The Investigation of Correlator Systems Utilizing Object and Frequency Space Filters

Hui Zhang

A thesis submitted in Partial fulfilment of the requirements for the degree of Doctor of Philosophy

Sponsoring Establishment: University of Abertay Dundee
Submitted: November 2000

I certify that this thesis is the true and accurate version of the thesis approved by the examiners.

Signed.. [redacted] **..(Director of Studies) Date.....** 4.Oct.2001

Declaration

I hereby declare that while registered as a candidate for the degree for which this thesis is presented I have not been a candidate for any other award. I further declare that, except where stated, the work in this thesis is original and was performed by myself.

Signed...  .....(Hui Zhang) Date...04/05/2001.....

Acknowledgements

I would like to thank my supervisors, Dr Colin Cartwright and Prof Allan Gillespie for their assistance and patience during my studies. Also thanks to Prof Zhaoqi Wang and Dr Nicholas Cook, for many discussions and suggestions while they were working and studying here, their advice is greatly appreciated.

The technical staff of the former division of Applied Physics and Material and of the EPICentre have been very helpful with all aspects. I also thank my fellow students for their encouragement and support throughout my time at the University of Abertay Dundee.

The Investigation of Correlator Systems Utilizing Object and Frequency Space Filters

Hui Zhang

Abstract

The aim of this research is to develop real-time object recognition systems which are robust and have good discrimination. An important aspect of this work is the development of a rotationally invariant optical correlator.

Optical correlation systems are investigated for the purpose of high speed, high discriminant and distortion invariant pattern recognition. A photorefractive joint transform correlator (JTC) using Bismuth Silicon Oxide (BSO) as a non-linear recording medium and a liquid crystal television as a spatial light modulator is implemented. The underlying physics is considered, some specific techniques to improve the operation are proposed.

The properties of photorefractive BSO are investigated for use as the dynamic holographic recording medium in information processing systems. The moving grating technique is used for edge-enhanced image reconstruction and for making the correlation peak sharper. The object and frequency space filtering methods are presented to improve the correlation performance, the discrimination, and to realise distortion invariant pattern recognition.

Circular harmonic matched filters and phase-only filters with different expansion orders are involved in the photorefractive JTC for real-time rotationally invariant pattern recognition. These filters can also be used to track an object with different orientations.

The coherent triple joint transform correlator employs a third beam to modify the Fourier spectrum and hence improves the correlation performance. In the incoherent triple JTC, the wavelet transform is used in the Fourier domain to achieve a high signal-to-noise ratio, noise robustness as well as discrimination. Several wavelet functions are also used, after processing, in the conventional JTC for high-speed image feature extraction. The wavelet transform functions can also be used in the JTC with circular harmonic filters to improve the output quality of rotation invariant pattern recognition.

List of Symbols

α	Absorption constant
e	Charge of an electron
$\mathbf{E}$	Total Electric field
E_0	Constant part of electric field
E_A	Applied electric field
E_D	Diffusion field
$\mathcal{E}$	Optical Electric Field
ε	Optical dielectric constant (= $\varepsilon_r\varepsilon_0$)
ε_0	Free space permittivity
ε_r	Relative dielectric constant
ε_s	Static dielectric constant
f	Focal length
ϕ_0	Phase shift of intensity interference pattern
Φ	Space charge grating phase shift
Γ	Two-wave coupling constant
λ	Optical wavelength
$\mathbf{H}$	Magnetic field
$\hbar$	Planck's constant divided by 2π
I_i	Intensity of *i*th beam
I_0	Total Intensity
$\mathbf{J}$	Current density
k_B	Boltzmann's constant
$\mathbf{k}_i$	Wave vector of *i*th beam
$\mathbf{K}$	Grating vector
κ	Coupling constant
L	Crystal thickness
Λ	Grating spacing

m	Intensity modulation
N_A^-	Acceptor density
N_D	Total donor density
N_D^+	Ionised donor density
n_e	Density of electrons
n_0	Unperturbed index of refraction
Δn	Change in refractive index
η	Intensity diffraction efficiency
P	Polarisation
r_{ij}	Electro-optic constant
r	Pump beam ratio
s	Photoionisation cross-section
θ	Incident angle of writing beams
σ	Diffracted Wave Vector
t	Time
T	Absolute temperature
μ	Free electron mobility
μ_0	Free space permeability
ω	Angular optical frequency

Contents

	Page
Chapter 1. Introduction	**1**
1.1 Pattern Recognition	1
1.2 The Photorefractive Effect	2
1.3 Main Aspects of the Research	3
1.4 The Outline of the Thesis	4
References	7
Chapter 2. Basic optical Transforms and Optical Correlator	**8**
2.1 Optical Linear Spatially Invariant Systems	8
2.2 The Fourier Transform and Fresnel Transform	10
2.3 The Basic Architectures of Optical Correlators	14
2.4 Performance Criteria	21
References	26
Chapter 3. Spatial Filtering Technique	**28**
3.1 A Summary of Optical Spatial Filters	28
3.2 Rotational Invariance and Circular Harmonic Filters (CHF)	36
3.3 CH Quantized Amplitude Compensated Matched Filters	39
3.4 Fresnel Lens-encoded Quantized Amplitude Compensated Filters	46
References	58
Chapter 4. Photorefractive BSO in Holography	**61**
4.1 Space-charge Field and the Refractive Index Grating	61
4.2 Energy Transfer Between Writing Beams in BSO	65
4.3 Diffraction from Volume Refractive Index Grating	69
4.4 Edge-enhancement with Moving Gratings inside the BSO Crystal	75
Reference	89

Chapter 5. Photorefractive Joint Transform Correlator (JTC) 93

5.1 The Liquid Crystal Television Used as Spatial Light Modulator 93

5.2 The Architecture of a Photorefractive JTC 97

5.3 Image Encoding 101

5.4 Pattern Recognition with the Photorefractive JTC 103

References 112

Chapter 6. Triple Joint Transform Correlator 115

6.1 The Optical Incoherent-erasure Technique 115

6.2 Coherent Triple Joint Transform Correlator 119

6.3 Incoherent Triple Joint Transform Correlator 131

References 134

Chapter 7. Wavelet Transform in the Photorefractive JTC 137

7.1 The Wavelet Transform 137

7.2 Image Feature Extraction with Wavelet Filters 140

7.3 Photorefractive JTC with Wavelet Filters 145

7.4 Image Feature Extraction in a Photorefractive JTC 154

Reference 161

Chapter 8. Rotationally Invariant Photorefractive JTC 163

8.1 The Photorefractive JTC with CHF 163

8.2 Experimental Comparison of CHF and Phase-only CHF in a JTC 163

8.3 Tracking a Rotating Object with the Photorefractive JTC 170

8.4 Wavelet Transforms in a Photorefractive JTC with CHF 174

References. 180

Summary and Conclusions 182

Appendix: List of Publications 187

Chapter 1. Introduction

1.1 Pattern Recognition

The aim of this research is to develop real-time object recognition systems that are robust and have good discrimination. An important aspect of this work is the development of a rotationally invariant optical correlator.

Pattern recognition is an important application of modern optics. The roots of optical pattern recognition can be traced back to Abbe's work in 1873, when he developed a method that led to the discovery of spatial filtering to improve the resolution of a microscope. However, optical pattern recognition did not actually find an application until the complex spatial filtering work of Vanderlugt in 1964 (VanderLugt, 1964). Since then, methods have been developed to construct efficient optical correlators for pattern recognition. Many systems exist in which objects and patterns are identified or classified with optical systems and computer algorithms. Basically there are two approaches in the optical implementation of pattern recognition, namely, the correlation approach and the neural network approach(Yu, 1998).

In the correlation approach, there are two frequently used architectures: the VanderLugt correlator (VLC) and the joint transform correlator (JTC). In 1966, two years after VanderLugt reported his optical structure, the first JTC architecture was demonstrated by Weaver and Goodman (Weaver, 1966). But the JTC had not assumed an important role in various applications until 1984 when a real time programmable JTC was reported by Yu and Lu (Yu, 1984). The basic distinction between the VLC and JTC are that the VLC depends on Fourier-domain filter synthesis, whereas the JTC depends on spatial-domain filtering. In the optical implementation, the Vanderlugt arrangement has an independent input scene, whereas the input scene is in the same plane with the filter in the JTC. Although the JTC has the same output function as the VLC, it avoids spatial filter synthesis problems and is less sensitive to optical system alignment.

Apart from correlators, artificial neural networks (Lippmann, 1987) are also used for pattern recognition. An important characteristic of neural networks is their massive interconnection and parallel processing. High resolution pattern recognition problems require a large number of neurons for parallel processing of an image, however, the number of parallel channels is limited because of the limited parallel interconnections with electronic wires. On the other hand, the parallel processing capability of optics permits these operations to take place at high speed, two dimensional optical processors are well suited for this problem. Ideally, an associative memory compares a given input pattern simultaneously with all possible matching patterns.

In the recent years, both approaches have been greatly improved. New philosophies and new algorithms have been developed for the design of better pattern recognition systems.

1.2 The Photorefractive Effect

The photorefractive effect was first encountered during frequency doubling experiments in the late 60's (Ashkin, 1966). It was discovered that an intense blue or green laser beam focused into $LiNbO_3$ or $LiTaO_3$ caused a change in the index of refraction of these crystals. This index inhomogeneity leads to distortions of the wavefront of transmitted beams, and to decollimation and scattering of light. The term "photorefractive effect" has now been adopted to describe the photoinduced refractive index changes.

Photorefractive effects have been observed in a variety of electro-optic materials, such as, in addition to the materials mentioned above, $BaTiO_3$, $Bi_4Ti_3O_{12}$ and $Bi_{12}SiO_{12}$. The possibility of using photorefractive materials as storage media was also reported. In the following years it was discovered that the refractive index change was reversible and applications in holography, information processing and other fields were proposed. In the field of optical information processing, real-time performance requires real-time

holographic recording devices, that is to say, the efficient and high-speed interaction between light beams containing information inside photorefractive materials is required. Therefore, the response time and the magnitude of the response, which depends on the electro-optic coefficient, of a photorefractive crystal are of great importance. Unfortunately, due to the nature of the effect, there must be a compromise between these two properties for most crystals. Some materials, such as Bismuth Silicon Oxide (BSO), are fast and reasonably sensitive with a relatively small electro-optic coefficient, while some others such as Barium Titanate ($BaTiO_3$) have a large electro-optic coefficient but respond rather slowly. Many applications of photorefractive crystals have been investigated, including coherent amplification, phase conjugation, media storage and real-time pattern recognition.

1.3 Main Aspects of the Project

This research has concentrated on the investigation of a real-time, photorefractive, optical, joint transform correlator for pattern recognition, in which the Fourier transform, Fresnel transform and wavelet transform are introduced and various filtering techniques are used for the purpose of improving the performance of the conventional JTC and to obtain the distortion-invariant pattern recognition. The following are the main aspects of this work:

- New spatial filter design and optimisation, circular harmonic quantized amplitude compensated matched filters, and Fresnel lens-encoded quantized amplitude-compensated matched filters with circular harmonic expansions, their performance merits and potential implementation with optics.

- The experimental investigation of the properties of the photorefractive crystal BSO, the energy transfer inside the crystal, the response time, the diffraction

efficiency for a transmission grating, and image edge enhancement by moving gratings in a BSO crystal at large fringe modulations.

- Triple joint transform correlator, one of the applications of the coherent erasure technique, to sharpen the correlation contour and improve the noise robustness and the discrimination of a matched-filter based photorefractive joint transform correlator, and investigation into incoherent triple joint transform correlators.

- Realisation of real-time rotationally invariant optical pattern recognition with the photorefractive joint transform correlator, the experimental comparison of the circular harmonic JTC and circular harmonic phase-only JTC for several single circular harmonic components, a multiple CHF used in a JTC to follow the track of an object with rotations within ±90.

- Wavelet transforms employed in the frequency domain of a photorefractive joint transform correlator to modify the conventional JTC and rotation-invariant JTC in correlation peaks, noise robustness and discrimination ability, also in the object domain for variant feature extraction.

1.4 Outline of the Thesis

There are seven chapters, in addition to Introduction and Conclusions, in this thesis. The contents of each chapter are listed below:

Chapter 2 introduces the fundamental background to this project. It includes the basic transforms and basic details of the two architectures of the optical correlator, the VanderLugt correlator and the joint transform correlator. The comparison of the different transforms and correlators is made. Some of the common measures of performance of the optical correlator are also introduced.

Chapter 3 covers the spatial filter design technique. The commonly used spatial filters, such as the matched filter, phase-only filter, inverse filter, and binary filter are described, and rotational invariance and circular harmonic filters are also introduced. The structure and performance of some novel filters, circular harmonic quantized amplitude compensated matched filters and Fresnel lens–encoded quantized amplitude compensated filters are presented.

Chapter 4 deals with the photorefractive effect and the crystal, BSO. Firstly we consider the basic properties of BSO: the photo-induced space charge field, the linear electro-optic effect, diffraction from a volume phase grating, energy transfer between write beams in steady state. Then we present the analysis and experimental results from an edge-enhanced reconstruction of moving gratings inside the photorefractive crystal BSO: the dependence of the optimum fringe velocity on the fringe modulation. We also show that the nonlinear dependence of the optimum fringe velocity on the fringe modulation provides a non-uniform enhancement of the diffraction efficiency with moving gratings. The edge-enhanced reconstruction of several images is also provided.

Chapter 5 introduces the structure of the photorefractive joint transform correlator. The properties and applications of the Epson liquid crystal television used as spatial light modulator are presented. The image coding technique is used to detour-phase encode images with non-positive values. The experimental results of pattern recognition with the photorefractive joint transform correlator are presented.

Chapter 6 deals with the triple joint transform correlator. The optical incoherent-erasure technique is introduced. The architectures and performance of the coherent triple joint transform correlator and incoherent triple joint transform correlator are presented and compared.

In chapter 7, the wavelet transforms are used in the photorefractive joint transform correlator. The basic properties of the wavelet transform, the mathematical formalism, the

basic types and the admission condition of the wavelet transform are introduced, and one of the most important uses of the wavelet transform in optics, image feature extraction is described. Then the wavelet transforms are employed in a photorefractive joint transform correlator to modify the correlation contours and to improve the discrimination ability and noise resistance. We also show that the joint transform of a scene with various wavelet functions can extract different features of images, such as corners and edges, effectively.

The last chapter, chapter 8, combines spatial filter design, the photorefractive joint transform correlator and the wavelet transforms together. Firstly, it introduces the photorefractive joint transform correlator with different order circular harmonic filters. The experimental comparison of performances of circular harmonic marched filters and phase-only circular harmonic filters in a joint transform correlator is presented. Then a multiple circular harmonic filter is used to track a rotating object in a photorefractive joint transform correlator. In the last part, the wavelet transforms are introduced into a circular harmonic joint transform correlator to improve the correlation outputs.

In the conclusion, a short statement is given to summarize the research. Further research is also discussed.

References: Introduction

A. Ashkin, G.D. Boyd, J.M. Dziedzic, R.G. Smith, A.A. Ballman, J.J. Levinstein, and K. Nassau, "Optically induced refractive index in-homogeneities in $LiNbO_3$ and LiTaO", App. Phys. Lett. **9**, No.1, 72-74 (1966).

R.P. Lippmann, " An introduction to computing with neural nets," IEEE Trans. Acoust. Speech Signal Process. **4**, 4-22 (1987).

D. Psaltis, D. Brady, and K. Wagner, " Adaptive optical networks using photorefractive crystals," Appl. Opt. **27**, 1752 (1988).

A. VanderLugt, "Signal detection by complex spatial filtering", IEEE Trans. on Inf. Theory, **IT-10**, 139-145 (1964).

C.S. Weaver and J. W. Goodman, "A technique for optically convolving two functions," Appl. Opt. **5,** 1248-1249 (1966).

F.T.S. Yu and X. J. Lu, "A real-time programmable joint transform correlator", Opt. Commun. **52**, 10-16 (1984).

F.T.S. Yu and D.A. Gregory, "Optical pattern recognition" (Ed: Yu and Jutamulia), Chapter 1, Cambridge University Press, Cambridge, 1998.

Chapter 2. Basic Optical Transforms and Correlators

2.1 The Linear Space Invariant Systems

Optical pattern recognition and classification is an attractive area in the field of optical information processing. The mathematical analysis used to study optical information processing is based on the theory of linear systems (Goodman, 1968; VanderLugt, 1992; Yu, 1983). In the first section of this chapter, the properties of the linear space invariant system are introduced.

An optical system can be described by the input excitation, system operation, and output response. That is the system operating on the input excitation to produce the output response. If the input excitations are $f_i(x_1, y_1)$, and $g_i(x_2, y_2)$ represent the corresponding output, where (x_1, y_1) and (x_2, y_2) are the coordinate systems of the input and output planes respectively, then by the definition of $L\{\ \}$, their relationship can be expressed as:

$$L\{f_i(x_1, y_1)\} = g_i(x_2, y_2) \tag{2.1}$$

A specific system is said to be linear if it satisfies the principle of superposition for all input functions $f_i(x, y)$ and all complex constants C_i:

$$L\left\{\sum_i C_i f_i(x_i, y_i)\right\} = \sum_i C_i L\{f_i(x_1, y_1)\} = \sum_i C_i g_i(x_2, y_2) \tag{2.2}$$

This ability indicates that the response of the system can be obtained by decomposing this input into a linear combination of elementary functions, finding the response to each elementary function and then taking the same linear combination of these elementary

responses. The decomposition can be achieved by the shifting property of the impulse δ function such that any input can be expressed as:

$$f(x_1, y_1) = \int_{-\infty}^{\infty} \int f(x_0, y_0)\delta(x_1 - x_0, y_1 - y_0)dx_0 dy_0 \tag{2.3}$$

where (x_0, y_0) is the position of the δ function in the input plane, in this way $f(x_1, y_1)$ is written as a linear combination of weighted and shifted δ functions. The output response of the linear optical system may now be expressed as (Goodman, 1968):

$$\begin{aligned} g(x_2, y_2) &= L\{f(x_1, y_1)\} \\ &= \int_{-\infty}^{\infty} \int f(x_0, y_0) L\{\delta(x_1 - x_0, y_1 - y_0)\} dx_0 dy_0 \end{aligned} \tag{2.4}$$

where $f(x_0, y_0)$ is simply a weighting factor and the linearity property allows the operator $L\{\ \}$ to act on the individual impulse functions. $L\{\delta(x_1 - x_0, y_1 - y_0)\} = h(x_2, y_2; x_0, y_0)$ is the impulse response of the system. The linear system is space-invariant if the impulse response function can be simplified as:

$$h(x_2, y_2; x_0, y_0) = h(x_2 - x_0, y_2 - y_0) \tag{2.5}$$

So the space-invariant system means the displacement of the impulse in the input plane only causes a corresponding displacement of the response in the output plane without change of functional form and the Eq. (2.4) can then be written as:

$$g(x_2 y_2) = \int_{-\infty}^{\infty} \int f(x_0, y_0) h(x_2 - x_0, y_2 - y_0) dx_0 dy_0 \tag{2.6}$$

which is the two dimensional convolution of the object function with the impulse response of the system. Thus the output response for an input function can be obtained by first calculating the response of the impulse at the point (x_0, y_0) of the input plane, and then convoluting it with the input excitation. Eq.(2.6) can be simplified as:

$$g = f * h \tag{2.7}$$

where * denotes the convolution operation. The physical variables in Eq. (2.7) may be either complex amplitude or intensity for an optical system. Many optical systems can be considered as a linear system and therefore can be assigned an impulse response function. The linear and space-invariant systems can be evidently simplified by taking the convolution operation after Fourier transform.

2.2 The Fourier Transform and Fresnel Transform

2.2.1 The Fourier transform

The Fourier transform (Goodman, 1968) is widely used in signal analysis. It generates a function that displays the frequency content of a signal and is useful since some features are more easily analysed or detected in the frequency domain than in the object domain. The Fourier transform is also the basis of modern optics. The two dimensional Fourier transform is particularly important for optical information processing. It is the basis of spectrum analysis, spatial filtering, and the convolution and correlation operations of optical signals.

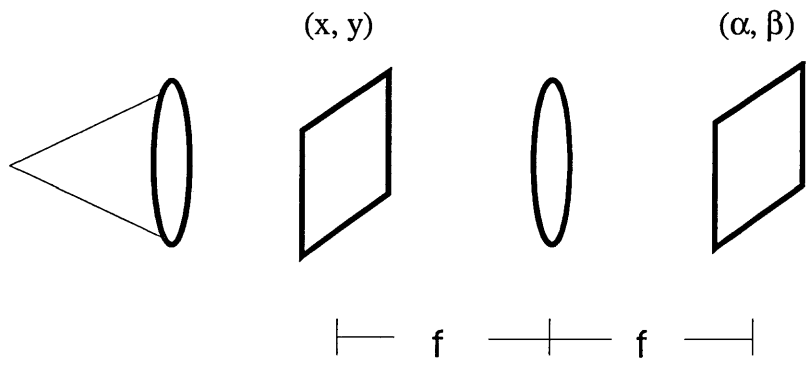

Fig. 2.1 The Fourier transform system

Suppose an object $f(x,y)$ is inserted in the front focal plane of a lens and illuminated by coherent light. The complex amplitude at the back focal plane of the lens is given by the Fourier transform (Javidi, 1994):

$$F(p,q) = F[f(x,y)]$$

$$= \int_{-\infty}^{\infty}\int f(x,y)\exp[-i(px+qy)]\mathrm{d}x\mathrm{d}y \tag{2.8}$$

with

$$\mathrm{p} = \frac{2\pi\alpha}{\lambda \mathrm{f}} \qquad \mathrm{q} = \frac{2\pi\beta}{\lambda \mathrm{f}} \tag{2.9}$$

where F(p, q) is the Fourier spectrum, F denotes the Fourier transform, (α, β) is the coordinate system in the back focal plane of the lens, λ is the illuminating wavelength, f is the focal length of the transform lens, and (p, q) are the spatial frequency coordinates. After the first transform, the original object can be obtained from its Fourier spectrum by an inverse Fourier transform. This can be done by another transform lens with an inverse coordinate system in the back focal plane of the lens. The corresponding inverse Fourier transform is:

$$f(x,y) = F^{-1}[F(p,q)]$$
$$= \iint F(p,q)\exp[i(px+qy)]dpdq \tag{2.10}$$

where F^{-1} denotes the inverse Fourier transform. One important property of the Fourier transform is its translation invariance. Suppose the input object shifts to a position (x_0, y_0),

$$F[f(x-x_0, y-y_0)] = \int_{-\infty}^{\infty}\int f(x-x_0, y-y_0)\exp[-i(px+qy)]dxdy$$
$$= \exp[-i(px_0+qy_0)]F(p,q) \tag{2.11}$$

i.e. the translation of the object only causes a linear phase shift in the Fourier spectrum with any change of position.

One important property of the Fourier transform is the correlation theorem. Consider two Fourier transform pairs:

$$f_1(x,y) \leftrightarrow F_1(p,q), \text{ and } f_2(x,y) \leftrightarrow F_2(p,q) \tag{2.12}$$

The inverse Fourier transform of the function $F_1(p, q)F_2^*(p, q)$, where the superscript * denotes the complex conjugation is, the cross correlation of the original objects (Yu, 1983):

$$\iint F_1(p,q)F_2^*(p,q)\exp[i(px+qy)]dpdq = \iint f_1(x', y')\, f_2(x'-x, y'-y)\, dx'dy'$$
$$= f_1(x,y) \otimes f_2(x,y) \tag{2.13}$$

where $\otimes$ denotes the correlation operation. The correlation operation yields a sharply peaked intensity distribution, and therefore it can be used for signal detection and pattern recognition.

2.2.2 The Fresnel transform

The Fourier transform possesses the property of translation invariance. It is a useful property under some circumstances. However, there are applications of optical pattern recognition in which the translation invariance of the object could be a drawback. For instance, when the placement of the object is as important as its identity. Space-variant pattern recognition can be realized by using Fresnel transforms in the optical correlator. Consider the optical system in which the output plane is not at the focal plane but a distance away from the transform lens, as shown in Fig. 2.2, but assume the input plane is at the front focal plane of the transform lens. The complex light distribution at the output plane is given by the Fresnel transform (Davis, 1992):

$$
\begin{aligned}
Fr(p,q) &= Fr[f(x,y)] \\
&= \int_{-\infty}^{\infty}\int_{-\infty}^{\infty} f(x,y)\exp\left\{\frac{i\pi}{\lambda f}\left[(\xi - x)^2 + (\eta - y)^2\right]\right\}\exp\left[\frac{-i\pi}{\lambda f}(\xi^2 + \eta^2)\right] \\
&\quad \exp\left\{\frac{i\pi}{\lambda d}\left[(\alpha - \xi)^2 + (\beta - \eta)^2\right]\right\} dx\,dy\,d\xi\,d\eta \qquad (2.14) \\
&= F\left[f(x,y)Z(x,y;d,f)\right]
\end{aligned}
$$

Where Fr indicates the Fresnel transform, Fr(p, q) is the Fresnel spectrum, (α, β) is the coordinate system of the selected Fresnel transform plane, (ξ, η) is the coordinate system in the lens plane, and Z(x, y; d, f) is a phase function:

$$
Z(x,y;d,f) = \exp\left[\frac{i\pi}{\lambda f}\left(1 - \frac{d}{f}\right)\left(x^2 + y^2\right)\right] \qquad (2.15)
$$

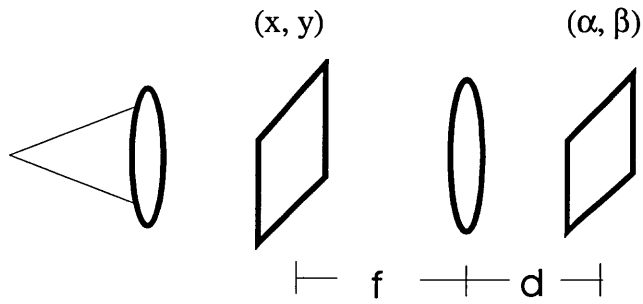

Fig. 2.2 The Fresnel transform system

It shows that the Fresnel transform of a signal can be regarded as the Fourier transform of the signal modified by a quadratic phase factor. A Fresnel transform filter could perform as well as a Fourier transform filter, although the Fresnel transform possesses no shift invariance. Using this shift variance property of the Fresnel transform, a space variant optical correlator can be set up, which can detect not only the shape, but also the correct placement of an object.

2.3 The basic architectures of optical correlation

The basic optical correlation operation may be demonstrated using the setup shown in Fig. 2.3 where two lenses are used to form the so called 4-f system. The first lens may be considered as generating the Fourier transform of the object in the Fourier plane, the second one then performs the inverse transform. A Fourier transform filter $F_2^*(p,q)$ is inserted at the back focal plane of the first transform lens. If a scene $f_1(x,y)$ is displayed at the front focal plane of the first transform lens, the cross correlation of $f_1(x,y)$ with $f_2(x,y)$ will be formed at the back focal plane of the second transform lens. The

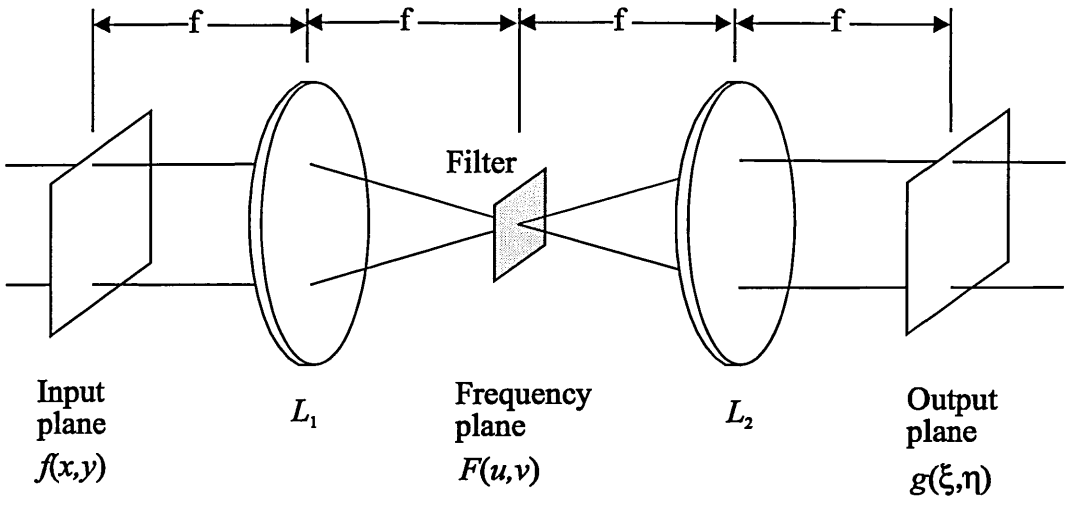

Fig. 2.3 The 4f optical system for optical correlation.

correlator possesses shift invariance because the Fourier transform is used in the optical system. The filter inserted at the Fourier plane to modify the spatial frequencies of the distribution is known as a spatial filter.

The output of the system can be denoted as:

$$g(\xi,\eta)=\int_{-\infty}^{\infty}\int f_1(x,y)f_2(x-\xi,y-\eta)dxdy \tag{2.16}$$

it is a correlation operation.

Based upon the 4-f system there are several practical correlation implementations. The most common are the matched-filter-based VanderLugt correlator (VLC) and the joint transform correlator (JTC).

2.3.1 The Vanderlugt matched-filter-based correlator

The matched filter is the optimum linear filter for maximising the ratio of peak signal to mean-square noise when we process a deterministic signal in the presence of additive, stationary random noise. Suppose the information we process is

$$f(x,y) = s(x,y) + n(x,y) \tag{2.17}$$

$f(x,y)$ is the sum of the signal $s(x,y)$ and stationary random noise $n(x,y)$.

Suppose $h(x,y)$ is the impulse response of a linear, space-invariant filter $H(p,q)$, the response of which we seek to optimise. As the signal is deterministic and as signal and noise are additive, the signal part of the output is

$$g_s(x,y) = \iint S(p,q)H(p,q)e^{i2\pi(px+qy)}dpdq \tag{2.18}$$

where $S(p,q)$ is the Fourier spectrum of the signal and we design a filter which maximizes $|g(0,0)|^2$. The noise power in the output plane can be expressed as (VanderLugt, 1992)

$$r_n(0,0) = \iint R_n(p,q)|H(p,q)|^2 dpdq \tag{2.19}$$

where $R_n(p,q)$ is the noise spectrum. The ratio of peak signal-to-noise can be deduced from Eqs. (2.18) and (2.19):

$$SNR = \frac{\left|\iint\left[\frac{S(p,q)}{R_n(p,q)}\right]H(p,q)R_n(p,q)dpdq\right|}{\iint R_n(p,q)|H(p,q)|^2 dpdq} \tag{2.20}$$

We apply the generalized Schwartz inequality to the numerator, with $R_n(p,q)$ as the non-negative function, under the condition

$$H(p,q) = \frac{S^*(p,q)}{R_n(p,q)} \tag{2.21}$$

and we have

$$SNR \leq \iint \frac{|S(p,q)|^2}{R_n(p,q)} dpdq \tag{2.22}$$

Therefore, the magnitude of the optimum filter is proportional to the magnitude of the Fourier transform of the signal and inversely proportional to the noise spectral density. Because the phase of the optimum filter is conjugate, or matched, to the phase of the Fourier transform of the signal , $H(p,q)$ is called a matched filter. As a special case, if the noise spectral density is uniform for all spatial frequencies, the filter becomes

$$H(p,q) = S^*(p,q) \tag{2.23}$$

This is the easiest form of the matched filter. The field transmitted by such a matched filter is entirely real and all phase variation is eliminated across the Fourier domain. Consequently the final lens focuses an amplitude-weighted plane wave to a bright spot denoting recognition. If the filter is not matched there will be no spot, the matched filter system will therefore recognize the input signal. If the input is not centred at the origin, the bright correlation spot in the output plane simply shifts by a proportional distance.

The output of the system for the special case of Eq. (2.23) is:

$$g(x', y') = \iint F(p,q) S^*(p,q) \exp[-i(px'+qy')] dpdq \tag{2.24}$$

By using the convolution theorem, this can be expressed as:

$$g(x', y') = \iint f(x, y)s^*(x - x', y - y')dxdy \tag{2.25}$$

which is a correlation operation.

However, the matched filter is difficult to use in practice, it contains amplitude and phase information which can be difficult to calculate and control, and if the images have a high space bandwidth product, the positional alignment may cause problems.

The problem of calculation and control of phase information were solved by the VandeLugt filter. VanderLugt holographically fabricated the matched spatial filter in 1964 (VanderLugt, 1964). In this technique, a hologram was recorded by exposing a film to the interference produced by a plane wave and the Fourier transform of the object. After development, the hologram is replayed by the Fourier transform of the reference image to generate, via a probe beam, the correlation of the object and reference images. It is necessary to record the Fourier hologram optically, the filter can be produced as a synthetic or computer-generated hologram, giving much greater speed and flexibility. Coherent correlators can deal with a complex signal, where the processing of the amplitude and phase information is significant in many cases.

The problem with positional sensitivity was removed with the development of the joint transform correlator (JTC) (Weaver, 1966). This system records the joint power spectrum of the Fourier transforms of the object and reference images. After development the hologram is replayed by a plane wave so the position of the filter is not critical, the cross-correlation of the two images is present in the output.

2.3.2 Joint transform correlator

The basic arrangement of the joint transform correlator is shown in Fig. 2.4. The reference and input scene functions are displayed on the spatial light modulator (SLM) in positions $(-x_0,0)$ and $(x_0,0)$ respectively. The joint power spectrum (JPS) of these two

functions is linearly recorded by the CCD camera; the joint power spectrum is the intensity of the interference formed by the Fourier transforms of the two functions. In general, the Fourier plane recording device requires a large dynamic range to record the JPS linearly. The captured JPS is then displayed on the SLM again and a further Fourier transform yields correlations at the output plane, amongst which is the cross-correlation of the reference and input scene functions. The output can be captured using the CCD camera again, and the correlations displayed on a monitor or captured by a framegrabber card for further analysis.

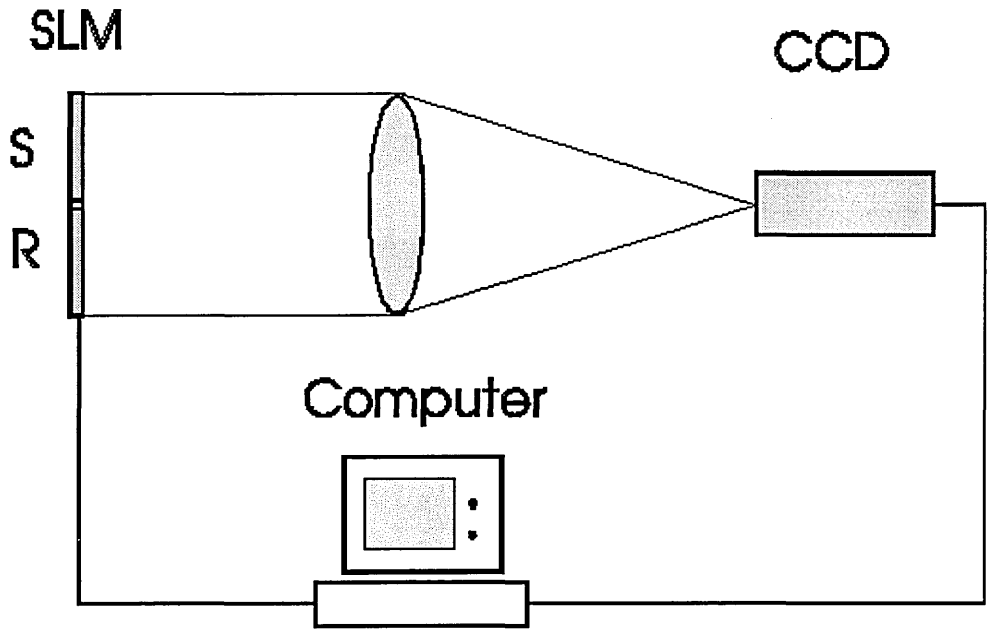

Fig. 2.4 The architecture of joint transform correlator (single modulator)

As a reference object $r(x-x_0, y)$ and an unknown object $s(x+x_0, y)$ are written side by side onto the input plane, the input object of the JTC is denoted by

$$h(x,y) = r(x-x_0, y) + s(x+x_0, y) \tag{2.26}$$

The joint transform power spectrum $|H(p,q)|^2$ in the Fourier plane is giving by (Javidi, 1994)

$$\begin{aligned}|H(p,q)|^2 &= |R(p,q)+S(p,q)|^2 \\ &= R(p,q)R^*(p,q)+S(p,q)S^*(p,q)+R^*(p,q)S(p,q)\exp(j2x_0p) \\ &+ R(p,q)S^*(p,q)\exp(-j2x_0p)\end{aligned} \tag{2.27}$$

where R(p, q) and S(p, q) denote the Fourier transforms of r(x, y) and s(x, y) respectively and the superscript * denotes the complex conjugate. In the conventional case, the Fourier transform of Eq. (2.27) can produce the following correlation signals at the output plane (Javidi, 1994):

$$C(x',y') = R_{11}(x',y') + R_{22}(x',y') + R_{12}(x'-2x_0,y') + R_{21}(x'+2x_0,y') \tag{2.28}$$

where

$$\begin{aligned}R_{21}(x',y') &= R_{12}(-x',-y') = \iint s(\xi,\zeta)r(\xi-x',\zeta-y')d\xi d\zeta, \\ R_{11}(x',y') &= \iint s(\xi,\zeta)s(\xi-x',\zeta-y')d\xi d\zeta, \\ R_{22}(x',y') &= \iint r(\xi,\zeta)r(\xi-x',\zeta-y')d\xi d\zeta.\end{aligned} \tag{2.29}$$

In Eq. (2.28), the first two terms are the autocorrelation terms. The terms of interest are the third and fourth, which are the cross correlation terms of the reference image and the target. A sufficiently large distance between the reference and target at the input plane makes the correlation terms at the output plane separate from each other. Basically, there is no difference between the output functions of the Vanderlugt correlator and the conventional joint transform correlator, however, the joint transform correlator is much easier for optical implementation.

Since the cross-correlations of the reference with the scene signal yield the same output as a matched filter (as shown in Eq(2.27)), the JTC also suffers from low discrimination. Some nonlinear techniques can be use to improve the performance of a JTC. These techniques transform the joint power spectrum in the Fourier plane nonlinearly. The use of nonlinear methods has been shown to be effective with good performance, such as sharper correlation peaks and higher discrimination. Among them, the phase-only JTC and the binary JTC give out quite good correlation output.

2.4 Performance Criteria

This section introduces the various criteria which have been developed to assess the performance of different correlation systems. The main performance measures introduced here are signal-to-noise ratio, light efficiency, peak sharpness, peak location, discriminability, and distortion invariance (Kumar, 1990). The methods of estimating these properties are listed below.

Signal-to-noise ratio

When random noise is added to the input scene, the output will fluctuate from experiment to experiment. It is desirable to keep this fluctuation to a minimum, and the output as large as possible for each noise level. This achieved by maximizing the following conventional correlation peak SNR measure which is defined as the ratio of the expected value squared of the correlation peak amplitude to the variance of the correlation peak amplitude (Kumar, 1990):

$$SNR = \frac{|E[g(0,0)]|^2}{\mathrm{var}\{g(0,0)\}} \tag{2.30}$$

where $E[g(0,0)]$ is the ensemble average or expected peak value and $\mathrm{var}\{g(0,0)\}$ denotes the variance. This SNR measure considers only the average and the variance of

the peak and not of any other point in the output. It is not suited for defining output peak sharpness. The numerator in Eq. (2.30) represents the square of the average of the values at the origin obtained when many different sample realisations from the noise process corrupt the input scene. Similarly, the denominator represents the variance of these values. Thus the SNR measure can not be estimated using just one correlation experiment. Higher SNR values indicate better noise tolerance and lower average probability of error in detection. The best way to incorporate the effects of random noise into any investigation is by using appropriate statistical descriptions.

Note that the above SNR measure is not the same as that used to design the matched filter, which was given in Eq. (2.20)

$$SNR = \frac{|g(0,0)|^2}{r_n(0,0)} = \frac{\left|\iint S(p,q)H(p,q)dpdq\right|^2}{\iint R_n(p,q)|H(p,q)|^2 dpdq} \tag{2.31}$$

It is described as the peak signal intensity divided by the noise power.

Light Efficiency

In optical correlators it is important that the output intensity at the correlation plane is maximized, so that detectors in this plane can respond quickly and accurately. The light efficiency was originally quantified using the following measure, called the Horner Efficiency (Caulfield, 1982):

$$\eta_H = \frac{\iint |f_1(x,y) * f_2(x,y)|^2 dxdy}{\iint |f_1(x,y)|^2 dxdy} = \frac{\text{Total energy in the correlation plane}}{\text{Total energy in the input plane}} \tag{2.32}$$

It is easy to see from this measure that η is always less than or equal to 1. Another easy form of the Horner efficiency is to use the peak correlation intensity in the correlation plane, instead of total energy in the correlation plane, in Eq. (2.32), it expressed as

$$\eta_H' = \frac{|g(0,0)|^2}{\iint |f_1(x,y)|^2 dxdy} = \frac{\text{Peak correlation intensity}}{\text{Total energy in the input plane}} \tag{2.33}$$

Peak Sharpness

Another attribute we would like to have in correlators is the ability to locate the inputs accurately. The accuracy of the detection of the target will be increased for sharp correlation peaks. Several measures have been proposed. The first one is the peak-to-sidelobe ratio (PSR), given by (Kumar, 1990):

$$PSR = \frac{|E[g(0,0)]|^2}{\text{var}[g(x', y')]} \tag{2.34}$$

where (x', y') represents an arbitrary point in the output plane far from the origin. The numerator in Eq. (2.34) is the squared magnitude of the average output peak, whereas the denominator is the output variance at the point away from the peak. Usually the PSR will be larger for sharper peaks. It is also shown that the SNR measure in Eq. (2.31) and this PSR are closely related.

Another measure of peak sharpness is the peak-to-root mean square ratio (PRMSR) (also called the signal-to-noise ratio):

$$PRMSR = \frac{|g(0,0)|^2}{g_{rms}^2} \tag{2.35}$$

where the peak is assumed to occur at the origin. Let Ω denote the set of output pixels for which the output values are below 50% of the peak value and let N_Ω denoted the number of pixels in this set. Then g_{rms} is defined according to:

$$g_{rms} = \left[\frac{1}{N_\Omega} \sum_{i \in \Omega} |g(x,y)|^2 \right]^{1/2} \tag{2.35}$$

The SNR in the following chapters mostly use this definition. The sharpness of the correlation peak can also be measured using the following peak-to-correlation energy (PCE) measure:

$$PCE = \frac{|g(0,0)|^2}{\iint |g(x,y)|^2 \, dxdy} \tag{2.36}$$

where the denominator is the total correlation energy. For sharp correlation peaks, most of the energy in the correlation plane will be in the peak, and the PCE will be large, for broad correlation peaks, PCE will approach 0. Also, PCE is a smooth measure because of the averaging involved in defining denominator. In addition, it is analytically tractable (Kumar, 1990).

Discriminability

Discriminability refers to the ability to detect one class of deterministic signal whilst rejecting others; it is different from the SNR measurement which refers to detection of a deterministic signal in random noise. It is relatively easy to discriminate against known false inputs, this is achieved using the following matched filter

$$H(p,q) = S_1^*(p,q) - S_2^*(p,q) \tag{2.37}$$

where $s_1(x,y)$ and $s_2(x,y)$ are the desired and false inputs respectively; $S_1^*(p.q)$ and $S_2^*(p,q)$ are the conjugates of their Fourier transforms.

A good measure of discrimination between two inputs in random noise is given by the Fisher ratio (Kumar, 1990)

$$\mathrm{FR} = \frac{\left|E\{g_1(0,0)\} - E\{g_2(0,0)\}\right|^2}{\frac{1}{2}\left[\mathrm{var}\{g_1(0,0)\} + \mathrm{var}\{g_2(0,0)\}\right]} \tag{2.38}$$

Higher FR values imply better discrimination between the two signal inputs. The denominator accounts for the fact that good discrimination also depends on low variance in the correlation peak heights.

Distortion invariance

Another desired feature in correlation filters is that the resulting output peak remain relatively insensitive to distortions in the input image, such as translations, scale changes, rotations, and view-angle differences. In a two-class discrimination problem, let Ω_1 denote the set of all possible images from class 1 (distorted set) and Ω_2 denote the set of all possible images from class 2 (normal set). Then a good measure of the distortion invariance is the discrimination ratio (DR) defined below (Kumar, 1990):

$$DR = \frac{\min_{i\in\Omega_1}\left|g_i(0,0)\right|}{\max_{i\in\Omega_2}\left|g_i(0,0)\right|} \tag{2.39}$$

where $g_i(0,0)$ is the output at the origin when the input is the ith signal from the set. Ideally, DR is close to one. Different types of distortion invariant filters can be designed using mathematical techniques.

Chapter 2: References

N.J. Cook, "Properties and processing applications of photorefractive BSO", PhD thesis, University of Abertay Dundee (Supervisor: Colin M. Cartwright), 1998.

J.A. Davis, D.M. Cottrell, N. Nestorovic, and S. M. Highnote, "Space-variant Fresnel transform optical correlator", Appl. Opt. **31**, 6889-6893 (1992).

J.W. Goodman, "Introduction to Fourier Optics," Chapter 1, McGraw-Hill, New York (1968).

J. L. Horner, P.D. Gianino, "Phase-only matched filter,", Appl. Opt. 23(6), 812-816 (1984).

B. Javidi, and J.L. Horner, "Real-time optical information processing", Chapter 2, 4, Academic Press, Inc, California, 1994.

B. V. K. Kumar, and L. Hassebrook, "Performance measures for correlation filters", Appl. Opt. **29**(20), 2997-3006 (1990).

B.V. K. Kumar, "Tutorial survey of composite filter designs for optical correlatiors", Appl. Opt. **31**(23), 4773-4801 (1992).

A.VanderLugt, "Optical Signal Processing", Chapters 3, 5, Wiley-Interscience, New York (1992).

A. VanderLugt, "Optimum sampling of Fresnel transforms", Appl. Opt. **29**, 3352-3361 (1990).

A. VanderLugt, "Signal detection by complex spatial filtering", IEEE Trans. on Inf. Theory, **IT-10**, 139-145 (1964).

Z.Q. Wang, "Real-time optical intensity correlation using photorefractive BSO", PhD thesis, University of Abertay Dundee (Supervisor: Colin M. Cartwright), 1995.

C.S. Weaver and J. W. Goodman, "A technique for optically convolving two functions," Appl. Opt. **5,** 1248-1249 (1966).

F.T.S. Yu, "Optical information processing," Chapter 1, Wiley-Interscience, New York (1983).

Chapter 3. Spatial Filtering Technique

3.1 A Summary of Optical Filters

The holographically fabricated matched spatial filter (MSF) as developed by VanderLugt has been widely applied to object detection in a noisy background and optical pattern recognition. It has been shown, using the Schwarz inequality, that the matched filter is the optimum filter for signal extraction from white noise, while for optical pattern recognition it is effective because the normalised peak intensity of an autocorrelation is always higher than that of a cross-correlation. In an investigation of the properties of the optical correlator, Horner found that the optical power efficiency (Horner efficiency, Horner, 1982) of the matched spatial filter is low due to the absorptive nature of the filter, and because of this he proposed a modified phase-only matched filter (POF). By computer simulation it has been shown that the phase-only matched filter (Horner, 1984) has a high Horner Efficiency and a significantly improved discrimination. Horner's work in fact implied that it is the Fourier amplitude spectrum content in the matched spatial filter that reduces the discrimination ability of the correlator. As further developments of this idea, the binary phase-only filter (BPOF) (Farn, 1988), in which only two values, namely –1 and +1, exist, the ternary matched filter (Flannery, 1988), the amplitude-compensated matched filter (ACMF) (Mu, 1988), the amplitude-modulated phase-only filter (AMPOF) (Awwal, 1990), and other synthetic filters have been proposed. In this section these developments are reviewed.

The matched filter

As introduced in chapter 2, suppose that $h(x, y)$ is the impulse response of a linear, space-invariant filter $H(u, v)$, the response of which must be optimised. It is found that the highest SNR is achieved when:

$$H(u,v) = \frac{S^*(u,v)}{R_n(u,v)} \tag{3.1}$$

The magnitude of the optimum filter is therefore proportional to the magnitude of the Fourier transform of the signal and inversely proportional to the noise spectral density. Because the phase of the optimum filter is conjugate, or matched, to the phase of the Fourier transform of the signal, $H(u,v)$ is called a matched filter. For the special case where the additive noise is white, i.e. the spectral density is uniform for all spatial frequencies, the optimum filter becomes:

$$H(u,v) = S^*(u,v) \tag{3.2}$$

which is also referred to as a matched filter. The wavefront transmitted by such a matched filter is entirely real (proportional to SS^*) and all phase variation is eliminated across the Fourier domain.

Supposed that $f(x,y)$ is the input scene, the output of Eq. (3.2) in a correlation system is

$$g(\xi,\eta) = \int_{-\infty}^{\infty}\int F(u,v)S^*(u,v)\exp\left[-j(ux+vy)\right]dudv \tag{3.3}$$

The matched filter is difficult to use in practice; it contains amplitude and phase information which can be difficult to calculate and control. If the images have a high space-bandwidth product, the positional alignment may cause problems.

Phase-only Filters

While the MSFs discussed in the last subsection are optimal from an SNR point of view, they suffer from two practical drawbacks. The first is their severe sensitivity to distortions in the input. Another problem is that the Horner efficiency of an MSF is usually very low. To alleviate the low light efficiency problem of the MSFs, Horner and Gianino suggested the following phase-only filter (Horner, 1984):

$$H_{POF}(u,v) = \frac{S^*(u,v)}{|S(u,v)|} \tag{3.4}$$

or

$$H_{POF}(u,v) = \exp[-i\phi(u,v)] \tag{3.5}$$

It is obvious from Eq (3.5) that $|H_{POF}(u,v)| = 1$ so that no light is absorbed by the medium in the filter plane. The POF has been shown to yield sharper correlation peaks but exhibit even more sensitivity to input distortion and its 'all-pass' nature makes it extremely sensitive to noise in the input.

Binary Phase-Only Filters

The POFs discussed in the last subsection constrain the magnitude to 1, but can take any phase values. In contrast, binary phase-only filters (BPOFs) take only two values,

namely, -1 and +1. They are named binary phase-only filters because –1 can be thought of as $\exp(j\pi)$ and +1 as $\exp(j0)$. The BPOFs are easily constructed by magneto-optic and ferro-electric spatial light modulators (SLM) capable of accommodating these two values.

The MSF is complex valued, and the BPOF has only two values. To code the complex filter $H(u,v) = S^*(u,v)$ onto a binary device, several methods have been used (Javidi, 1994). These include binarizing the real part, the imaginary part, or some combination of the two:

$$\begin{aligned} H_1(u,v) &= \mathrm{sgn}[S_R(u,v)] \\ H_2(u,v) &= \mathrm{sgn}[S_I(u,v)] \\ H_3(u,v) &= \mathrm{sgn}[S_R(u,v) + S_I(u,v)] \end{aligned} \tag{3.6}$$

where

$$\mathrm{sgn}[x] = \begin{cases} +1 & \text{if } x \geq T \\ -1 & \text{if } x < T \end{cases} \tag{3.7}$$

and

$$S(u,v) = S_R(u,v) + jS_I(u,v) \tag{3.8}$$

The amplitude binary means that $H(u,v)$ takes on only two values (+1 and –1), T is the threshold value.

The Inverse Filter and the Amplitude-Compensated Matched Filter

Another type of spatial filter that will give a delta function detection peak in the correlation plane is the inverse filter (IF), which is defined as

$$\begin{aligned} H_{IF}(u,v) &= \left|H_R(u,v)\right|^{-1} \exp[-i\phi_R(u,v)] \\ &= H_R{}^{*}(u,v)\left|H_R(u,v)\right|^{-2} \end{aligned} \tag{3.9}$$

However, the IF has severe limitations associated with mathematical poles and small optical efficiency. In order to avoid the poles, at the points where the modulus is tending to zero, a constant value is inserted, i.e.,

$$\begin{aligned} H_{IF}(u,v) &= \left|H_R(u,v)\right|^{-1} \exp[-i\phi(u,v)] && \text{if } \left|\mathrm{H_R}(u,v)\right| > \varepsilon_{\mathrm{T}} \\ H_{IF}(u,v) &= \varepsilon_{\mathrm{T}}{}^{-1} \exp[-i\phi(x,y)] && \text{if } \left|\mathrm{H_R}(u,v)\right| < \varepsilon_{\mathrm{T}} \end{aligned} \tag{3.10}$$

where ε_{T} is an arbitrary threshold to be determined.

The amplitude-compensated matched filter $H_{ACMF}(p,q)$ is a type of approximate inverse filter, which consists of two different filtering functions. It takes the form of a phase-only filter where the modulus of the Fourier amplitude spectrum is lower than a threshold value, and takes the form of an inverse filter where the modulus of the Fourier amplitude spectrum is higher than the threshold value:

$$H_{ACMF}(p,q)=\begin{cases} H_{POF}(p,q) & \text{When } |H(p,q)| < F_0 \\ \dfrac{F_0}{|H(p,q)|}H(p,q) & \text{When } |H(p,q)| \geq F_0 \end{cases} \tag{3.11}$$

where F_0 is the threshold value. If an object $f(x,y)$ is fed into the optical correlator, the filtered wave-front will be not only uniform in phase but also show reduced variations in amplitude, which makes the correlation peak much sharper. This type of filter is inherently energy absorptive, and the total signal energy transferred to the output plane is much lower than that with any other type of filter. Therefore the noise tolerance is poor. However, the light efficiency does not suffer seriously because the absorption mainly takes place at the region of low spatial frequency which has less energy contribution to the correlation peak (Wang, 1992).

The synthetic discriminant function (SDF) filters

The SDF concept was originally introduced by Hester and Casasent in the context of coherent correlation (Hester, 1980). For a class of objects, the coherent SDF is formed from a weighted linear combination of the complex amplitude distributions of these objects.

As discussed before, matched filters suffer from their sensitivity to input distortions, such as scale changes and rotations. A filter may need to be designed to yield similar output values with distorted as well as undistorted images, and SDFs present one

approach to such distortion-invariant filter design. The basic SDF method uses a set of N images, which are obtained by deliberately distorting the reference image and it is supposed that these N images, $s_1(x,y)$, $s_2(x,y),\ldots,$ $s_N(x,y)$ are representative of all the expected distortions. The SDF is a composite function r(x,y):

$$r(x,y)=\sum_{i=1}^{N} a_i s_i(x,y) \tag{3.12}$$

where a_i, i = 1, 2, ..., N, are the appropriate coefficients, which are chosen so that when x(x,y) is cross-correlated with $s_i(x,y)$, we get a desired constant c_i as the value of the output at the origin, i.e.,

$$\int_{-\infty}^{\infty}\int_{-\infty}^{\infty} r(x,y)s_i(x,y)dxdy = c_i, \qquad \text{for i} = 1,2,\ldots,\text{N}. \tag{3.13}$$

If the set contains images from two separate classes, then we can set c_i to 1 for images from the desired class and to 0 for images from the other class. The purpose of this "training" is that when this filter correlates with a nontraining image, the output at the origin will be close to 1 for true class images and close to zero for false class. To calculate this function, we seek a set of functions which are linear combinations of the distributions of the object:

$$\sum_{i=1}^{N} a_i H_{ij} = C_j \qquad \text{for j} = 1,2,\ldots,\text{N}, \tag{3.14}$$

where

$$H_{ij} = \int_{-\infty}^{\infty} \int s_i(x,y) s_j(x,y) dxdy. \tag{3.15}$$

The N equations in Eq. (3.14) can be expressed more succinctly as:

$$\boldsymbol{H a} = \boldsymbol{c} \tag{3.16}$$

Where $\boldsymbol{a} = [a_1, a_2, ..., a_N]^T$, $\boldsymbol{c} = [c_1, c_2, ..., c_N]^T$. If we express the training images in a vector $\boldsymbol{S} = [s_1, s_2, ..., s_N]$, the SDF function changes to an N x N matrix

$$\boldsymbol{R} = \boldsymbol{Sa} \tag{3.17}$$

With Eqs. (3.16) and (3.17), the solution vector $\boldsymbol{R}$ can be written as

$$\boldsymbol{R_{SDF}} = \boldsymbol{SH^{-1}c} \tag{3.18}$$

Noting $\boldsymbol{H} = \boldsymbol{S^T S}$, $\boldsymbol{R_{SDF}}$ will be

$$\mathbf{R_{SDF}} = \mathbf{S(S^T S)^{-1} c} \tag{3.19}$$

The computed SDF are then fed into an optical spatial light modulator incorporated into a correlator to produce the optical reference signal.

3.2 Circular Harmonic Filters and Rotational Invariance

The circular harmonic expansion (Arsenault, 1982) of an object can be described by:

$$f(r,\vartheta)=\sum_{N=-\infty}^{N=\infty} f_N(r)\exp(iN\vartheta) \tag{3.20}$$

with

$$f_N(r)=\frac{1}{2\pi}\int_0^{2\pi} f(r,\vartheta)\exp(-iN\vartheta) \tag{3.21}$$

where $f(r,\vartheta)$ is the object with polar co-ordinates, N is an integer and $f_N(r)\exp(iN\vartheta)$ is the Nth circular harmonic. The circular harmonic filters are formed by taking one or a few circular harmonic components. For a single circular harmonic component, suppose we chose the Mth circular harmonic component to form the filter. Its Fourier transform in a polar co-ordinate system (ρ,φ) can be expressed as:

$$F_M(\rho,\varphi)=F\left[f_M(r)\exp(iM\vartheta)\right]=F_M(\rho)\exp(iM\varphi) \tag{3.22}$$

with

$$\begin{aligned} F_M(\rho)&=(-i)^M 2\pi\int_0^{\infty} f_M(r)J_M(2\pi r\rho)rdr \\ &=\left|F_M(\rho)\right|\exp\left[i\alpha_M(\rho)\right] \end{aligned} \tag{3.23}$$

where F denotes the Fourier transform, $J_M(r)$ is the M-order Bessel function, $|F_M(\rho)|$ and $\alpha_M(\rho)$ is the amplitude and the phase of $F_M(\rho)$, respectively.

A phase-only version of the circular harmonic filter can be obtained by setting the modulus $|F_M(\rho)|$ in Eq. (3.22) to unity, and the filter becomes

$$F_{M(POF)}(\rho,\varphi) = \exp[i\alpha_M(\rho)]\exp(iM\varphi) \tag{3.24}$$

Suppose the circular harmonic filters are inserted in a correlator, and the input is a ϑ_0 rotated version of the object. The complex light distribution at the centre of the output plane of the correlator can be described by:

$$\begin{aligned} A_M(0,0) &= \int_0^{\infty}\int_0^{2\pi}\sum_{N=0}^{\infty} F_N(\rho)\exp(iN\varphi)F_M^*(\rho)\exp(-iM\varphi)\exp(iN\vartheta_0)\rho d\rho d\varphi \\ &= 2\pi\exp(iM\vartheta_0)\int_0^{\infty}|F_M(\rho)|^2\rho\, d\rho \end{aligned} \tag{3.25}$$

It can be seen that the intensity at the centre of the output plane is ϑ_0 independent, which ensures the rotation-invariance.

For a filter containing k circular harmonic components, the filter is denoted by

$$f_k(r,\vartheta) = \sum_k f_{N_k}(r)\exp(iN_k\vartheta) \tag{3.26}$$

With a ϑ_0 rotation of the object, the amplitude at the centre of the output plane should be

$$A_k(0,0) = \sum_k A_{N_k}(0,0) = \sum_k \left| A_{N_k}(0,0) \right| \exp(iN_k \vartheta_0) \tag{3.27}$$

Because of the different phase factors in each component, the vector result varies with the target rotation angle ϑ_0. This means that the correlation output intensity $\left|A_k(0,0)\right|^2$ is influenced by the target rotation. Generally speaking, the larger the rotation angle ϑ_0, the larger its influence on the output correlation peak. Also the more circular harmonic components that are employed to form the filter, the more the output correlation peak depends on the rotation angle of the object.

3.3 Circular Harmonic Quantized Amplitude Compensated Matched Filters

In 1984 Horner proposed the phase-only filter which has been shown to exhibit two important features: a simple structure with no absorption and excellent performance in terms of high Horner efficiency and good discrimination. Since then, various kinds of spatial filters have been developed. Among them, the quantized amplitude-compensated matched filter (QACMF) was proposed (Wang, 1993) which combines a simple structure with excellent performance. It possesses an excellent discrimination capability (comparable to the amplitude-compensated matched filter), and a structure only slightly more complex than the binary filter. This filter can again be easily implemented either with an amplitude-modulating spatial light modulator or by computer-generated holography methods.

However the QACMF yields three diffraction terms when it is used in a correlator: the correlation, the convolution and the zero-order terms (Wang, 1993). Only the correlation term plays a useful role in pattern recognition and the others either give rise to false alarms (the convolution term) or background noise (the zero-order term). One solution is

to incorporate an appropriate frequency carrier in the filter design to shift the correlation term away from the others.

For rotation-invariant pattern recognition the circular harmonic expansion method has been applied to the matched spatial filter, the phase-only and the binary phase-only filters, the amplitude-compensated matched filter and the amplitude-modulated phase-only filter (Hsu, 1982; Leclerc, 1989; Sun, 1990). With the circular harmonic binary phase-only filter or the circular harmonic binary filter, the superposition of the correlation term and the convolution term destroys the rotation invariant property if non-zero orders of the circular harmonic expansion are used (Leclerc, 1989). Therefore the frequency carrier concept discussed above plays a significant role in this case.

Here we apply the circular harmonic expansion method to the QACMF to achieve rotation invariant recognition. The proposed filter has three grey-levels and the zero-order, first-order and second-order terms of the circular harmonic expansion were selected to implement a number of spatial filters. An appropriate frequency carrier was used to separate the correlation term from the others as discussed above and the performance of the proposed filters were compared with the corresponding circular harmonic binary filter (CHBF).

In the computer simulations the performance of the CHQACMF and the CHBF were compared. Both are amplitude filters with only a few grey levels (3 and 2 respectively). The reference object selected is the English letter "E", chosen for its lack of circular symmetry. In the comparison, the zero-order, the first-order and the second-order circular harmonic components were selected sequentially to form the filters. The performance criteria used were the peak correlation intensity PCI (with a scaling of 0-255), the signal-to-noise ratio SNR and the Horner efficiency η_H. The SNR is defined as the ratio of the peak correlation intensity to the mean intensity outside the 50% peak value in the correlation plane and as such represents the sharpness of the correlation peak and consequently determines the probability of an error in detection. The Horner efficiency is defined as the ratio of the peak correlation intensity to the total energy in the

input object which in turn determines the detectability of the correlation peak. A PC running the 'IDL' package was used for the simulations.

Table 3.1 presents the computer simulation results. For each filter, the correlation results for zero and a $\pi/4$ rotation of the object are presented. Column 2 lists the type of spatial filters. CHBF denotes the circular harmonic binary filter and CHQACM denotes the circular harmonic quantized amplitude-compensated matched filter. Columns 3-8 list the rotation angle of the object, the peak correlation intensity, the signal-to-noise ratio, the Horner efficiency, the average of the signal-to-noise ratio for the two rotation angles, and the average of the Horner efficiency for the two rotation angles. We can see that there is a trade-off between the Horner efficiency and the signal-to-noise ratio with the different filters.

	Filter	Angle	CPI	SNR	$\eta_H(\%)$	$\overline{\text{SNR}}$	$\overline{\eta_H}(\%)$
1	Zero-order CHBF	0	255	66	0.57	60	0.52
		$\pi/4$	204	53	0.46		
2	Zero-order CHQACM	0	196	82	0.44	78	0.43
		$\pi/4$	185	74	0.42		
3	First-order CHBF	0	123	33	0.27	32	0.27
		$\pi/4$	119	32	0.26		
4	First-order CHQACM	0	102	43	0.23	40	0.22
		$\pi/4$	97	38	0.22		
5	Second-order CHBF	0	110	40	0.25	36	0.23
		$\pi/4$	97	32	0.22		
6	Second-order CHQACM	0	97	58	0.22	52	0.20
		$\pi/4$	80	47	0.18		

Table 3.1. The computer simulation results with various circular harmonic expansion filters.

CHBF : Circular Harmonic Binary Filter

CHQACM : Circular Harmonic Quantized Amplitude Compensated Matched filter

CPI : Correlation Peak Intensity

SNR : Signal-to-Noise Ratio

η_H : Horner Efficiency

$\overline{SNR}$: Average SNR for the two rotation angles

$\overline{\eta_H}$: Average Horner efficiency for the two rotation angles

With the zero-order CHQACMF listed in row 2, the Horner efficiency is on average 0.43 %, which represents a 17 % reduction compared with the zero-order CHBF listed in row 1. The signal-to-noise ratio of the CHQACMF however has an average value of 78, which represents a 30 % improvement over the CHBF as listed in row 1.

With the first-order CHQACMF listed in row 4, the Horner efficiency is on average 0.20 %, which represents a 19 % reduction as compared with the first-order CHBF listed in row 3; however the signal-to-noise ratio of the CHQACMF is 40, which represents a 25 % improvement over the CHBF.

Finally with the second-order CHQACMF listed in row 6, the Horner efficiency is on average 21 %, which represents a 13 % reduction as compared with the second-order CHBF listed in row 5. The signal-to-noise ratio however of the CHQACMF is 52 giving a 44 % improvement over the CHBF.

The trade-off seems to depend on the circular harmonic order used in the filter design. With the second-order circular harmonic component the amplitude compensation procedure exhibits the best trade-off between signal-to-noise ratio and Horner efficiency. To illustrate the filters' performance more clearly three-dimensional plots of the correlation results are presented in Figs. 3.1 to 3.3. Fig. 3.1 shows the correlation results for the zero-order circular harmonic filters, (a) was obtained with the CHBF and (b) was obtained with the CHQACMF. Similarly, Fig. 3.2 and Fig. 3.3 present the correlation results for the first-order and the second-order circular harmonic filters respectively. Again, (a) was obtained with the CHBF and (b) was obtained with the CHQACMF. All plots correspond to zero rotation of the object. These plots show that the signal-to-noise ratio is improved by the amplitude compensation technique.

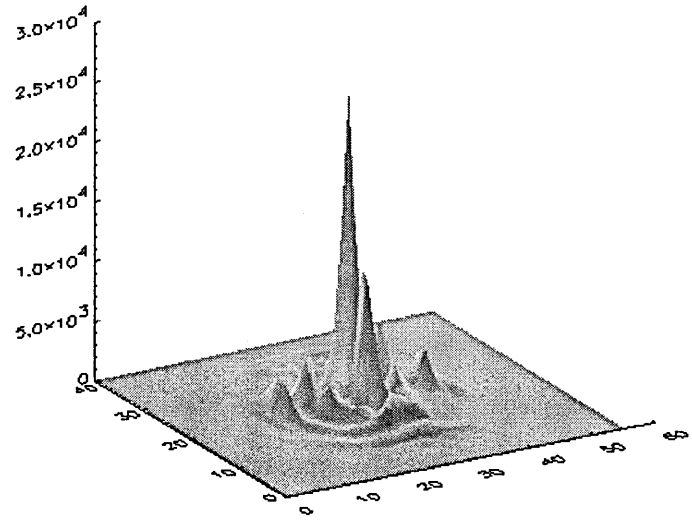

(a)

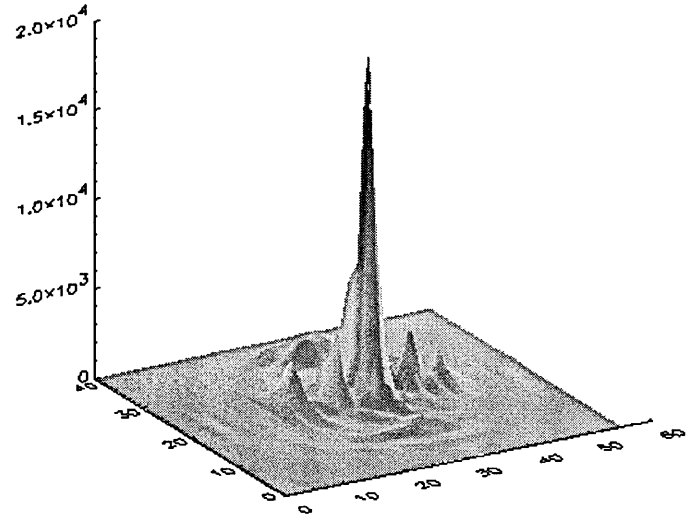

(b)

Fig. 3.1. Three dimensional plots of the correlation results with the zero-order circular harmonic filters (0° rotation). (a) with the circular harmonic binary filter, (b) with the circular harmonic quantized amplitude-compensated matched filter.

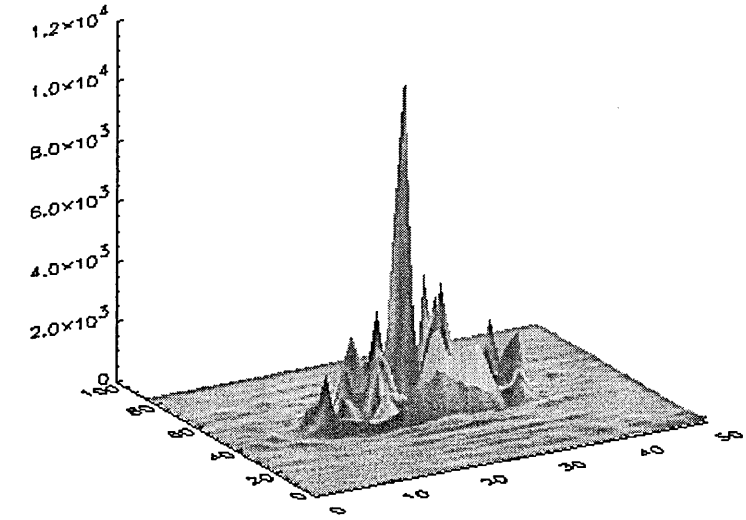

(a)

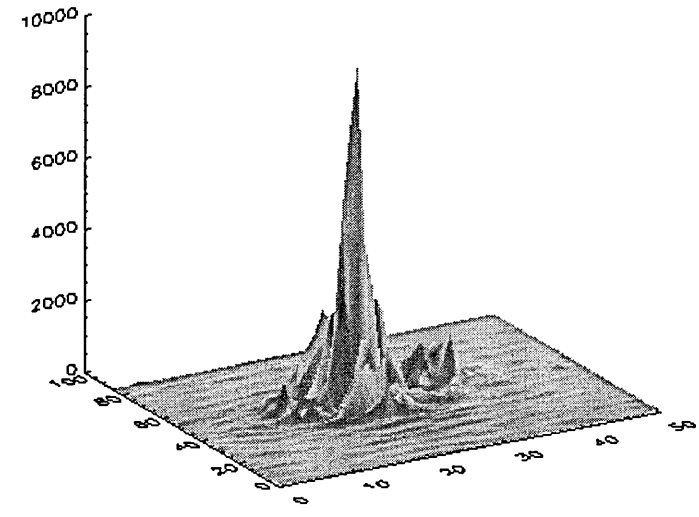

(b)

Fig. 3.2 Three dimensional plots of the correlation results with the first-order circular harmonic filters (0° rotation). (a) with the circular harmonic binary filter, (b) with the circular harmonic quantized amplitude-compensated matched filter.

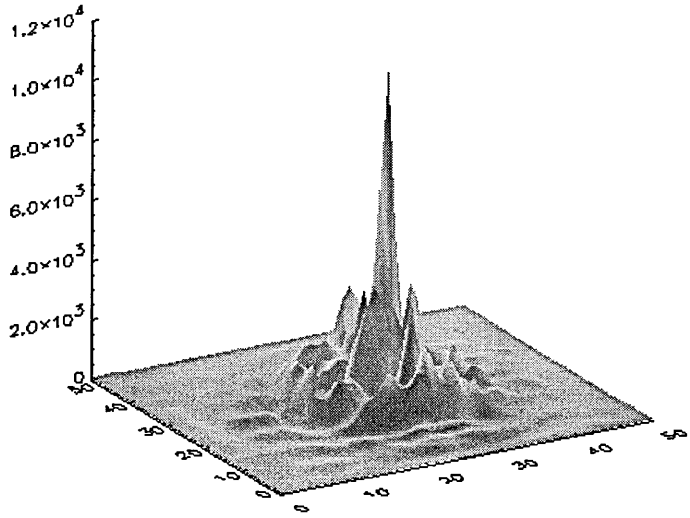

(a)

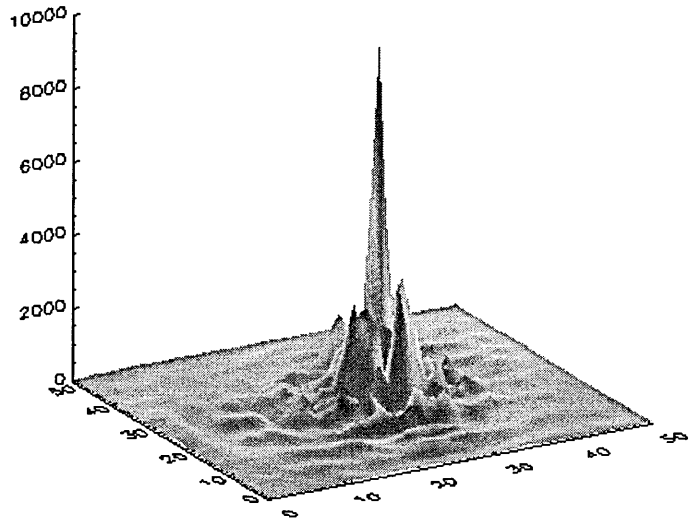

(b)

Fig. 3.3. Three dimensional plots of the correlation results with the second-order circular harmonic filters (0° rotation). (a) with the circular harmonic binary filter, (b) with the circular harmonic quantized amplitude-compensated matched filter.

The quantized amplitude-compensated matched filter is characterized by its simple structure, with only a few discrete grey levels, and excellent signal-to-noise ratio performance which determines the probability of an error in recognition which can be regarded as one of the most important performance criterion. In this work we have extended this idea to circular harmonic expansion filters for rotation-invariant recognition. It is shown that there is a trade-off between the signal-to-noise ratio and the Horner efficiency with the amplitude compensation technique. The trade-off is dependent on the circular harmonic order, and with the second-order circular harmonic quantized amplitude-compensated matched filter an improvement of 44 % in the signal-to-noise ratio was obtained with only a 13 % reduction in Horner efficiency as compared with the second-order circular harmonic binary filter.

3.4 Fresnel Lens-encoded Quantized Amplitude Compensated Filters

In the development of spatial filters for object recognition, every effort has been made to improve the filter's performance as well as simplifying the filter structure. As mentioned above, after the matched filter and phase only filter, subsequently many different kinds of spatial filter have been suggested. Among them the amplitude compensated matched filter (ACMF) and the amplitude-modulated phase-only filter possess excellent performance in terms of discrimination. To simplify the filter design so as to enable the use of an amplitude-modulating spatial light modulator, the quantized amplitude compensated matched filter (QACMF), which is an amplitude filter with only a few discrete grey levels, was developed and has been shown to possess excellent performance. This filter can be easily implemented either with an amplitude-modulating spatial light modulator (SLM) or by computer-generated holography methods, which are then sent to the SLM directly from a computer. However, the QACMF generates three diffraction terms when it is used in a correlator, namely: the correlation term, the convolution term and the zero-order diffraction term. The convolution term however can be thought of as a correlation of the reference object (a real function) with an inverted version of itself. Therefore with an inverted object as the input, the convolution term has

the same peak intensity as the correlation term would have when using the original object. This can cause a faulty recognition when an inverted version of the reference object is presented as the input. To spatially separate the three terms of the filter an appropriate frequency carrier is usually incorporated in the design of the filter; the frequency carrier shifts the correlation region away from the origin and off-axis. Fresnel lens-encoding is however an alternative technique which can be used to spatially separate the correlation region from the others (Davis, 1989, 1990). Instead of shifting the correlation region away from the origin, it renders the correlation wavefront convergent and the other wavefronts divergent by introducing a Fresnel lens phase factor. As a result the three terms at the output plane are all on axis, but with only the profile of the correlation term unchanged whilst the others are flattened or suppressed.

The method of circular harmonic expansion has been applied to phase-only and binary phase-only filters (Rosen, 1988), it has also been applied to the Fresnel lens-encoded binary phase-only filter (Leclerc, 1991). It is obvious that the ambiguity in detection, when the correlation and the convolution diffraction terms are superimposed, has no relevance when considering rotationally invariant recognition. The inverted version of an object is simply a 180° rotation of the original object and it is expected to give the same correlation peak intensity as the original object. However the problem is that if non-zero orders of the circular harmonic expansion are used, the superposition of the correlation and the convolution diffraction terms will destroy the rotation invariance property (Davis, 1990).

Here we apply the Fresnel lens encoding technique to the quantized amplitude compensated matched filter for the isolation of the correlation diffraction term, and make a comparison with the Fresnel lens-encoded binary filter. It is shown that the QACMF has a higher signal-to-noise ratio compared with the binary filter, with some loss, however, in Horner efficiency. We then extend this idea to including a circular harmonic expansion for rotationally invariant recognition. The first-order and the zero-order terms of the circular harmonic expansion were used to form the Fresnel lens-encoded filters. It

is shown by computer simulations that the Fresnel lens-encoded quantized amplitude-compensated matched filter possesses excellent performance in terms of discrimination.

3.5.1 Fresnel lens-encoded quantized amplitude-compensated matched filter

Suppose the Fourier transform of a real object $f(x, y)$ is expressed as:

$$F(p,q) = |F(p,q)| \exp[i\varphi(p,q)] \tag{3.28}$$

where (p, q) is the spatial frequency co-ordinates, $|F(p,q)|$ is the Fourier amplitude spectrum and $\varphi(p,q)$ is the Fourier phase spectrum. The Fresnel lens-encoded binary filter (also called the Fresnel lens-encoded amplitude-encoded binary phase-only filter) takes the form (Davis, 1989):

$$H_{BF}(p,q) = \frac{1}{2}\{1 + BIN[Z_1^* F^*(p,q) + Z_1 F(p,q)]\} \tag{3.29}$$

with

$$Z_1 = \exp\left[\frac{-i2\pi(\alpha^2 + \beta^2)}{2z\lambda}\right] \tag{3.30}$$

where (α, β) is the spatial co-ordinate at the Fourier plane, z is the focal length of the Fourier transform lens, λ is the wavelength and BIN indicates the binarization operation of a complex function:

$$BIN[G(p,q)] = \begin{cases} 1 & \text{when phase angle } \varphi(p,q) \le \pi \\ -1 & \text{otherwise} \end{cases} \tag{3.31}$$

with G(p,q) a complex function. It is clear that the Fresnel lens-encoded binary filter $H_{BF}(p,q)$ has a binary value of 0 or 1. Now the Fresnel lens-encoded quantized amplitude matched filter, with three-grey level quantization, can be expressed as:

$$H_{QACM}(p,q)=\begin{cases} H_{BF}(p,q) & \text{when } |F(p,q)| \le F_1 \\ \dfrac{F_1}{F_2}H_{BF}(p,q) & \text{when } F_1 < |F(p,q)| \le F_2 \\ 0 & \text{otherwise} \end{cases} \tag{3.32}$$

where F_1 and F_2 are threshold values which are chosen by examining the histogram of the Fourier amplitude spectrum of the object. It can be seen that $H_{QACM}(p,q)$ takes the form of a Fresnel lens-encoded binary filter when the modulus of the Fourier amplitude spectrum is less than a threshold value, and it has additional appropriate absorptive factors for other ranges of the modulus of the Fourier amplitude spectrum. Note that $H_{BF}(p,q)$ is a binary filter with grey levels of 0 and 1, $H_{QACM}(p,q)$ is therefore a three grey level amplitude filter. When the Fresnel lens-encoded filter is used in a correlator, an additional lens with a phase transformation given by Z_1 should be inserted just behind the filter.

3.5.2 Fresnel lens-encoded circular harmonic quantized amplitude-compensated matched filter

As discussed in the last section, the circular harmonic expansion of a function can be expressed as:

$$f(r,\vartheta)=\sum_{N=-\infty}^{N=\infty} f_N(r)\exp(iN\vartheta) \tag{3.33}$$

where

$$f_N(r) = \frac{1}{2\pi}\int_0^{2\pi} f(r,\vartheta)\exp(-iN\vartheta)d\vartheta \tag{3.34}$$

For rotationally invariant object recognition, one or more circular harmonic terms are used to form the spatial filter. Suppose that the Mth circular harmonic term is chosen for the spatial filter. Its Fourier transform can be expressed as:

$$F[f_M(r)\exp[iM\vartheta]] = |F_M(p,q)|\exp[i\varphi_M(p,q)] \tag{3.35}$$

where $|F_M(p,q)|$ is the Fourier amplitude spectrum of the Mth circular harmonic term and $\varphi_M(p,q)$ is the Fourier phase spectrum. The Fresnel lens-encoded Mth circular harmonic binary filter $H_{BF}(p,q)|_M$, referring to equation (3.29), takes the form:

$$H_{BF}(p,q)|_M = \frac{1}{2}\{1 + BIN[Z_1^* F_M^*(p,q) + Z_1 F_M(p,q)]\} \tag{3.36}$$

whereas the Fresnel lens-encoded Mth circular harmonic quantized amplitude-compensated matched filter, with three grey level quantization, takes the form:

$$H_{QACM}(p,q)|_M = \begin{cases} H_{BF}(p,q)|_M & \text{when } |F_M(p,q)| \le F_{M1} \\ \frac{F_{M1}}{F_{M2}} H_{BF}(p,q)|_M & \text{when } F_{M1} < |F_M(p,q)| \le F_{M2} \\ 0 & \text{otherwise} \end{cases} \tag{3.37}$$

where F_{M1} and F_{M2} are again appropriate threshold values chosen according to the Fourier amplitude spectrum of the Mth circular harmonic component of the object. It is to be expected that the threshold values will be different according to the circular harmonic order used, and in practice they are chosen by inspection of the histograms of the Fourier spectrum given by equation (3.37).

3.5.3 Computer simulation results

We have investigated the performance of the proposed spatial filters by means of computer simulations. An English letter "E" was created, in a 128 × 128 pixel array and used as the reference object. The Fresnel lens-encoded quantized amplitude-compensated matched filter was compared with the Fresnel lens-encoded binary filter, since both are amplitude-modulated with only a few discrete grey levels. The performance criteria used are the peak correlation intensity PCI, the Horner efficiency η_H, and the signal-to-noise ratio SNR. The peak correlation intensity is scaled to a maximum value of 255 determined by the 8 bit grey level pixel resolution. The Horner efficiency is defined as the ratio of the peak correlation intensity to the total energy in the input object, which determines the detectability of the correlation peak. The signal-to-noise ratio is defined as the ratio of the peak intensity to the mean intensity outside a 50 % peak value in the output, which represents the sharpness of the correlation peak and determines the chance of an error detection in pattern recognition. A PC running the "IDL" software was used to perform the simulations.

A. Performance of the Fresnel lens-encoded quantized amplitude-compensated matched filter

Three grey levels are used to generate the filter, and the threshold levels are chosen to optimise the filter performance. There is always a trade-off between discrimination and Horner efficiency and the trade-off depends considerably on the threshold levels. Here we chose two threshold values of 1/12 and 1/3 of the maximum absolute value of the Fourier amplitude spectrum, which give a high signal-to-noise ratio without a dramatic loss in Horner efficiency. It is possible that a better performance could be obtained with more grey levels, but it is difficult to optimise many threshold values simultaneously, and the filter structure would of course be surely more complicated with more grey levels.

Table 3.2 presents the computer simulation results for the performance of the Fresnel lens-encoded quantized amplitude-compensated matched filter which is compared with

the Fresnel lens-encoded binary filter. Column 1 lists the types of spatial filters. BF denotes the Fresnel lens-encoded binary filter and QACMF denotes the Fresnel lens-encoded quantized amplitude compensated matched filter. Columns 2-4 list the peak correlation intensity, the Horner efficiency and the signal-to-noise ratio, respectively.

Filter	PCI	η_H (%)	SNR
BF	255	3.5	179:1
QACMF	124	1.7	727:1

Table 3.2. Computer Simulation Results with Different Fresnel Lens-Encoded Filters

We can see that the Fresnel lens-encoded quantized amplitude-compensated matched filter exhibits a higher signal-to-noise ratio of 727:1 which is more than four times that of the Fresnel lens-encoded binary filter. Considering that the signal-to-noise ratio is perhaps the most important parameter in pattern recognition, this improvement is significant. The Horner efficiency is about 50 % of that of the Fresnel lens-encoded binary filter. This reduction in Horner efficiency can however be compensated for in a practical situation by, for example, the use of a more sensitive detector. These results show that the amplitude-compensation procedure in Fresnel lens-encoded filters plays a very important role in improving the filter performance. It can be understood as follows: with the Fresnel lens-encoding technique the three diffraction terms are superimposed but only the correlation peak profile is unaffected whereas the convolution and the zero-order diffraction terms are flattened and act as background noise. The absorption resulting from the amplitude compensation procedure takes place mostly at low spatial frequencies; it thus serves two functions: first, it flattens the Fourier amplitude spectrum at the filter plane and so sharpens the correlation peak; second, it absorbs the background noise, further reducing the influence of the zero-order and the convolution diffraction terms. The combination of sharpening the correlation peak and the reduction of background noise enhances the signal-to-noise ratio significantly. To illustrate the improvement, three

dimensional plots of the auto correlation results are presented in Fig. 3.4. Fig. 3.4 (a) was obtained with the Fresnel lens-encoded binary filter and (b) was obtained with the Fresnel lens-encoded quantized amplitude compensated matched filter. It is obvious that the signal-to-noise ratio in (b) is much higher than that in (a). For comparison we used the same reference image to form a Fresnel lens-encoded ternary phase-amplitude filter, which also has three levels. For the same kind of correlation, the Horner efficiency and signal-to-noise ratio are 12% and 443:1, respectively. It can be seen that the ternary filter has a much higher Horner efficiency and quite good SNR, although not as good as the QACMF. However, the requirements of the spatial light modulator for the ternary filter are quite different to that for the QACMF, so it is perhaps not reasonable to compare it too closely with the QACMF.

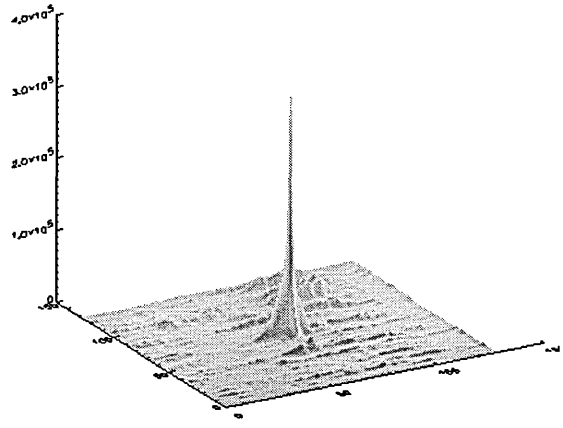

(a)

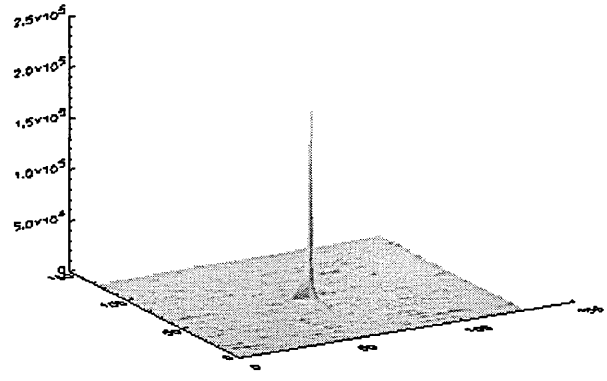

(b)

Fig. 3.4 3-D plots of the auto correlation with the different Fresnel lens-encoded filters. (a) with the Fresnel lens-encoded binary filter, (b) with the Fresnel lens-encoded quantized amplitude-compensated matched filter.

B. Performance of the Fresnel lens-encoded quantized amplitude-compensated matched filter with circular harmonic expansion

	Filter	CPI	SNR	η_H(%)
1	Zero-order CHBF	255	113:1	0.30
2	Zero-order CHQACM	212	131:1	0.25
3	First-order CHBF	171	78:1	0.20
4	First-order CHQACM	124	99:1	0.15

Table 3.3. Computer Simulation Results with Different Fresnel lens-Encoded circular Harmonic Expansion Filters

For rotationally invariant correlation using a circular harmonic expansion, we have calculated the Fresnel lens-encoded binary filter and quantized amplitude compensated matched filter according to equations of (3.36) and (3.37). In this simulation, the zero-order and the first-order circular harmonic terms were chosen to form the spatial filters. For each circular harmonic term, the expansion centre was chosen to obtain a maximum correlation peak in the output plane. Table 3.3 presents the computer simulation results. CHBF in rows 2 and 4 denotes the Fresnel lens-encoded circular harmonic binary filter, and CHQACMF in rows 3 and 5 denotes the Fresnel lens-encoded circular harmonic quantized amplitude-compensated matched filter. We can see that with a circular harmonic expansion, the effect of the amplitude compensation procedure on the signal-to-noise ratio is not as dramatic as before. With the first-order circular harmonic expansion, the signal-to-noise ratio is enhanced from 78:1 in row 4 to 99:1 in row 5 with a factor of 26 % enhancement, by the amplitude compensation procedure. With the zero-order circular harmonic expansion, the signal-to-noise ratio is enhanced from 113:1 in row 2 to 131:1 in row 3 a factor of only 18 %. Correspondingly, the Horner efficiency decreases only slightly. It drops from 0.29 % in row 2 to 0.25 % in row 3 with the zero-order circular harmonic expansion, and it drops from 0.20 % in row 4 to 0.15 % in row 5 with the first-order circular harmonic expansion. Fig. 3.5 presents three dimensional plots

corresponding to the results in Table 3.3, (a) was obtained with the Fresnel lens-encoded zero-order circular harmonic binary filter, (b) was obtained with the Fresnel lens-encoded zero-order circular harmonic amplitude-compensated matched filter, (c) was obtained with the Fresnel lens-encoded first-order circular harmonic binary filter, and (d) was obtained with the Fresnel lens-encoded first-order circular harmonic amplitude-compensated matched filter. It can be seen by inspection of the figures that the signal-to-noise ratio is improved slightly by the amplitude compensation procedure as detailed in Table 3.3. For comparison, we also used the higher order circular harmonic orders to form spatial filters. We found that for high orders the differences between the Fresnel lens-encoded binary filter and the Fresnel lens-encoded QACMF get smaller. It seems that the effect of the amplitude compensation technique decreases with an increase in the circular harmonic order. For high orders, the Fourier amplitude spectra are very weakly employed, and this is perhaps part of the reason why they do not affect the correlation results dramatically.

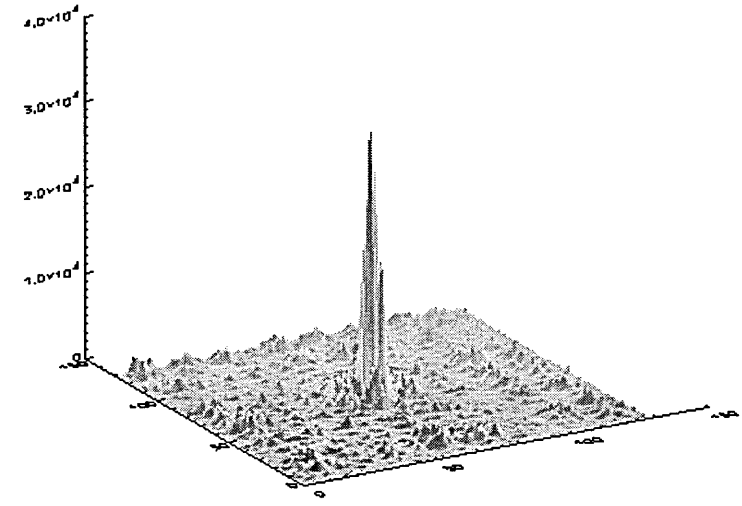

(a)

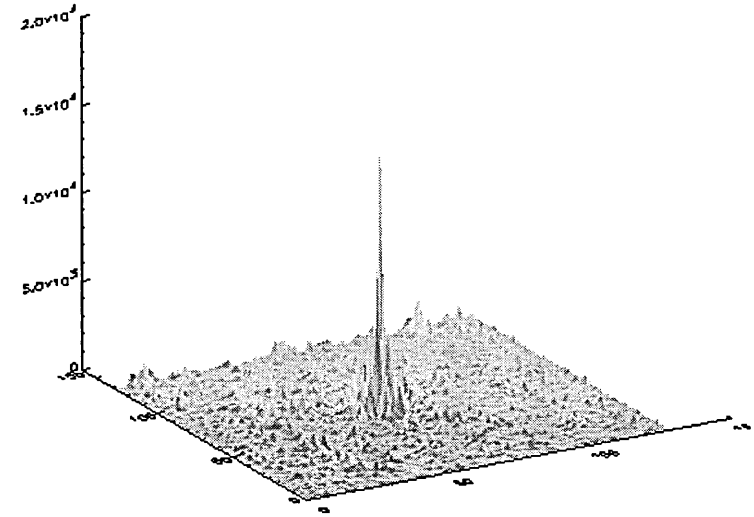

(b)

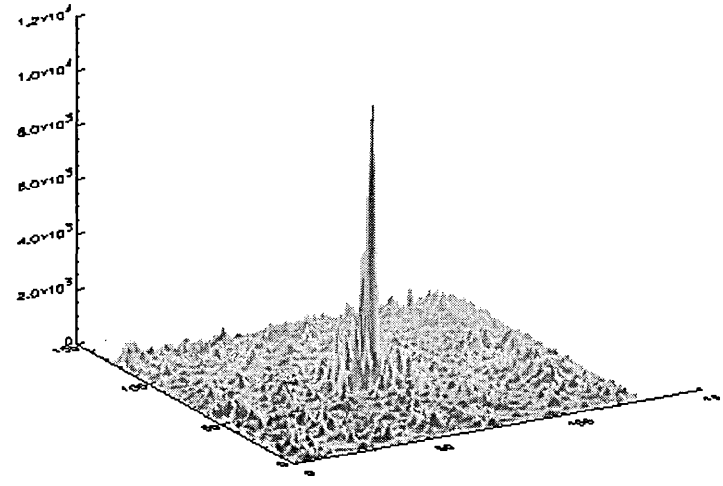

(c)

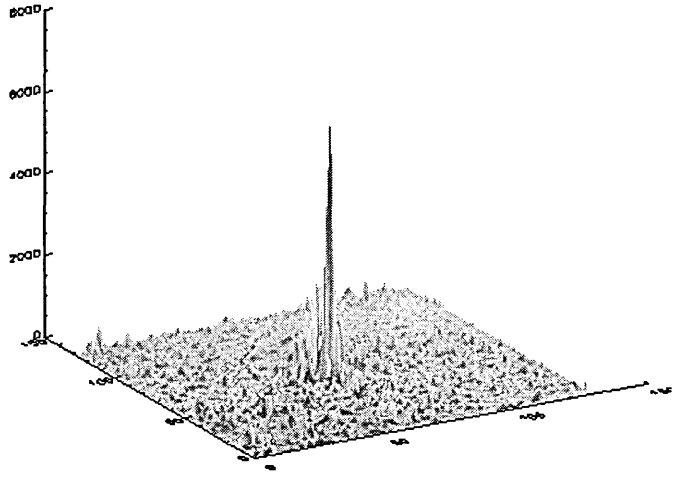

(d)

Fig. 3.5 3-D plots of the auto correlation with the different Fresnel lens-encoded circular harmonic expansion filters (0° rotation). (a) with the Fresnel lens-encoded zero-order binary filter, (b) with the Fresnel lens-encoded zero-order quantized amplitude-compensated matched filter, (c) with the Fresnel lens-encoded first-order binary filter, (d) with the Fresnel lens-encoded first-order quantized amplitude-compensated matched filter.

In this section, we have applied the quantized amplitude technique to the Fresnel lens-encoded binary filter and created the Fresnel lens-encoded quantized amplitude-compensated matched filter to improve filter performance. The proposed filter is amplitude modulated with only three discrete grey levels compared with two levels in the Fresnel lens-encoded binary filter and thus could be implemented on an amplitude-modulation spatial light modulator in a real-time application. In a comparison with the Fresnel lens-encoded binary filter, the proposed spatial filter possesses an excellent signal-to-noise ratio which is a significant improvement because the signal-to-noise ratio determines the probability of a false detection. Therefore it is considered to be a strong candidate particularly in real-time applications. The quantized amplitude compensation technique has also been applied to the Fresnel lens-encoded circular harmonic binary filter for rotationally invariant recognition. The zero-order and the first-order of the circular harmonic terms were selected to form the filters in the simulations. The effect of the quantized amplitude compensation procedure on the Fresnel lens-encoded circular harmonic binary filter seems not so significant; however, an improvement of 30 % in the signal-to-noise ratio when using the first-order circular harmonic term has been obtained.

Chapter 3: References

J.A. Davis, D.M. Cottrell, R.A. Lilly and S.W. Connely, "Multiplexed phase-encoded lenses written on spatial light modulators", Opt. Lett., **14** (1989) 420-422.

J.A. Davis, D.M. Cottrell, J.E. Davis and R.A. Lilly, "Fresnel lens-encoded binary phase-only filters for optical pattern recognition", Opt. Lett., **14** (1989) 659-661.

J.A. Davis, S.H. Drayton, D.M. Cottrell and J.E. Davis, "Improved synthetic discriminant function performance using Fresnel lens-encoded binary phase-only filters", Appl. Opt., **29** (1990) 2594-2599.

J.A. Davis, L.R. York and D.M. Cottrell, "Rotationally invariant Fresnel lens-encoded circular harmonic binary phase-only filters", Appl. Opt., **30** (1991)1820-1825

J.D. Downie, "Design of optimal binary phase and amplitude filters for maximization of correlation peak sharpness", Opt. Lett., **16** (1991) 508-510.

D.L. Flannery, J.S. Loomis and M.E. Milkovich, "Transform-ratio ternary phase-amplitude filter formulation for improved correlation discrimination", Appl. Opt., **27** (1988) 4079-4083.

C.F. Hester, and D. Casasent, " Multivariant technique for multiclass pattern recognition," Appl. Opt., 19, 1758-1761 (1980).

J. L. Horner, "Light Utilization in Optical Correlators", Appl. Opt. 21, 4511-4514 (1982).

J.L. Horner, and P.D. Gianino, "Phase-only matched filter,", Appl. Opt. 23, 812-816 (1984).

Y.-N. Hsu, H.H. Arsenault and G. April, "Rotation-invariant digital pattern recognition using circular harmonic expansion", Appl. Opt., **21** (1982) 4012-4015.

Y.-N. Hsu and H.H. Arsenault, "Optical pattern recognition using circular harmonic expansion", Appl. Opt., **21** (1982) 4016-4019.

B. Javidi, and J.L. Horner, "Real-time optical information processing", Chapter 2, 4, Academic Press, Inc, California, 1994.

L. Leclerc, Y. Sheng and H.H. Arsenault, "Rotation invariant phase-only and binary phase-only correlation", Appl. Opt., **28** (1989) 1251-1256.

L. Leclerc, Y. Sheng and H.H. Arsenault, "Optical binary phase-only filters for circular harmonic correlations", Appl. Opt., **30** (1991) 4643-464

G.G. Mu, X.M. Wang and Z.Q. Wang, "Amplitude-compensated matched filtering", Appl. Opt., **27** (1988) 3461-3464.

J. Rosen and J. Shamir, "Circular harmonic phase filters for efficient rotation-invariant pattern recognition", Appl. Opt., **27** (1988) 2895-2899.

Y. Sun, Z.Q. Wang, and G. Mu, "Amplitude compensated matched filers using circular harmonic expansion and a Mellin transform," Appl. Opt. 29, 4779-4783 (1990).

Z.Q. Wang, C.M. Cartwright, W.A. Gillespie and C. Soutar, "Evaluation of the performance of the amplitude-compensated matched filer with different threshold values", Optik, **90** (1992) 139-143.

Z.Q. Wang, C.M. Cartwright, W.A. Gillespie and C. Soutar, "An optical matched filter using a quantized amplitude compensation technique", Optik, **94** (1993) 78-82.

H. Zhang, Z.Q. Wang, C.M. Cartwright, M.S. Ding, N.J. Cook, and W.A. Gillespie, "A circular harmonic quantized amplitude compensated matched filter", Optik **109** (3), 119-123 (1998).

Chapter 4. Photorefractive BSO in Holography

The photorefractive crystal bismuth silicon oxide (BSO) has been widely used as a dynamic holographic medium in real-time optical correlation (Pichon, 1984). It has the advantages of a fast response, good optical quality over a large surface area, high spatial frequency response, and a low writing and erasing energy. All of these make it suitable for real-time applications. It is well known that when two beams intersect inside a photorefractive crystal, an optical refractive-index grating is formed by the excitation of photo-electrons which migrate by diffusion and drift forming a space-charge modulation which modifies the refractive index via the linear electro-optical effect. The mechanism is as follow: the writing beams produce a photo-excited charge-carrier distribution which corresponds to the intensity distribution which produces a space–charge field; this field modulates the refractive index of the crystal via the linear electro-optic effect and forms the refractive index grating. In pattern recognition, this effect can be used to record the joint power spectrum in the Fourier plane to realize real-time operation. In this chapter the basic theory of refractive index modulation and other properties, and its application in optical correlation are introduced.

4.1 Photo-Induced Refractive Index Modulation

Photorefractive crystals can be described as electro-optic crystals which are also photoconductive. Under certain conditions light incident on these crystals can therefore cause a change in the crystal's refractive index. In the simple model assumed here the crystal is regarded as having one type of mobile carrier, electrons (e^-), and two types of impurities, donors (N_D) and acceptors (N_A^-) which reside somewhere deep in the band gap, as shown in Fig. 4.1. Electrons can be excited to the conduction band by photons of energy $\hbar\omega$, ionising a donor atom in the process. The conduction band electrons may be transported by drift and diffusion and then recombine with ionised donors. Some of the donor atoms and all the acceptor atoms are assumed to be ionised, and the acceptor ions play no active part in the excitation and recombination process but are present to ensure

that a large number of donors are ionised in the dark. So the variables of the model are n_e, the density of electrons, N_D the density of donors, N_D^+ the density of ionised donors, and N_A^- the density of ionised acceptors.

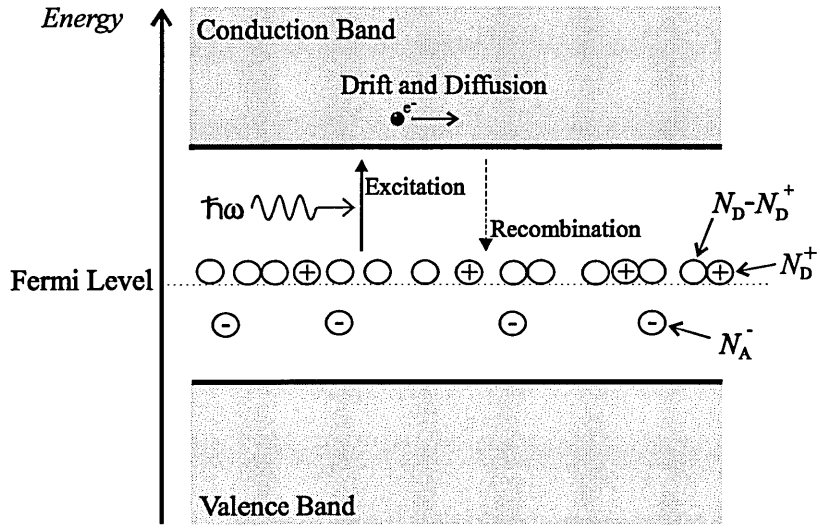

Fig.4.1 Band Transport Model of Photorefractivity.

The model describing the formation of the grating is best described by considering the simplest experimental situation of two plane waves incident symmetrically on the crystal at angles $\pm\theta$. The photorefractive process is driven by the intensity distribution caused by the interference of these two beams, of intensity I_1 and I_2.

This intensity distribution can be written as

$$I = I_0\left(1+m\cos(Kz+\phi_0)\right) \tag{4.1}$$

where $I_0 = I_1+I_2$, is a constant intensity, m is the modulation of the interference pattern, given by

$$m = \frac{2\sqrt{I_1 I_2}}{I_0}. \tag{4.2}$$

K is the grating vector, given by

$$\mathrm{K} = \frac{2\pi}{\Lambda}, \text{ and } \quad \Lambda = \frac{\lambda}{2\sin\theta}, \tag{4.3}$$

where Λ is the grating spacing, λ is the optical wavelength, and ϕ_0 is a constant phase shift arising from the difference between the phases of the two writing beams.

The crystal responds to the intensity distribution, via the photoconductivity property, by the excitation of pairs of electrons and ionised donors, their density being proportional to the intensity. These electrons are mobile and will diffuse from higher to lower electron density; the ionised donors are not mobile and consequently there is a violation of local charge neutrality and an electric field appears. The crystal is also electro-optic, (linear Pockels effect) meaning that an electric field will cause a small change in the relative dielectric constant and, therefore, a change in refractive index. The intensity interference pattern thus causes a dielectric grating with the same spacing, Λ. The spatial variations of these properties are shown in Fig. 4.2.

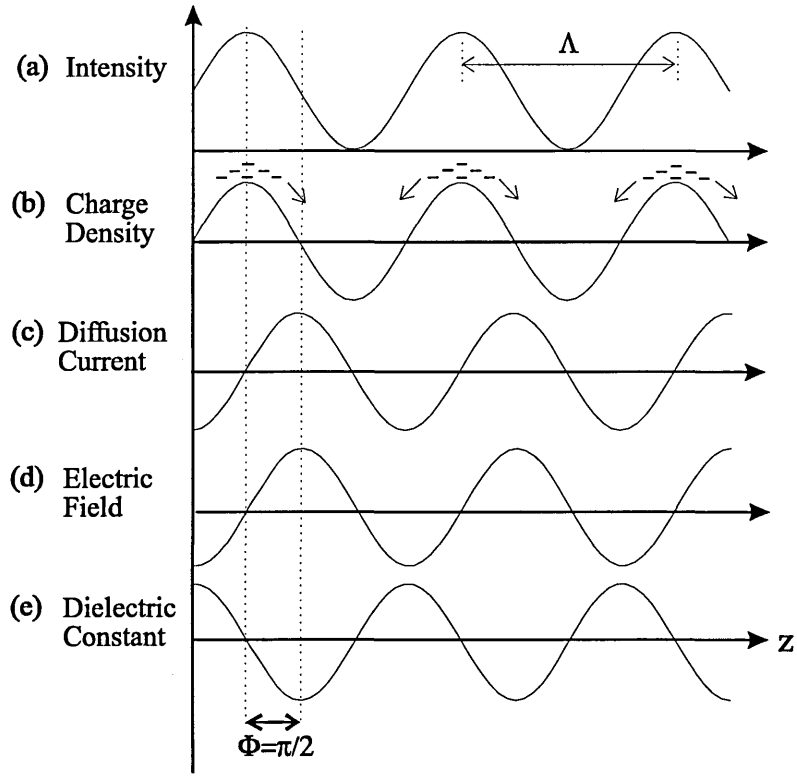

Fig. 4.2 The response of the material to light: (a) interference pattern, (b) mobile charges migrate, and (c) give rise to a diffusion current, (d) the subsequent space charge distribution gives rise to a space charge field, which (e) modulates the dielectric constant.

The intensity variation (a) causes the charge density distribution in (b), the mobile electrons then diffuse (indicated by arrows) from areas of high to low electron density, and may recombine with ionised donors. This migration of electrons causes the diffusion current, (c) which is 90 degrees out of phase with the electron distribution since it is proportional to the gradient of the electron density. There is therefore an excess of ionised donors in areas of high electron promotion (high intensity), and a reduced level of donors in areas of low promotion, consequently the electric field appears, (d). This electric field then modulates the dielectric constant, (e) through the linear electro-optic effect.

The photorefractive effect is classified as nonlinear since light propagating through the material is affected by material properties which are in turn influenced by the passage of the light. Nonlinear optical effects can be described by the following equation which relates the polarisation of a medium, P to the optical electric field, E, (Boyd, 1992)

$$P = \varepsilon_0 \chi_e(E) E\,, \tag{4.4}$$

where

$$\chi_e(E) = \chi_e^{(1)} + \chi_e^{(2)} E + \chi_e^{(3)} E^2 + ... \tag{4.5}$$

is the electronic susceptibility, and ε_0 is the dielectric permittivity of a vacuum. One nonlinear optical effect which displays a light dependent refractive index is the Kerr effect, which involves the third order susceptibility tensor, $\chi^{(3)}$. The associated refractive index change scales with absolute intensity and large power densities ($MWcm^{-2}$) are necessary to produce observable results. The change of refractive index in the photorefractive effect is, by contrast, due to the non-zero second order susceptibility tensor $\chi^{(2)}$ which is presented in crystalline media lacking inversion symmetry, such as BSO. The space charge field changes associated with the photorefractive effect rely on the modulation of the writing intensities, and light of very low intensity ($mWcm^{-2}$) may still produce observable refractive index variations.

4.2 Energy transfer Between Writing Beams in BSO

Consider two waves propagating in a photorefractive material in which they create a periodic refractive index modulation, a phase grating. Each wave is then diffracted by the grating and, for an unshifted grating, the diffracted wave has a $-\pi/2$ phase shift with respect to the original wave. If the grating is $\pi/2$ phase shifted, there will be an additional $\pm\pi/2$ phase shift with respect to the diffracted waves. Thus an in phase

superposition of waves occurs in one propagation direction, and an anti phase superposition of waves occurs in another propagation direction.

Suppose two waves a_1 and a_2 are described as:

$$\begin{aligned} a_1 &= R(z)\exp(-i\vec{\rho}\cdot\vec{r}) \\ a_2 &= S(z)\exp(-i\vec{\sigma}\cdot\vec{r}) \end{aligned} \tag{4.6}$$

where $R(z) = |R(z)|\exp[-i\varphi_1(z)]$ and $S(z) = |S(z)|\exp[-i\varphi_2(z)]$ where $\varphi_1(z)$ and $\varphi_2(z)$ are the phase angles of the complex amplitude. The interference of these waves forms a dynamic refractive index grating. If the dynamic grating is Φ phase shifted with respect to the interference pattern, the refractive index modulation will be described as (Guenter, 1989):

$$n = n_0 + \frac{\Delta n_s}{I_0}\left\{\exp(-i\Phi)R(z)S^*(z)\exp[-i(\vec{\rho}-\vec{\sigma})\cdot\vec{r}] + cc\right\} \tag{4.7}$$

where Δn_s is the saturation value of the photo-induced refractive index modulation. By taking the phase shift into account, the coupled wave equations can be expressed as:

$$\cos(\vartheta_0)\frac{dR}{dz} + \frac{\alpha}{2}R = -i\exp(-i\Phi)\frac{2\pi\Delta n_s}{\lambda_0}\frac{RS^*S}{I_0} \tag{4.8}$$

$$\cos(\vartheta_0)\frac{dS}{dz} + \frac{\alpha}{2}S = -i\exp(-i\Phi)\frac{2\pi\Delta n_s}{\lambda_0}\frac{SR^*R}{I_0} \tag{4.9}$$

The two waves are coupled in both the intensity and the phase according to the grating phase shift angle. By differentiating S and R, substituting them into Eqs. (4.8) and (4.9), separating the real and the imaginary parts, we obtain the differential equations for

coupled intensities (the real part) and coupled phases (the imaginary parts). The coupled intensity equations have the form (Guenter, 1989):

$$\frac{dI_R}{dz}+\frac{\alpha}{\cos(\vartheta_0)}I_R=-\Gamma\frac{I_R I_S}{I_R+I_S} \tag{4.10}$$

$$\frac{dI_S}{dz}+\frac{\alpha}{\cos(\vartheta_0)}I_S=\Gamma\frac{I_R I_S}{I_R+I_S} \tag{4.11}$$

where

$$\Gamma=\frac{4\pi\Delta n_S \sin(\Phi)}{\lambda_0 \cos(\vartheta_0)} \tag{4.12}$$

is the intensity coupling constant. The solution of Eq. (4.11) is giving by:

$$I_S(z)=I_S(0)\frac{I_R(0)+I_S(0)}{I_R(0)+I_S(0)\exp(\Gamma z)}\exp\left\{\left[\Gamma-\frac{\alpha}{\cos(\vartheta_0)}\right]z\right\} \tag{4.13}$$

If $I_S(0) << I_R(0)$, Eq. (4.13) can be simplified as:

$$I_S(z)=I_S(0)\exp\left\{\left[\Gamma-\frac{\alpha}{\cos(\vartheta_0)}\right]z\right\} \tag{4.14}$$

The signal wave is amplified with an exponential gain proportional to the intensity coupling constant Γ.

The energy transfer between writing beams in a dynamic holographic recording depends on the phase shift between the interference pattern and the grating formed. The "drift" mechanism of charge-carrier migrating (under an applied electric field) gives rise

to a very small phase shift when the drift length is much smaller than the grating spacing, for which stationary energy transfer is almost forbidden. The "diffusion" mechanism of charge-carrier migration (without an applied electric field) yields a $\pi/2$ phase shift grating for which stationary energy transfer occurs. However the index modulation by diffusion is low in the high spatial frequency domain, and so the intensity coupling constant Γ is small. Effective energy transfer can be achieved with a photorefractive crystal in the drift recording mode, which has a higher index modulation at high spatial frequency, and using the moving grating technique which yields an additional $\pi/2$ phase shift between the grating and the interference patterns.

Although stationary energy transfer is almost forbidden in a grating formed by the drift mechanism of charge-carrier migration, transient energy transfer during the grating recording could occur. This effect is a consequence of the non stationary phase mismatch between the recorded grating and the interference fringes when the two writing beams are of different intensities.

The coupled phase equation deduced from Eqs. (4. 8) and (4. 9) has the form (Heaton, 1985):

$$\frac{d\varphi}{dz} = \gamma \frac{I_R - I_S}{I_R + I_S} \tag{4. 15}$$

where $\varphi(z) = \varphi_1(z) - \varphi_2(z)$ is the phase difference between the interacting waves and γ is zero. In this case $d\varphi/dz = 0$, but stationary energy transfer occurs. On the other hand, when the index grating is in phase with the interference fringes, γ is finite and Γ is zero. In this case there is no stationary energy transfer, but $d\varphi/dz \neq 0$ provided that the intensities of the writing beams are different, which causes transient energy transfer.

Suppose two writing beams are incident on the medium with same incident angle ϑ_0. At $t = 0$ there is no grating at the surface of the nonlinear media, i.e. $\partial\varphi/\partial z = 0$. In the

stationary case $\partial\varphi/\partial z \neq 0$, according to Eq. (4. 15), and the surfaces of equal phase in the interference pattern are inclined relative to their original position. The equal phase contours of the refractive index grating are coincident with the inclined interference fringes because there is a zero phase shift between them in the charge-carrier drifting mode of recording. Assume that the recording medium has a finite time response and that the response time is τ. During $0 < t < \tau$, the time mismatch between the writing and the diffraction processes leads to a spatial mismatch between the interference pattern and the recorded refractive index grating. Transient energy transfer occurs. When $t >> \tau$ the refractive index grating succeeds in catching up with the inclined stationary interference distribution and the transient energy transfer ceases. It is clear that the following conditions should be satisfied for transient energy transfer: first, the recording medium has a finite response time, second, the intensities of the writing beams are different at the surface of incidence.

The analytical expression for the transient energy is given by (Kukhtarev, 1977):

$$I_{\pm}(z) - I_{\pm}(0) = \pm(\pi z\Delta)^2 [I_{-}(0) - I_{+}(0)] I_{+}(0) I_{-}(0) \exp\left(\frac{-t}{\tau}\right)\left[\frac{t}{\tau} + \exp\left(\frac{-t}{\tau}\right) - 1\right] \qquad (4.16)$$

where Δ is determined by the ensemble of characteristic parameters of the medium that defines the photorefractive process. It can be seen that the non stationary increment of the light intensity is proportional to the square of the thickness z and the response time of the medium τ.

4.3 Diffraction from Volume Refractive Index Gratings

4.3.1 Bragg Diffraction from a Volume Grating

A plane grating can be regarded as a set of periodically spaced transparent slits in an opaque screen. When a plane wave encounters these slits, it is scattered into different directions. Diffraction maxima occur when the scattered components from these slits are in-phase, which allows a constructive addition of these components. Fig. 4.3 shows the geometry for diffraction from a plane grating. Suppose that grating spacing is Λ, the refractive index everywhere is n_0, the wavelength of the incident wave is λ_0 in air, and the incident angle and diffracted angle of the plane wave are ϑ_0, and ϑ_L, respectively. The in-phase scattering takes place when the addition of the optical path lengths AB and AC is a whole number of wavelengths, which yields:

$$Sin(\vartheta_0) + Sin(\vartheta_L) = \frac{L\lambda_0}{n_0\Lambda} \tag{4.17}$$

where L is a integer. Eq. (4.17) shows that the incident angle has no specific restriction, and for a certain incident angle, a set of diffraction maxima with different angles can exist.

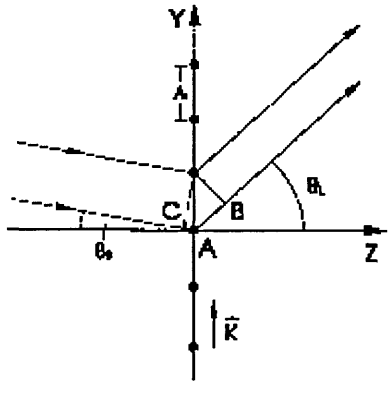

Fig. 4.3 Diffraction from a plane grating.

For a volume grating, Eq. (4.17) must still be valid. In addition, we must consider the scattering from all points along the same fringe. Fig. 4.4 shows that it is a slanted grating with a slant angle ϕ. The in-phase addition of the scattered components from a single occurs when the optical path lengths EF and GH in Fig. 4.4 are equal. This yields a condition:

$$\cos(\vartheta_L - \phi) = \cos(\vartheta_L + \phi) \tag{4.18}$$

which additionally restricts the diffraction angles to:

$$\vartheta_L = -\vartheta_0 \quad \text{or} \quad \vartheta_L = \vartheta_0 + 2\phi \tag{4.19}$$

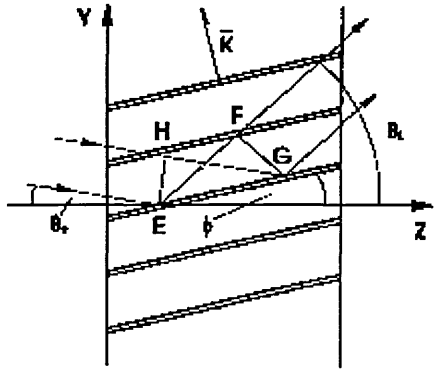

Fig. 4.4 Diffraction from a volume grating

For the condition of $\vartheta_L = -\vartheta_0$, the solution to Eq. (4.17) is $L = 0$, and only zero-order diffraction is allowed. For the condition of $\vartheta_L = \vartheta_0 + 2\phi$, Eq. (4.17) is

$$2Sin(\vartheta_0+\phi) = \frac{L\lambda_0}{n_0\Lambda} \tag{4.20}$$

This implies that other diffraction orders can exist at certain specific incident angles, namely the "Bragg" angles. With light incident at the Lth Bragg angle, up to two waves are permitted. These are the zeroth and Lth diffraction orders. With other incident angles, the wave travels through the grating without diffraction. The first diffraction order is allowed when light is incident at the first angle:

$$2Sin(\vartheta_0 + \phi) = \frac{\lambda_0}{n_0 \Lambda} \tag{4.21}$$

which is the Bragg condition and the incident light is said to be "Bragg-matched" to the grating.

4.3.2 Diffraction Efficiency for a Transmission Grating

In this subsection, the diffraction efficiency of volume gratings in the Bragg regime is analyzed by using coupled wave theory (Kogelnik, 1969). We consider here the diffraction efficiency of a slantless transmission grating under the Bragg condition.

Suppose the refractive index variation of a fixed grating is described by:

$$n = n_0 + \frac{\Delta n}{2}\left[\exp(-i\vec{K}\cdot\vec{r}) + cc\right] \tag{4.22}$$

where $\vec{r}$ is the position vector. The incident wave a_i and the diffracted wave a_d can be described by:

$$a_i = R(z)\exp(-i\vec{\rho}\cdot\vec{r}) \tag{4.23}$$

$$a_d = S(z)\exp(-i\vec{\sigma}\cdot\vec{r}) \tag{4.24}$$

where R(z) and S(z) are the complex amplitude, and $\vec{\rho}$ and $\vec{\sigma}$ are the wave vectors. The coherent sum must satisfy the scalar wave equation:

$$\nabla^2(a_i + a_d) + k^2(a_i + a_d) = 0 \tag{4.25}$$

where k is the propagation constant related to relative dielectric constant and the conductivity of the medium. Substituting Eqs. (4.23) and (4.24) into Eq. (4.25), the coupled wave equations can be obtained. Under the conditions of Bragg matching and assuming a slowly varying approximation for the complex amplitudes, the coupled wave equations take the form:

$$\cos(\vartheta_0)\frac{dR}{dz} + \frac{\alpha}{2}R = -i\chi S \tag{4.26}$$

$$\cos(\vartheta_0)\frac{dS}{dz} + \frac{\alpha}{2}S = -i\chi R \tag{4.27}$$

where α is the average intensity absorption coefficient, and

$$\chi = \frac{\pi\Delta n}{\lambda_0} \tag{4.28}$$

is the coupling constant. The coupled equations (4.26) and (4.27) have the typical solution:

$$R(z) = R_1 \exp(\gamma_1 z) + R_2 \exp(r_2 z) \tag{4.29}$$

$$S(z) = S_1 \exp(\gamma_1 z) + S_2 \exp(r_2 z) \tag{4.30}$$

where

$$\gamma_{1,2} = -\frac{\alpha}{2\cos(\vartheta_0)} \pm \frac{i\chi}{\cos(\vartheta_0)} \tag{4.31}$$

Adopting the following boundary conditions:

$$R(0) = R_1 + R_2 = 1 \tag{4.32}$$

$$S(0) = S_1 + S_2 = 0 \tag{4.33}$$

$$\frac{dS(0)}{dz} = \gamma_1 S_1 + \gamma_2 S_2 \tag{4.34}$$

The diffracted wave at the output of the volume grating can be obtained from Eq. (4.30):

$$\begin{aligned} S(T) &= -i\exp\left[\frac{-\alpha T}{2\cos(\vartheta_0)}\right]\sin\left[\frac{\pi\Delta n T}{\lambda_0\cos(\vartheta_0)}\right] \\ &\approx \frac{-i\pi\Delta n T}{\lambda_0\cos(\vartheta_0)}\exp\left[\frac{-\alpha T}{2\cos(\vartheta_0)}\right] \end{aligned} \tag{4.35}$$

where T is the thickness of the volume grating. The last expression in Eq. (4.35) is valid for small fringe modulations. Considering a volume grating formed in BSO with the crystal orientation set for maximum refractive index modulation, the complex amplitude of the diffracted wave can be obtained:

$$S(T) = \frac{-i\pi n_0^3 \gamma_{41} T E_{sc}}{\lambda_0\cos(\vartheta_0)}\exp\left(\frac{-\alpha T}{2\cos(\vartheta_0)}\right) \tag{4.36}$$

If the space-charge field has no additional phase shift, the diffracted wave will be $-\pi/2$ phase shifted with respect to the incident beam. The diffraction efficiency of the transmission volume grating is given by:

$$\eta = \frac{|S(T)|}{|R(0)|} = \left[\frac{\pi n_0^3 \gamma_{14} T}{\lambda_0\cos(\vartheta_0)}\right]|E_{sc}|^2\exp\left[\frac{-\alpha T}{\cos(\vartheta_0)}\right] \tag{4.37}$$

It can be seen that the diffraction efficiency is proportional to the square of the modulus of the space charge field. As the space-charge field is proportional to the fringe

modulation, the diffraction efficiency is proportional to the square of the fringe modulation.

4.4 Edge-enhancement with Moving Gratings inside the BSO Crystal

The technique of moving gratings in photorefractive crystals has been widely investigated since 1980. In the initial stages, researchers were interested in energy transfer in two-wave mixing and four-wave mixing configurations by moving gratings for signal amplification. In this case, the fringe modulation is very small and the differential equations can be solved with first-order approximations. Recently researchers have concentrated on the improvement of holographic recording by moving gratings, with numerical simulations and experimental investigations as well. For holographic applications, the fringe modulation is normally large and the space-charge field exhibits strong nonlinearity. The nonlinearity is revealed in two aspects: first, the optimum fringe velocity is nonlinearly dependent on the fringe modulation and the total intensity of the writing beams; second, the enhancement of the diffraction efficiency is nonlinearly dependent on the fringe modulation. For linear recording, these are drawbacks, and Fresnel holography could be preferred to eliminate the nonlinear effects. However these aspects can be explored in specific image processing and optical pattern recognition tasks. The dependence of the optimum fringe velocity on fringe modulation suggests a possibility of enhancing certain spatial frequencies of the Fourier spectrum of an object and suppressing other spatial frequencies. If we set the fringe velocity to a value suitable for higher fringe modulations, which are related to the higher Fourier spectrum components in a Fourier transform holographic recording, an edge-enhanced reconstruction will be obtained.

Edge-enhancement is a popular image processing technique and is very useful in optical pattern recognition. The edges of objects correspond to the high spatial frequencies of the Fourier spectrum, which in turn make the main contribution to the auto-correlation peak, other parts of the object correspond to low spatial frequencies, which make a smaller contribution to the auto-correlation peak. Therefore edge

enhancement can make the auto-correlation peak much sharper and so improve the discrimination. The edge enhancement of an input image can be achieved either by computer processing or by optical filtering techniques (Wang, 1990). With a computer-aided system, the high-speed processing advantage of the optical system is restricted by the computer. With a holographic derivative filter technique the total light efficiency of the system is low. Coherent and incoherent edge enhancement using BSO has also been previously reported and applied to optical correlation using two-wave mixing and four-wave mixing architectures (Huignard, 1978). By reversing the conventional object-to-reference beam ratio during holographic recording (i.e. making the object beam intensity much greater than the reference beam intensity), an edge-enhanced image can be obtained. It has been shown that this edge enhancement technique is successful and has the advantages of real-time and what can be termed active processing i.e. enhancing the diffraction from edges of the input.

In this section we demonstrate the edge enhancement of an object by moving gratings in a BSO crystal. It is a real-time and active processing, enhancing the diffraction from the edges and suppressing the diffraction from the dc component. As the edge enhancement is obtained, with selection of a certain band of the Fourier spectrum of the object to be enhanced, the signal-to-noise ratio and the stability of the output image is also improved due to the resonant effects of moving gratings. Experimental results of object edge-enhancement and edge-enhanced optical correlation are presented (The work was conducted in cooperation with Prof. Zhaoqi Wang, the external supervisor of the student).

4.4.1 Experimental arrangement

Fig. 4.5 shows the experimental arrangement used. The argon ion laser was operated at $\lambda = 514.5$ nm, and the beam was expanded and collimated to 20 mm in diameter by BE1. The polarizing beam splitter (PBS1) was used to divide the argon laser beam into two beams, one beam acts as a reference beam and another acts as an input beam. The beam ratio can be adjusted by rotating the first half-wave plate HWP1, and the

polarization direction of the reflected beam is kept parallel to that of the transmitted beam by rotating the second half-wave plate HWP2. A piezomirror PM was used to obtain a frequency detuning of the reference beam, and the scanning direction can be selected using either a sawtooth signal or an inverse sawtooth signal. In the read-out part, He-Ne

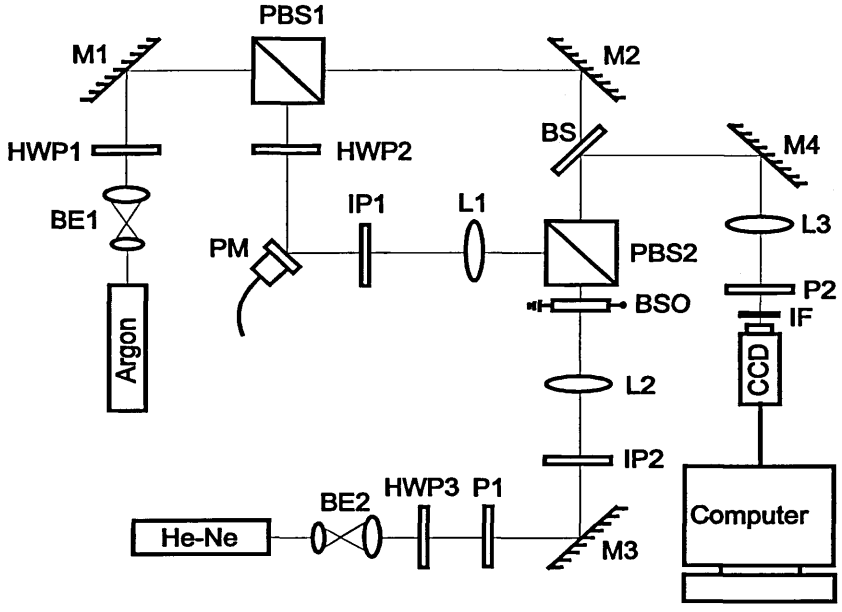

Fig. 4.5 The experimental arrangement for the edge enhanced correlation by moving gratings.

laser light is expanded and collimated by BE2. The third half-wave plate in conjunction with a polarizer P1 varies the beam intensity. IP1 is the reference signal while IP2 is the target to be detected. L1 and L2 are the transform lenses, whose focal lengths are selected to match the wavelength variation of the He-Ne laser in the read-out part from that of the argon ion laser in the writing part. The reconstructed image is detected via a CCD camera positioned at the back focal plane of the transform lens L3. An interference filter IF and a polaroid P2 were used to suppress the background noise. M (1-4) are mirrors. The received images are captured by a micro-computer and then are processed using IDL software. For the measurements of the variation of the optimum fringe velocity with the fringe modulation, and the variation of the enhancement of the diffraction efficiency with fringe modulation at fixed fringe velocity, a detector is put in

place of the CCD camera, and IP1, IP2, L1, and L2 are removed. An oscilloscope is used to monitor the detector output in this case.

4.4.2. Experimental results

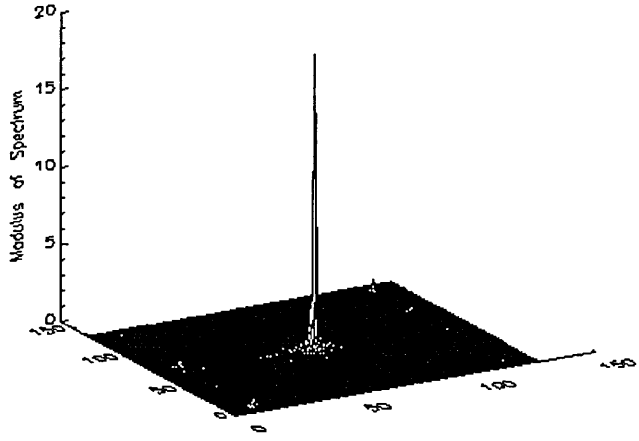

(a)

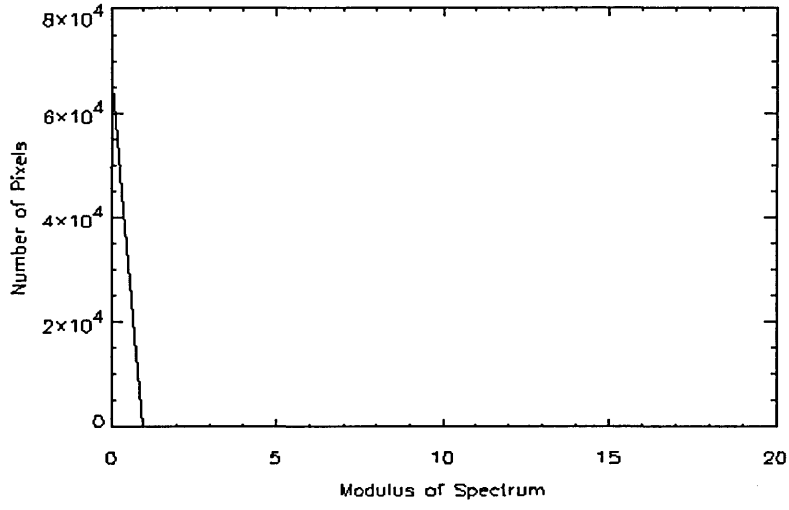

(b)

Fig. 4.6 The three dimensional surface (a) and the histogram (b) of the modulus of the Fourier power spectrum of the English letter "O".

A. The variation of the optimum fringe velocity with the Fourier power spectrum

It is well known that the Fourier power spectrum of an object is extremely non-uniform. For most of the images the maximum Fourier power spectrum component is the dc peak, and the spectrum drops by several orders of magnitude at high spatial frequencies. This causes a non-uniform distribution of the fringe modulation as well as non-uniform distribution of the total intensity of the writing beams in holographic recording. Fig. 4.6 presents the three dimensional surface plot and the histogram of the modulus of the Fourier power spectrum of a English letter "O" which we used for the following demonstrations. It can be seen that the peak of the power spectrum is around the zero frequency band which occupies only a few pixels. In the region of high spatial frequencies, the modulus of the Fourier spectrum is less than one-twentieth that of the zero frequency spectrum. Suppose the intensity of the reference beam is set to be the same of the intensity as the power spectrum of low spatial frequencies in a holographic recording set-up. The fringe modulation, which is described by

$$m(\alpha,\beta)=\frac{2|O(\alpha,\beta)||R(\alpha,\beta)|}{|O(\alpha,\beta)|^2+|R(\alpha,\beta)|^2} \tag{4.38}$$

where $O(\alpha,\beta)$ and $R(\alpha,\beta)$ are the object and the reference beams respectively, will vary from unity at zero spatial frequency to vary small (less than 0.01) at high spatial frequencies. Fig. 4.7 presents a histogram of the fringe modulation corresponding to fig. 4.6. It can be seen that the number of pixels falls linearly as the fringe modulation increases. For example, there are 4.6×10^4 pixels at a fringe modulation of 0.3, but only 1.3×10^4 at a fringe modulation of 0.8.

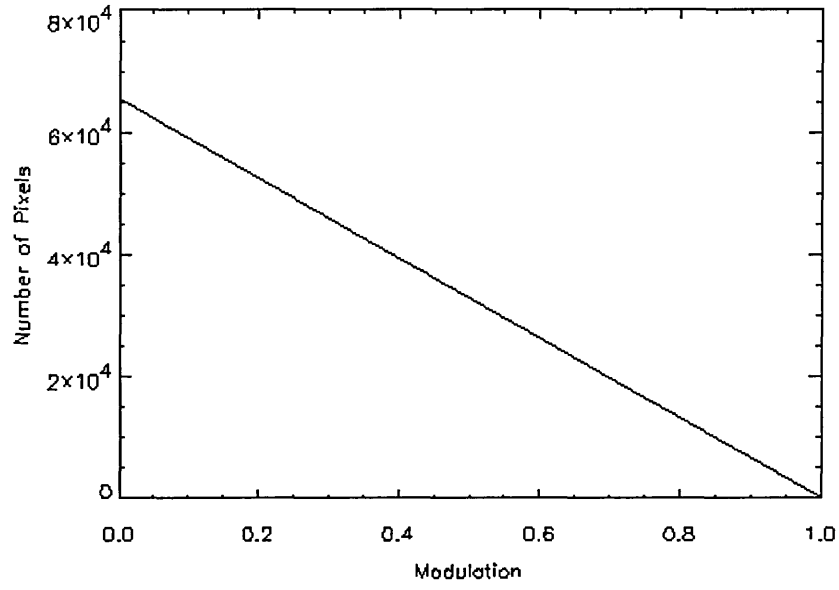

Fig. 4.7 Histogram of the fringe modulation of the Fourier transform hologram of the English letter "O".

The optimum fringe velocity for moving gratings is strongly dependent on the fringe modulation(Wang, 1994). Fig. 4.8 presents the experimental results. The grating recording conditions are as follows: fringe spacing $\Lambda = 20\ \mu$m, applied voltage $E_0 = 6.25$ kV/cm, intensity of the reference beam $|R(\alpha,\beta)|^2 = 7.5$ mW/cm^2. In this experiment the intensity of the reference beam is kept constant to simulate the actual conditions in holographic recordings. The piezomirror is driven by a controller connected to a sawtooth wave form generator. The scanning velocity can be adjusted either by changing the peak amplitude of the sawtooth voltage or by changing the scanning period. The fringe velocity of the moving gratings caused by the scanning piezomirror is determined by the relationship:

$$v = \frac{2\kappa U_M \Lambda \cos[\vartheta_0]}{\lambda t} \tag{4.39}$$

where U_M is the peak amplitude of the sawtooth voltage applied to the piezomirror, κ is the elongation of the stack of the piezo for unity voltage, ϑ_0 is the incident angle of the beam to the piezomirror, λ is the wavelength of the writing beam and t is the scanning period of the sawtooth voltage. In these experiments, we constructed a Mach- Zehnder interferometer, keeping the same laser wavelength and the same incident angle of the beam to the piezomirror as that in the holographic recording system, for calibrating the fringe velocity. The fringe velocity is now determined by:

$$v = \frac{N\Lambda}{t} \tag{4.40}$$

where N is the fringe number passing through a fixed position in the output of the interferometer for one scanning period of the sawtooth voltage. The diffracted helium-neon laser is incident on a detector, which is connected to a digital oscilloscope to monitor the variation of the diffraction with the fringe velocity.

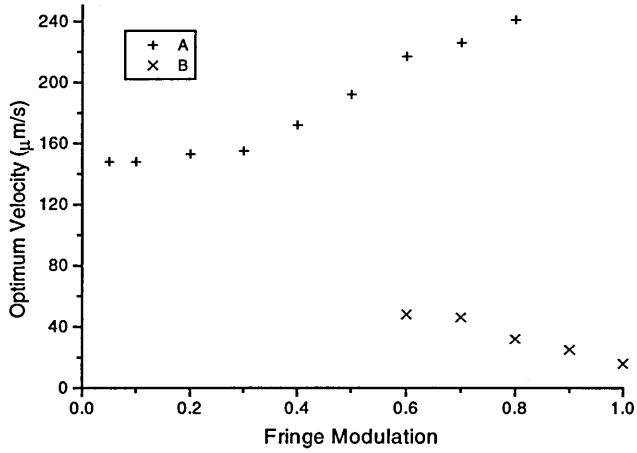

Fig. 4.8 The experimental results for the optimum fringe velocity versus the fringe modulation. $\Lambda = 20\ \mu m$, $E_0 = 6.25$ kV/cm, $|R(\alpha,\beta)|^2 = 7.5 mW/cm^2$.

We can see from fig. 4.8 that there are two sets of data, "A" and "B". Set "A" is at high fringe velocity which starts from very small fringe modulation and continues to a fringe modulation of 0.8. Set "B" is at low fringe velocity which starts from a fringe

modulation of 0.6 up to unity. This is due to the fact that there are two specific fringe velocities which yield peaks in the diffraction efficiency in the range of fringe modulation 0.6 to 0.8. One is at a higher velocity which can be regarded as a higher shift of the optimum velocity at small fringe modulations, and another is at a much lower fringe velocity. At a fringe modulation of 0.6, the peak for a low fringe velocity is much lower than that for a high fringe velocity. As the fringe modulation increases, the peak for a low fringe velocity increases and becomes more significant, and the peak for high fringe velocity decreases and becomes less important. At a fringe modulation of 0.9, the peak for a high fringe velocity almost disappears. We can see that the optimum fringe velocity is about 150 μm/s at small fringe modulations (less than 0.1), and it increases as the fringe modulation increases (set "A"). It reaches 240 μm/s at a fringe modulation 0.8. The sub-optimum fringe velocity (set "B") at the fringe modulation of 0.6 is 50 μm/s, and it decreases as the fringe modulation increases. For fringe modulations larger than 0.9, the optimum fringe velocity becomes very low, it equals to 14 μm/s at the fringe modulation of unity for instance, which can be regarded as a lower shift of the sub-optimum fringe velocity. We note that the optimum fringe velocity is nonlinearly dependent on the fringe modulation in the range in which we are interested. Fig. 4.9 shows the numerical results for the modulus of the space-charge field versus the relative fringe velocity (m = 0.6) (Brost, 1993). It is shown that, for high fringe modulations, there are two peaks for the space charge field. This could explain the two sets of data in fig.4.8.

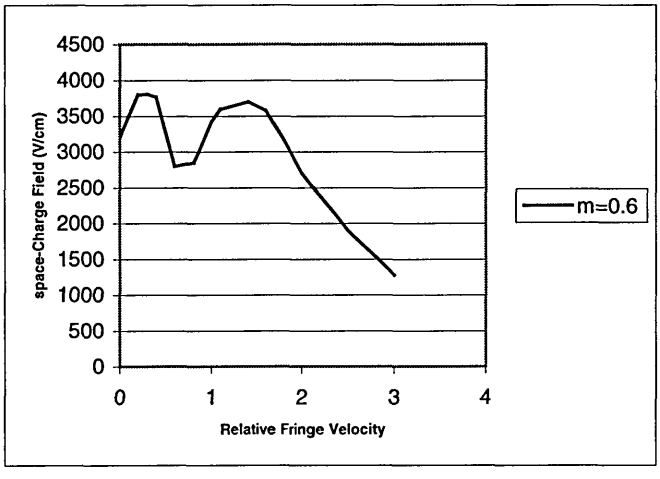

Fig. 4.9 The space-charge field versus the fringe velocity at m=0.6.

B. Enhancement of the diffraction efficiency at different fringe modulations by moving gratings with fixed fringe velocity

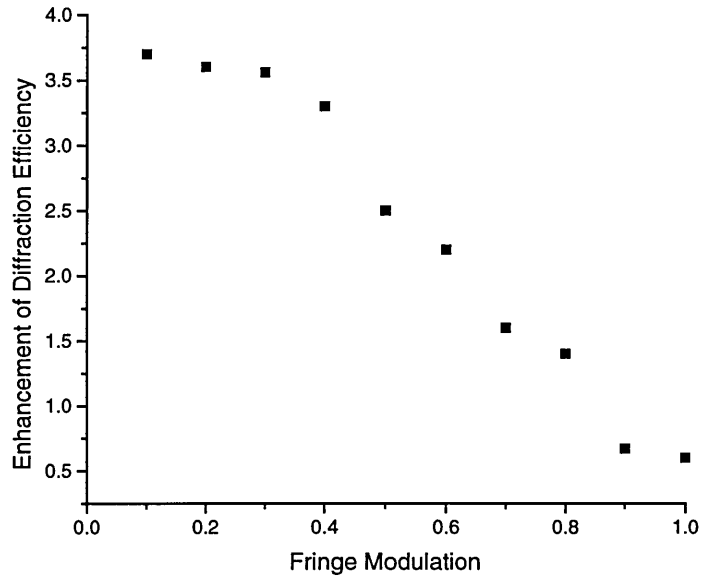

Fig. 4.10 The experimental results for the enhancement of the diffraction efficiency versus the fringe modulation with a fixed fringe velocity. $v = 150\,\mu m/s$, $\Lambda = 20\,\mu m$, $E_0 = 6.25$ kV/cm, $|R(\alpha,\beta)|^2 = 7.5 mW/cm^2$.

The nonlinear dependence of the optimum fringe velocity on the fringe modulation provides a non-uniform enhancement of the diffraction efficiency with moving gratings. With a fixed fringe velocity appropriate to smaller fringe modulations, the diffraction efficiency from the corresponding fringe modulations could be enhanced by several times while the diffraction efficiency from the higher fringe modulations could be suppressed significantly. Fig. 4.10 presents the results of the enhancement of the diffraction efficiency of different fringe modulations (different spatial frequencies) when the fringe velocity is appropriate to the smaller fringe modulations. The grating recording conditions are as before, except that the fringe velocity is fixed at 150 μm/s appropriate to the smaller fringe modulations. We can see from fig. 4.10 that the diffraction efficiency is enhanced by several times at smaller fringe modulations (3.2 times

enhancement at a fringe modulation of 0.4 and 3.7 times enhancement at a fringe modulation of 0.1 for instance), and it is suppressed at larger fringe modulations (reduced by a factor of 0.6 at a fringe modulation of unity for instance). Considering that the high fringe modulation figures correspond to the lower spatial frequencies of the Fourier spectrum and the low fringe modulation figures correspond to the higher spatial frequencies, the effect of moving gratings described in fig. 4.10 yields edge-enhancement of images, characterized by suppressing low spatial frequency components as well as enhancing the high spatial frequency components.

C. Edge enhancement of objects and edge enhanced correlation by moving gratings

In the following experiments, we chose the English letter "O", a binary rectangle and a binary aeroplane as the objects. The object is inserted at the input plane IP1, and the intensity ratio of the writing beams is adjusted for a linear recording. The total intensity of the writing beams is about 1.0 mW/cm^2. The average fringe spacing is 20 μm and the entire Fourier transform of the object was within the crystal dimensions. The recorded dynamic hologram is readout by the collimated helium-neon laser, and the output image is received by the CCD camera. The linear holographic reconstruction is shown in fig. 4.11. The (a), (b) and (c) in fig. 4.11 are the reconstruction of the English letter "O", the binary rectangle and the binary aeroplane, respectively. Then the moving grating is applied, and the fringe velocity is experimentally chosen to be $25\mu m/s$. Fig. 4.12 shows the edge enhanced reconstruction by the moving gratings. The (a), (b) and (c) in fig. 4.12 correspond to the (a) (b) and (c) in fig. 4.11, respectively. It is evident that edge enhancement of the objects has occurred. We note that the effect of the edge enhancement is different for the three objects. The binary rectangle shows the best edge enhancement. This is because the simple shape consists of a larger magnitude of low frequency components, and the larger the low frequency component is, the better the edge enhancement of the object. To show the edge enhanced effects more clearly, horizontal cross-sections are also presented, as shown in fig. 4.13 and fig. 4.14 corresponding to fig. 4.11. (b), and fig. 4.12 (b), respectively. Fig. 4.13 corresponds to the linear reconstruction and fig. 4.14 corresponds to the edge enhanced reconstruction.

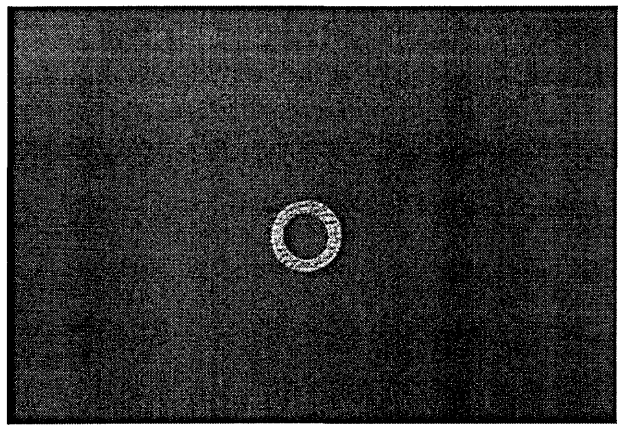

(a)

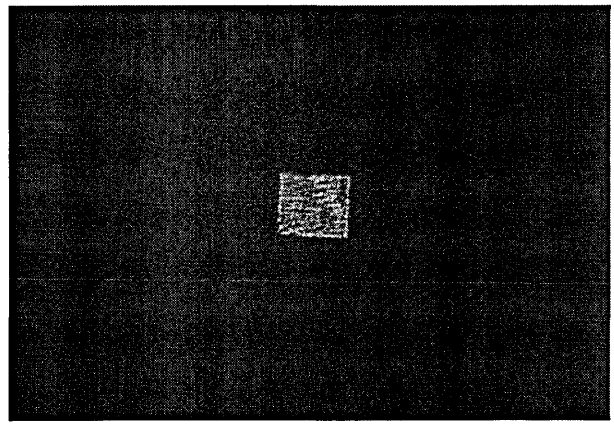

(b)

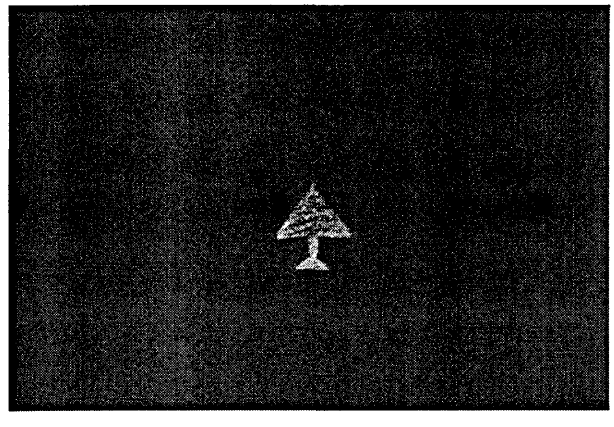

(c)

Fig. 4.11 The linear reconstruction of the Fourier transform holograms of three different objects: (a) the English letter "O"; (b) the binary rectangular object; (c) the binary aeroplane.

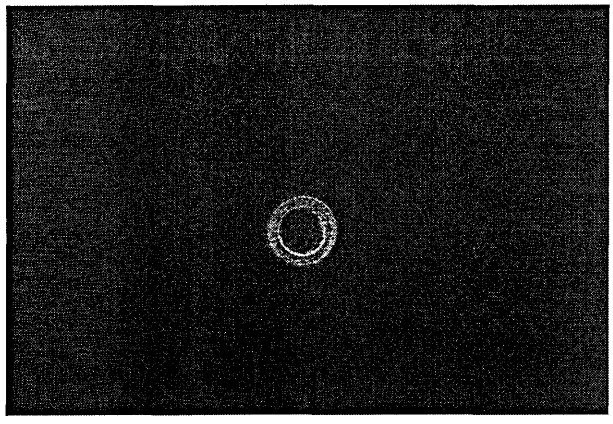

(a)

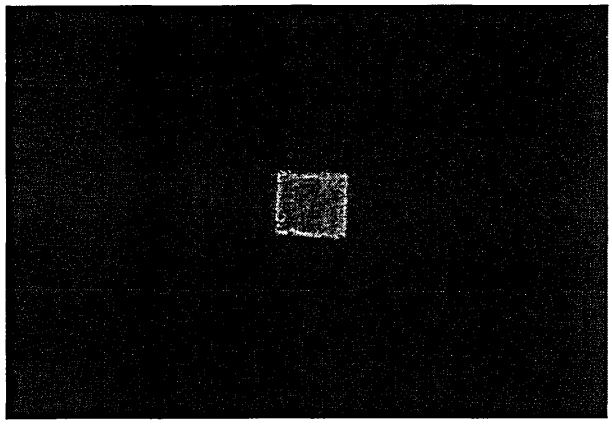

(b)

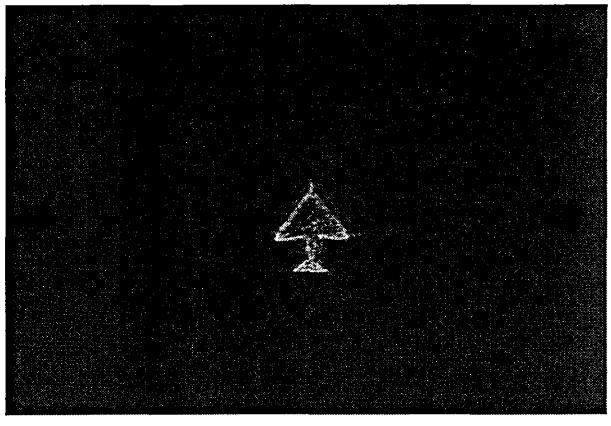

(c)

Fig. 4.12 The edge enhanced reconstruction of the Fourier transform holograms of the objects corresponding to Fig. 4.10 by moving gratings.
$\Lambda = 20\ \mu\text{m}$, $E_0 = 6.25$ kV/cm, $\left|R(\alpha,\beta)\right|^2 = 1.2\text{mW/cm}^2$.

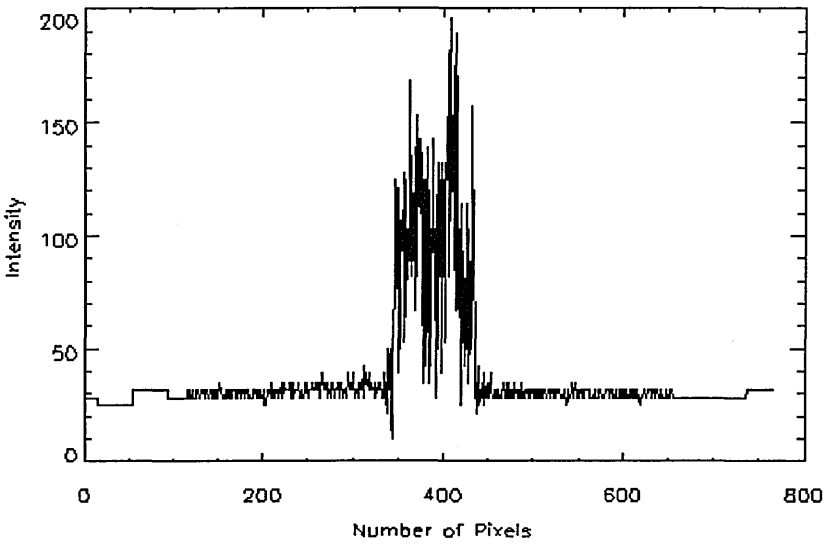

Fig. 4.13 The horizontal cross-section of the linear reconstruction of the rectangle, corresponding to fig. 4.10(b).

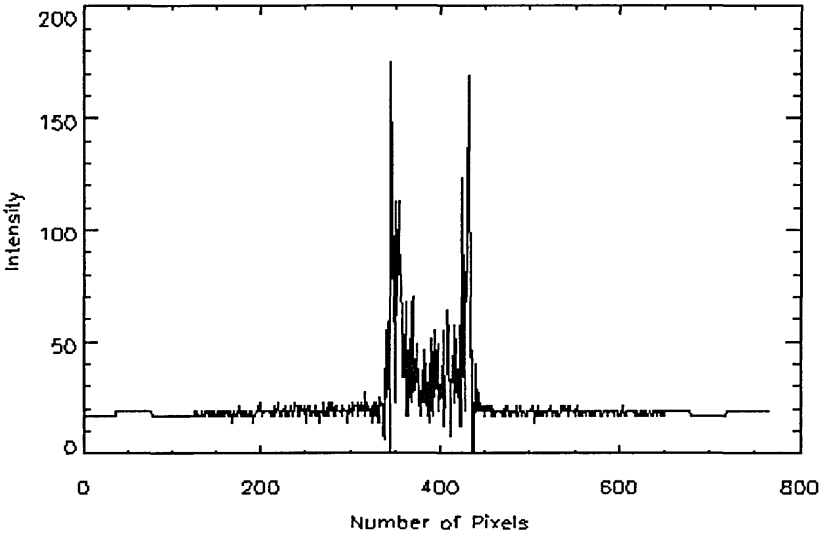

Fig. 4.14 The horizontal cross-section of the edge enhanced reconstruction of the rectangle by moving gratings, corresponding to fig. 4.11(b).

For purpose of investigating optical pattern recognition, the second object, which is the same as the object in the plane of IP1, is placed at the plane IP2 in the read out part of the optical correlation system. The optical correlation patterns were detected by the CCD camera. Fig.4.15 presents the auto-correlation results for the letter "O". Fig. 4.15(a) was obtained without moving gratings and fig. 4.15(b) was obtained with moving gratings. It can be seen that the correlation spot in 4.15(b) is much smaller than that in 4.15(a) showing the improvement of the sharpness of the auto-correlation when using moving gratings. 4.15(c) and (d) are 3D plots of 4.15 (a) and 4.15 (b) respectively.

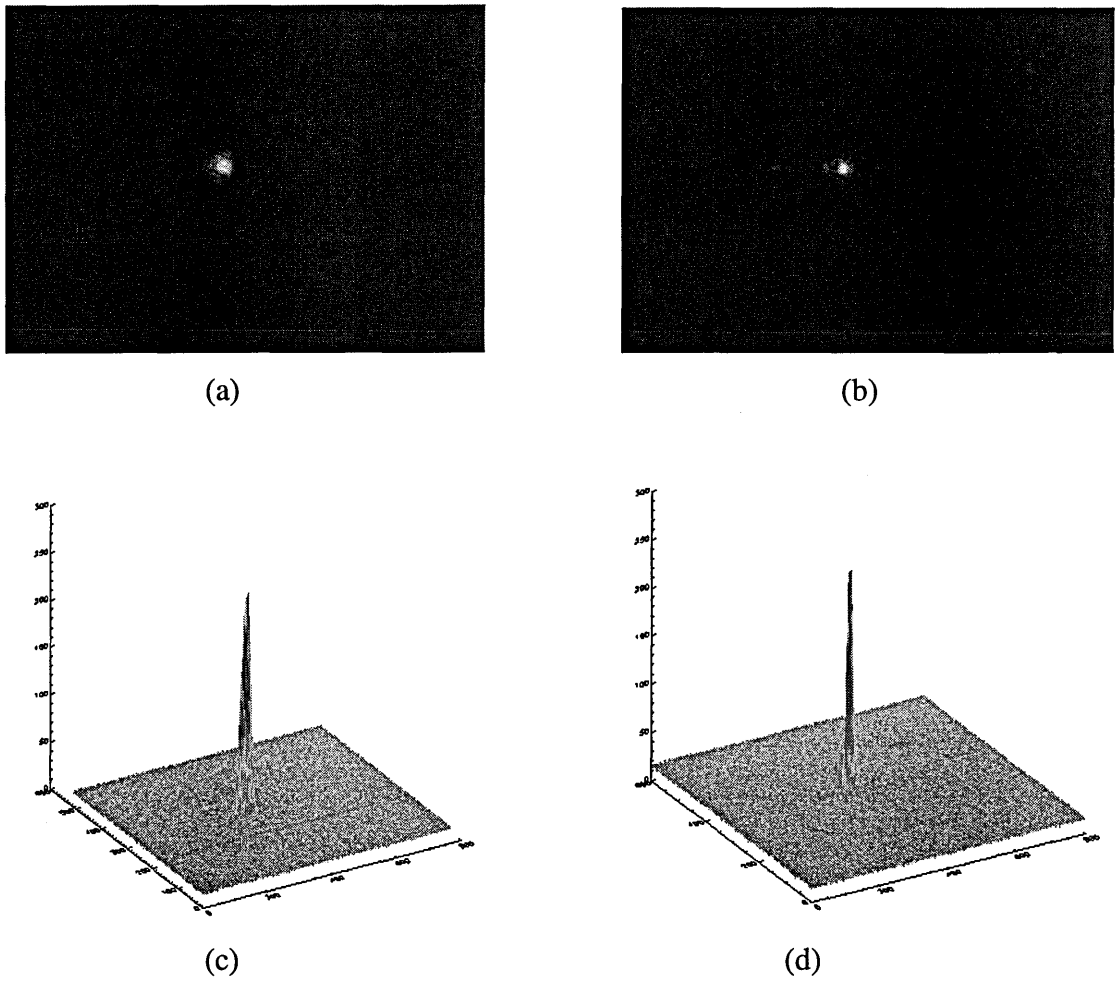

Fig. 4.15. The auto-correlation results of the letter "O". $\Lambda = 20\ \mu m$, $E_0 = 6.25$ kV/cm, $|R(\alpha,\beta)|^2 = 1.2$ mW/cm^2. (a) without moving gratings; (b) with moving gratings, (c) and (d) are their 3D plots.

We have experimentally shown the nonlinear dependence of the optimum fringe velocity on the fringe modulation and the variation of the enhancement of the diffraction efficiency with fringe modulation by moving gratings with a fixed fringe velocity suitable to high fringe modulations. There are two groups of data in the variation of the optimum fringe velocity with fringe modulation over a range of fringe modulations, and the velocity difference between these two groups is very large. We have achieved edge enhancement of objects and edge enhanced correlation by moving gratings. The experimental results are quite good, and the results (the fringe velocity adopted for instance), are coincident with previous work. We have improved the sharpness of the auto-correlation peak, by a factor of one-third, using the moving gratings. This is a significant improvement in the discrimination for optical pattern recognition. The proposed edge enhancement technique has the unique advantages of being able to arbitrarily select spatial frequencies to be enhanced, an improved signal-to-noise ratio and the elimination of fluctuations of the output due to the resonant effects of moving gratings. Therefore the proposed technique is attractive in respect to the use of photorefractive crystals. In our system we use a piezomirror to acquire Doppler frequency detuning. If an acousto-optic modulator were used instead, the driving system would be simpler thus making the system more compact.

Chapter 4: References

L.B. Au and L. Solymar, "Space-charge field in photorefractive materials at large modulation", Opt. Lett., **13** 660-662 (1988).

L.B. Au and L. Solymar, "Higher harmonic gratings in photorefractive materials at large modulation with moving fringes", J. Opt. Soc. Am., **A7** 1554-1561 (1990).

A.S. Awwal, M.A. Karim and S.R. Jahan, "Improved correlation discrimination using an amplitude-modulated phase-only filter, Appl. Opt., **29** 233-236 (1990).

R. W. Boyd, "Nonlinear Optics", San Diego, Academic Press, p120 (1992).

G.A. Brost, "Numerical analysis of the photorefractive response with moving gratings", Photorefractive Materials, Effects and Devices PRM'93, August 1993, Kiev, Ukraine, Post-deadline paper.

N.J. Cook, "Properties and processing applications of photorefractive BSO", PhD thesis (University of Abertay Dundee, Supervisor: Colin M. Cartwright), 1998.

J. Feinberg, "Real-time edge-enhancement using the photorefractive effect", Opt. Lett., **5** 330-332 (1980).

P. Guenter, "Electro-Optic and Photorefractive Materials", Part 4, Springer-Verlag, Berlin (1989).

G. Hamel de Monchenault, B. Loiseaux and J.P. Huignard, "Amplification of high bandwidth signals through two-wave mixing in photorefractive $Bi_{12}SiO_{20}$ crystals", Appl. Phys. Lett., **50** 1794-1796 (1987).

G. Hamel de Monchenault and J.P. Huignard, "Two-wave mixing with time modulated signal in $Bi_{12}SiO_{20}$ theory and application to homodyne wave front detection", J. Appl. Phys., **63** 624-627 (1988).

J.M. Heaton and L. Solymar, "Transient energy transfer during hologram formation in photorefractive crystals", Opt. Acta **32**, 397-408 (1985).

J.P. Huignard and J.P. Herriau, "Real-time coherent object edge reconstruction with $Bi_{12}SiO_{20}$ crystals", Appl. Opt., **17** 2671-2672 (1978).

J.P, Huignard and A. Marrakchi, "Coherent signal beam amplification in two-wave mixing experiments with photorefractive $Bi_{12}SiO_{20}$ crystals", Opt. Comm., **38**, 249-154 (1981).

N.V. Kukhtarev, V.B. Markov and S.G. Odulov, "Transient energy transfer during hologram formation in $LiNbO_3$ in external electric field", Opt. Comm. **23**,338-343 (1977).

H. Kogelnik, "Coupled wave theory for thick hologram gratings", Bell. Syst. Tech. J., **48**, 2909-2946 (1969).

J. Ma, J.E. Ford, Y. Taketomi and S.H. Lee, "Moving grating for enhanced holographic recording in cerium-doped SBN:60", Opt. Let., **16** 270-272 (1991).

S. Mallick, B. Imbert, H. Ducollet, J.P. Herriau and J.P. Huignard, "Generation of spatial subharmonics by two-wave mixing in a nonlinear photorefractive medium", J. Appl. Phys., **63** 5660-5663 (1988).

M.P. Petrov, S.I. Stepanov and A.V. Khomenko, "Photorefractive crystals in coherent optical systems", Chapter 6, Springer-Verlag, Berlin, 1991.

L. Pichon, and J.P. Huignard, "Dynamic joint-Fourier-transform correlator by Bragg diffraction in photorefractive $Bi_{12}SiO_{20}$ crystal", Opt. Comm., **36**, 277-280 (1981).

H. Rajbenbach, J.P. Huignard and B. Loiseaux, "Spatial frequency dependence of the energy transfer in two-wave mixing experiments with BSO crystals", Opt. Comm., **48** (1983) 247-252.

H. Rajbenbach, J.P. Huignard and Ph. Refregier, "Amplified phase-conjugate beam reflection by four-wave mixing with photorefractive $Bi_{12}SiO_{20}$ crystals", Opt. Lett., **9** 558-560 (1984).

Ph. Refregier, L. Solymar, H. Rajbenbach and J.P. Huignard, "Two-beam coupling in photorefrective $Bi_{12}SiO_{20}$ crystals with moving grating: theory and experiments", J. Appl. Phys., **58** 45-57 (1985).

L. Solymar and J. M. Heaton, "Transient energy transfer in photorefractive material; an analytic solution", Opt. Comm., **51**, 76-78 (1984).

N.A. Vainos and R.W. Eason, "Real time edge enhancement by active spatial filtering via five wave mixing in photorefractive BSO", Opt. Comm., **59** 167-172 (1986).

Z.Q. Wang, W.A. Gillespie, C.M. Cartwright and C. Soutar, "Real-time computer-aided multiplexed optical intensity correlator using Fresnel holographic filters and a liquid crystal television", Opt. Comm., **86** 19-24 (1991).

Z.Q. Wang, C. Soutar, W.A. Gillespie and C.M. Cartwright, "Real-time edge-enhanced object correlation using incoherent readout of photorefractive BSO", Optik, **93** 157-162 (1993).

Z.Q. Wang, W.A. Gillespie and C.M. Cartwright, "Holographic-recording improvement in a bismuth silicon oxide crystal by the moving-grating technique", Appl. Opt., **33** 7627-7633 (1994).

Z.Q. Wang, C.M. Cartwright, W.A. Gillespie and N.J. Cook, "Effects of optical bias on moving gratings in bismuth silicon oxide at large fringe modulation", Appl. Opt., **35** 3829-3834 (1996).

Chapter 5. Photorefractive Joint Transform Correlator

5.1 The Liquid Crystal Television (LCTV) used as a Spatial Light Modulator

The LCTV used as a spatial light modulator is the Epson liquid crystal video projector (model VP-100PS). The liquid crystal display is active-matrix addressed, with 326x264 (rows by columns) pixel elements, each pixel having a size of 80x90 μm and an active area of 55x60 μm . It has a sandwich-like structure, i.e. the polarizer, the liquid crystal cell and the analyzer. The original Epson liquid crystal display is arranged such that the polarization direction of the polarizer is parallel to the molecular director on the incident surface of the liquid crystal cell, and the polarization direction of the analyzer is parallel to that of the polarizer. The coupled amplitude and phase modulation mode can be available depending on the polarization of the light and the voltage applied to the liquid crystal cells.

Fig 5.1 shows the construction of a transmissive type, twisted nematic liquid crystal cell. The twisted nematic liquid crystal is an anisotropic medium that can be treated locally as a homogeneous uniaxial crystal whose optical axis is parallel to the direction of the molecules. Because of the twist induced by scratches on the surface of the sandwiching electrodes, the molecules gradually rotate in a helical fashion, usually through 90°. Thus the material is inhomogeneous, and the optical axis follows the molecular twist. With no voltage applied across the liquid crystal layer, the incident polarized light, as it transverses the liquid crystal layer, is gradually twisted in its polarization direction by the liquid crystal molecules with the twisted nematic effect. When the light reaches the back of the cell, the polarization direction is rotated by 90° and becomes perpendicular to that of the analyzer, and the light is blocked. This is the fully "off" condition of the liquid crystal cell.

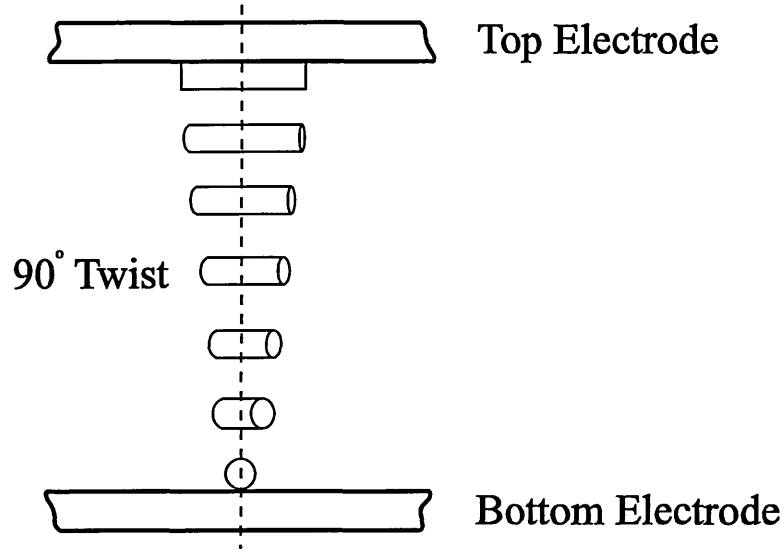

Fig. 5.1 Molecular director orientation in a twisted nematic liquid crystal cell.

When an electric field is applied, the molecules away from the surfaces tend to realign in a direction approximately parallel to the applied field and normal to the surface. This realignment causes changes in the transmission of polarized light and the liquid crystal acts as a birefringent medium whose characteristics depend on the applied voltage. The twisted nematic effect of the liquid crystal molecules becomes weaker, and the polarization direction of the light emerging from the liquid crystal cell will not be fully perpendicular to that of the analyzer. This is "on" condition of the liquid cell.

The voltage applied to the LCTV cells consists of two parts. First a bias voltage across every cell produces the transmittance and can be largely controlled by adjustment of the 'brightness' level on the video projector. Additional control is provided by the 'contrast' level which modifies the contrast ratio between a fully 'on' and a fully 'off' pixel. The 'brightness' and 'contrast' levels on the video projector can be adjusted according to a hardware fixed scale between 0 and 10. The second part of the voltage is applied individually to each pixel and controls the continuous 256 grey level mode. With a non-zero angle between the polarization direction of the polarizer and the molecular direction on the incident surface, a controlled birefringence effect is involved. Therefore, the

voltage-dependent intensity transmission of the twisted nematic liquid crystal cell can be obtained.

The response of the transmitted amplitude and phase change to applied field is coupled and complex and the LCTV must be characterized and determined the operating curve. Prior knowledge of this is essential to correct any filter algorithms accordingly. For coherent processing the coupled amplitude and phase modulation should be generally avoided. In this research all the filters are designed to amplitude modulate and a minimum phase change is therefore desired.

Phase mostly modulation can be achieved by using an appropriate applied voltage bias when the polarization of the light is oriented parallel to the LC molecule director. For this mode of operation, the directions of polariser and analyzer, which sandwich the LCTV, will be 0° and 90° respectively, where the direction of the LC molecular director at the front face of the LCTV is also 0°. Phase mostly modulation is achieved under a small bias voltage where the LC directors are slightly perturbed and their twist angle distribution is close to the unperturbed case where no bias is applied. In this configuration the LCTV produces phase-mostly modulation with small amplitude modulation.

Amplitude mostly modulation can be achieved for a bias voltage above a certain threshold level. The mode of operation is therefore partially determined by the "brightness" setting. The polariser should be at 90°, perpendicular to the molecular director at the front face and analyzer should be parallel to the polariser. With a large applied voltage the LC molecular directors are almost untwisted, and there is little or no phase variation. Fig. 5.2 (a) and (b) show the amplitude and phase modulation effect obtained from a Mach-Zehnder interferometer (Cook, 1998). The upper image shows the continuous interference fringes resulting from minimum phase modulation and the lower image shows discontinuous fringes resulting from a phase mismatch between the different grey levels.

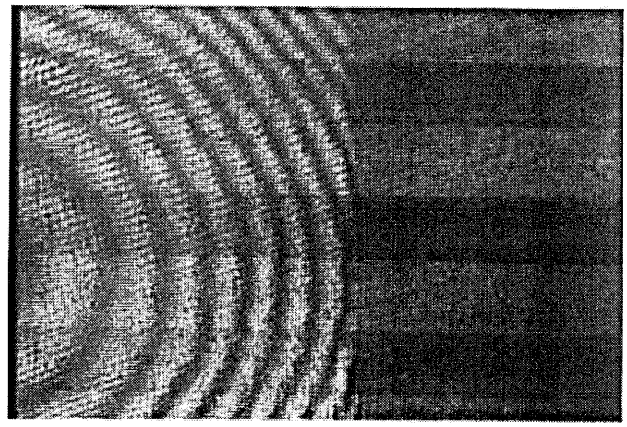

(a)

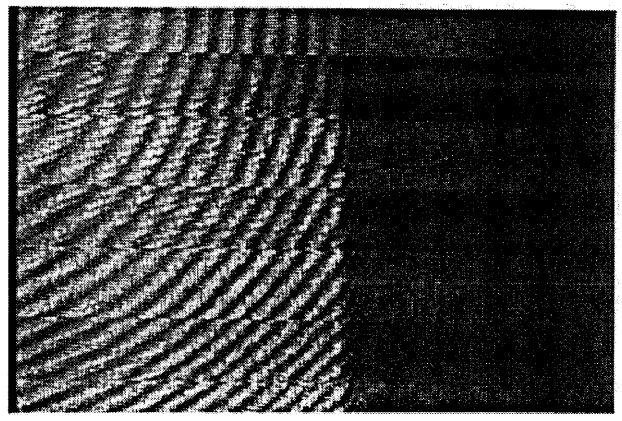

(b)

Fig. 5.2 Interference fringes showing amplitude (a) and phase (b) mostly operation of the LCTV.

Linear polarised light that enters an LCTV parallel to the molecular director will undergo a phase change of

$$\phi = \frac{2\pi n_e d}{\lambda} \tag{5.1}$$

and emerge linearly polarised, d is the thickness of the LC.

Light polarised perpendicular to the director will undergo a phase change of

$$\phi = \frac{2\pi n_0 d}{\lambda} \tag{5.2}$$

but will still emerge linearly polarised. n_o and n_e are the ordinary and extraordinary refractive indices of the birefringent LC, and n_e - n_o > 0, giving positive dielectric anisotropy.

To find the correct configuration, the orientation of the molecular directors at the front face of the LCTV must be determined as follows. Intensity nulls for an LCTV sandwiched between polariser and analyser with zero applied voltage, can only be achieved if the input polarisation is either parallel or perpendicular to the molecular director, (Kirsch, 1992). Light entering the front face polarised at any other angle will emerge elliptically polarised. The polarisation state of the exit light can therefore be used to determine two possible orientations of the molecular director at the front face.

5.2 The Architecture of a Photorefractive JTC

As discussed in Chapter 2, there are two main architectures of optical correlator: the VanderLugt correlator and the joint transform correlator. In this section, the experimental implementation of a photorefractive joint transform correlator is presented. Photorefractive recording materials give the advantage of real-time recording and read-out of the hologram, removing the need for development and thus avoiding the position constraints previously encountered by the VanderLugt correlator. The use of the spatial light modulator (SLM) to display the images offers the possibility of continuous update of the hologram, and the combination of photorefractive crystals and SLMs can be used to design real-time pattern recognition systems.

There are other advantages gained by using a photorefractive crystal as the JPS processor, rather than the single SLM setup, such as increased resolution in the Fourier plane. The fact that the magnitude of the photorefractive space charge field depends on

the modulation of the intensity, rather than its absolute value which is the case for linear detectors, can be used to implement Fourier plane nonlinearities. The degree of the nonlinearity may be adjusted by varying beam ratios. Khoury (Khoury, 1994) has reported a photorefractive correlator that operates by using two-beam coupling to implement nonlinearity in the Fourier plane, correlations similar to inverse filters and phase-only filters were obtained.

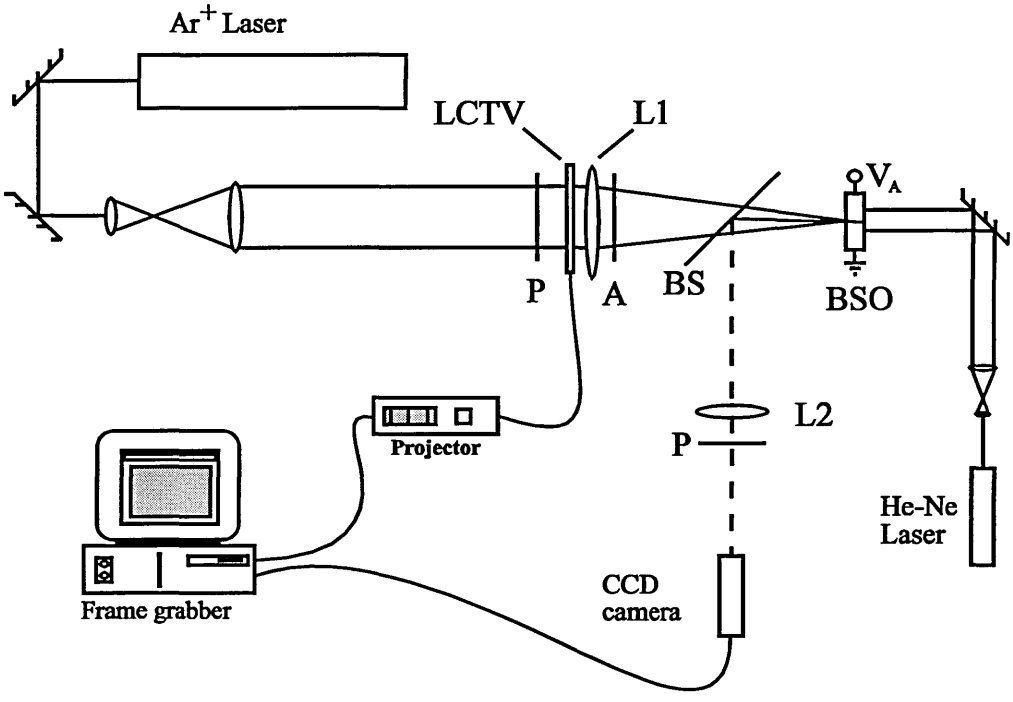

Fig 5.3 The photorefractive joint transform correlator.

Referring to Figs. 2.4 and 5.3, which show the classic and photorefractive JTCs respectively, and assuming that the two writing beams are of a suitable wavelength to enable hologram formation in the crystal, in these experiments the 514nm line from an argon-ion laser is used. In fig.5.2, the argon ion laser beam is expanded and collimated first. The beam intensity ratio can be adjusted by rotating a half-wave plate. L1 is the first Fourier transform lens. Input images of 768 x 512 pixels are generated by a frame grabber and scaled to ensure the correct registration of pixel on the LCTV. The angles of polariser (P) and analyzer (A) are chosen to operate LCTV in amplitude-mostly

modulation. The distance between the reference and target ensures that the cross-correlation signal is adequately separated from the dc part. The Fourier transform is formed at the BSO crystal or other photorefractive crystals, which is positioned at the back focal plane of the lens L1. For the read-out part, He-Ne laser light (dashed line) is expanded and collimated so that the joint power spectrum grating can be addressed. The correlation output is formed by lens L2, and an interference filter IF and a polaroid P1 are used to suppress the background noise. The output correlation signal is detected by a CCD camera positioned at the back focal plane of the transform lens L2 and linked to the same frame grabber. These correlation images are captured by a microcomputer and then are processed with proper software.

Let us look at the response of the material to the interference pattern formed between the fields $r(-x_0, y_0)$ and $s(x_0, y_0)$. We also assume that the photorefractive crystal is thin, in the sense that the two fields are constant across the thickness of the crystal, and we can neglect any coupling between the two waves. In this case the amplitude of the refractive index variation induced in the material that gives rise to the first order cross-correlations is obtainable as (Cook, 1998)

$$\Delta n = n_0^3 r_{41} E_1\big(m(u,v)\big) \tag{5.3}$$

where $E_1(m(u,v))$ is calculated as a function of the modulation but also contains the phase information of the JPS, and may be written as

$$E_1\big(m(u,v)\big) = \big|E_1\big(m(u,v)\big)\big|\cos\big[x_0 u + \phi_S(u,v) - \phi_R(u,v)\big] \tag{5.4}$$

The JPS incident on the photorefractive BSO crystal has a certain modulation $m(u, v)$ for each spatial frequency

$$m(u,v) = \frac{2\sqrt{I_S(u,v) I_R(u,v)}}{I_S(u,v) + I_R(u,v)} \tag{5.5}$$

where $I_S(u,v)=|S(u,v)|^2$ and $I_R(u,v) = |R(u,v)|^2$ are the intensities of the two Fourier transformed incident fields, which are now acting as the writing beams.

We next assume that a third, plane-wave probe beam is Bragg-matched to the grating produced by the two writing beams and furthermore it is arranged that the presence of the probe beam does not perturb the grating. This is easily achieved for BSO since a He-Ne beam can be used as the third probe beam, and BSO is less sensitive to 633nm light. The probe beam is diffracted from the grating to produce a beam which, when inverse Fourier transformed, will give the desired correlation output.

Assuming that the diffraction efficiency is low and ignoring absorption, the amplitude diffraction efficiency, η' is derived from the intensity diffraction efficiency (Eq. (5.6)),

$$\eta' = \frac{\pi \Delta n L}{\lambda \cos\theta} \tag{5.6}$$

The probe is assumed to have unit amplitude, therefore the amplitude of the diffracted probe may be obtained using Eq's (5.3) - (5.6) to give

$$-\frac{\pi L n_0^3 r_{41}}{\lambda \cos\theta}\left|E_1\left(m(u,v)\right)\right|\cos\left[x_0 u + \phi_S(u,v) - \phi_R(u,v)\right] \tag{5.7}$$

which is of the form of a cross-correlation. Therefore, photorefractive materials can be used as the active media for real-time correlation and convolution processes.

The Fourier component of the transmittance function that generates the first-order correlation intensity signal can therefore be expressed as having the form

$$\left|E_1\left(m(u,v)\right)\right|\cos\left[x_0 u + \phi_S(u,v) - \phi_R(u,v)\right] \tag{5.8}$$

The choice of model used to describe the modulation of the space charge field depends on the particular characteristics of the system, in particular the intensity modulation.

We note that if $|R(u,v)| = |S(u,v)|$ for all (u,v) then $m(u,v)=1$, leading to a maximised, constant modulation of the space-charge field. This high modulation for all spatial frequencies will improve diffraction efficiency, increase the information contribution from the high frequency component, and result in phase-only correlation. This can be achieved for all (u,v) in practical terms by setting $|R(u,v)| = |S(u,v)| = 1$, which is possible by encoding the scene and reference to give phase-only distributions in the Fourier plane. Also various object and frequency space filtering techniques can be used to improve the performance of the photorefractive JTC.

5.3 Image Coding Technique

Since different kinds of filters will be used in this phororefractive JTC and these filters may have negative values as well as positive values, the image encoding technique is necessary in a photorefractive joint transform correlator. Since the object plane filters are real they can be encoded using two real, positive components, or pixels. The technique used for encoding the positive and negative values is derived from the method of subtraction based on the decomposition of the function in two parts (Vallmitjana, 1995; Cook, 1998), the positive and negative, and encoding in Ronchi gratings with the same frequency but with a π phase difference. This provides the subtraction of amplitudes in Fourier space.

A real two-dimensional function $h(x,y)$ may be expressed as the sum of two functions

$$h(x,y) = h^{+}(x,y) - h^{-}(x,y) \tag{5.18}$$

where

$$
\begin{aligned}
h^{+}(x,y) &= h(x,y) && \text{when } h(x,y) > 0, \\
&= 0 && \text{when } h(x,y) < 0, \\
h^{-}(x,y) &= -h(x,y) && \text{when } h(x,y) < 0, \\
&= 0 && \text{when } h(x,y) > 0.
\end{aligned}
\tag{5.19}
$$

Both $h^{+}(x,y)$, and $h^{-}(x,y)$ are real, positive functions and are called bipolar filters.

The transmission of a Ronchi grating may be expressed by its Fourier series expansion (Vallmitjana, 1995),

$$
r^{+}(x,y) = 1 + \sum r_n \sin\left(2\pi n x / p\right) \tag{5.20}
$$

where p is the spatial period. If the Ronchi grating is displaced by $p/2$, its transmission is

$$
r^{-}(x,y) = 1 - \sum r_n \sin\left(2\pi n x / p\right) \tag{5.21}
$$

Note that r^{+} and r^{-} alternate between the values 0 and 1 along the x-axis and that they are complementary gratings.

Now consider the following function

$$
\begin{aligned}
h_c(x,y) &= h^{+}(x,y)r^{+}(x,y) + h^{-}(x,y)r^{-}(x,y) \\
&= [h^{+}(x,y) + h^{-}(x,y)] + [h^{+}(x,y) - h^{-}(x,y)] \\
&\quad \times \sum r_n \sin(2\pi n x / p)
\end{aligned}
\tag{5.22}
$$

Its two-dimensional Fourier transform is given by

$$\begin{aligned} H_c(u,v) &= [H^+(u,v)+H^-(u,v)] \\ &\quad +[H^+(u,v)-H^-(u,v)]\otimes\sum r_n\delta(u-{}^{n}\!/_{p}) \\ &= [H^+(u,v)+H^-(u,v)] \\ &\quad +H(u,v)\otimes\sum r_n\delta(u-{}^{n}\!/_{p}) \end{aligned} \tag{5.23}$$

Finally by taking the Fourier transform of only one diffraction order we obtain the desired function *h(x, y)*.

The encoding of a digital function is carried out by representing each sampled value by using four pixels. Both left pixels are given the original value if it is positive, while the two right pixels remain at zero. Similarly, both right pixels are given the absolute of the original value if it is negative and the two left ones remain zero. Each set of two vertical pixels therefore forms part of a grating, the gratings arising from the positive and negative values are complementary and provide subtraction of amplitudes in the Fourier plane. Each sampled value was chosen to be represented by two vertical pixels after testing of other possibilities as part of this work.

5.4 Pattern recognition with the Photorefractive JTC

Now we use the architecture of the photorefractive JTC to realise optical pattern recognition. Using the set-up shown in fig. 5.3 with the BSO crystal, the single object and multiple object scenes and their output signals of a joint transfor correlator are shown in fig. 5.4 and fig. 5.5, respectively.

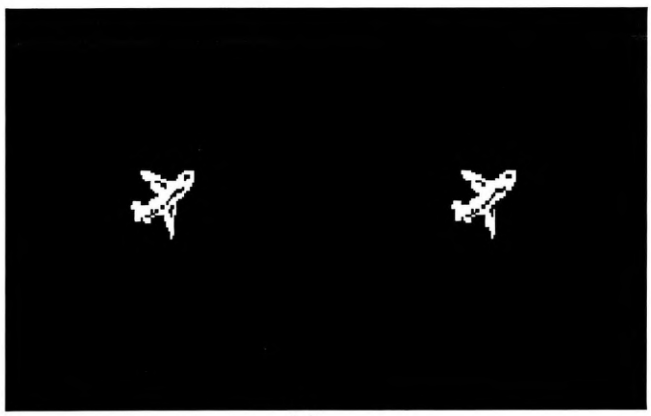

(a)

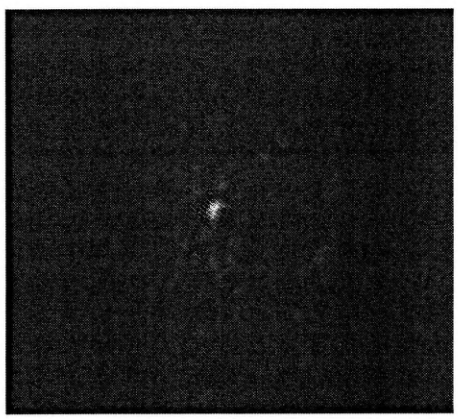

(b)

Fig. 5.4 The input plane (a) and the output plane (b) of a joint transform correlator with single input object.

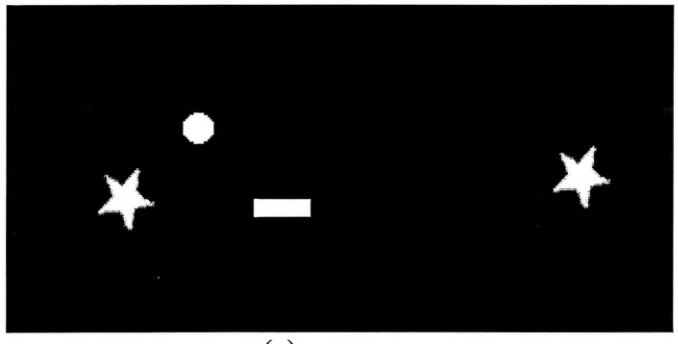

(a)

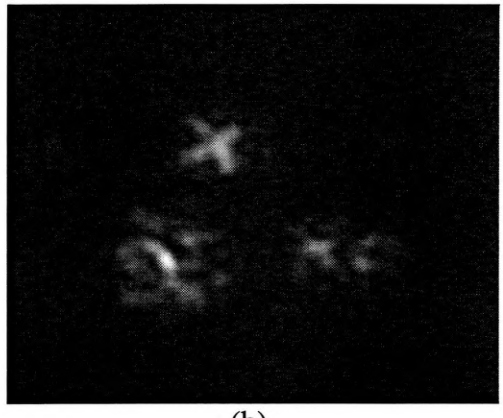

(b)

Fig. 5.5 The input plane (a) and the output plane (b) of a joint transform correlator with multiple input objects.

Other photorefractive materials also can be used as recording medium in the Fourier plane. Among them, doped potassium sodium strontium barium niobate SBN (KNSBN) is a frequently used recording materials. However, it has quite different properties compared with BSO. BSO has been widely used as a dynamic holographic medium in optical systems, since it has the advantages of the fast response, good optical quality over a large surface area, high spatial frequency response, and low writing and erasing energy. These make it suitable for real-time applications. KNSBN crystal is a kind of novel photorefractive material with large electro-optic coefficient, high Curie temperature, single domain and suitable spectrum sensitive range, which has attracted considerable attention in recent years (Chen, 1989; Sun, 1991). As the photorefractive crystal plays an

important role in the PJTC, we compared the properties of these two materials with the setup of Fig.5.3.

Firstly, we investigate the influence of the applied field on the output correlation signals. The English letter O has been chosen as the input image, which is correlating with the reference O. We started with BSO crystal, fig. 5.6 (a) shows the correlation output plane with an applied voltage of +5 kV, then we reduce the voltage gradually, fig 5.6 (b) shows the output under 3 kV. It is evident that the correlation peak intensity has reduced a lot (nearly 80%). Fig 5.7 shows the peak correlation intensity (PCI) varying with the applied voltage. It shows that in the range from 5kV to 3kV, the peak correlation intensity almost varies linearly with the reduction of the applied voltage, from 3 kV to 0kV, there is no visible correlation peak. The output correlation signal depends

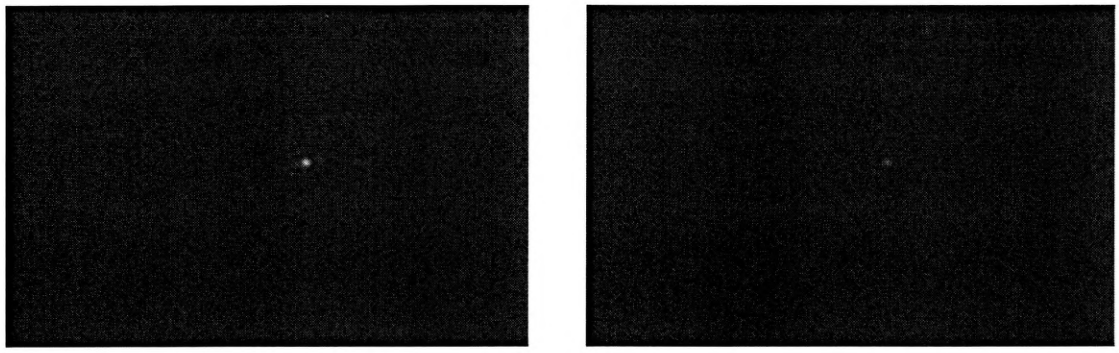

(a) (b)

Fig. 5.6 The output plane of the photorefractive JTC with BSO and, (a) applied field filed of 5kV, (b) applied field of 2kV.

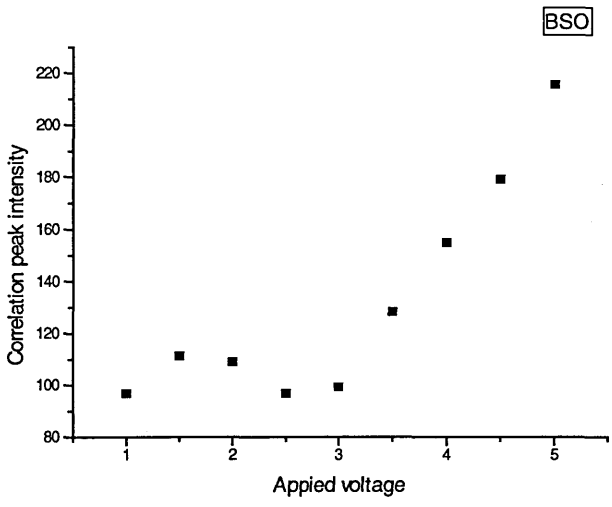

Fig. 5.7 The peak correlation intensity for various applied fields on the BSO crystal.

largely on the applied voltage on the BSO crystal, i.e., the optical properties of the BSO crystal depends largely on the applied voltage, without applied field, BSO crystal can not record the fringe formed by the joint power spectrum effectively. Fig 5.8 shows the SNR varying with the applied voltage. It varies in the similar way as fig. 5.7.

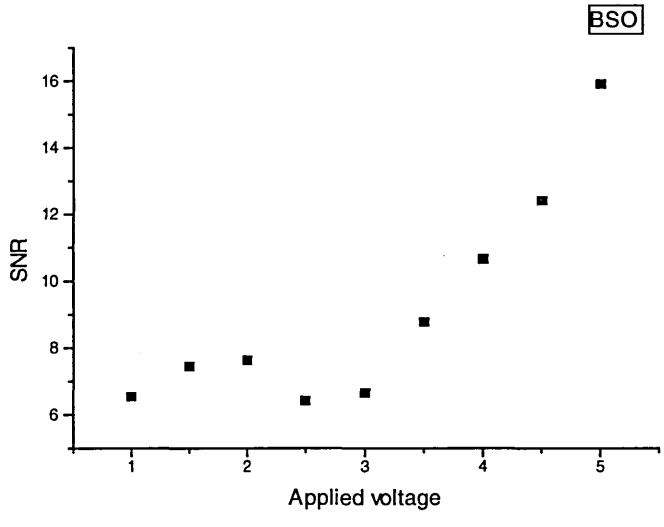

Fig. 5.8 The SNR of the output varies with applied voltage.

Then a KNSBN crystal replaced BSO in the setup. Fig 5.9 is the correlation output signals with SBN in the Fourier plane, (a) is the correlation without applied field and (b) is the output with applied voltage of 3kV, this is the highest voltage we apply on the crystal, higher one may probably cause damage to the crystal we used. Comparing the two images, the second one is not as neat as the first one. It seems that the fringes in the crystal get into a kind of confusion along with applied field, and consequently the correlation output is messed up. Also, the signal is not as steady as the one without

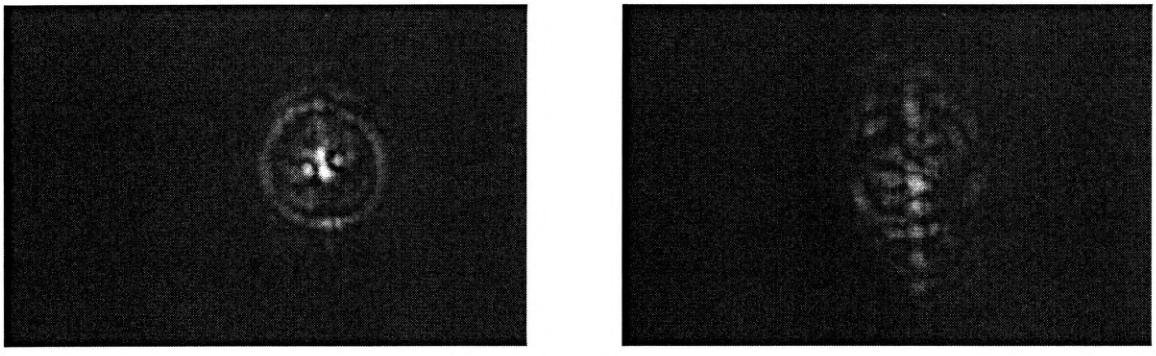

(a) (b)

Fig. 5.9 The output plane of the photorefractive JTC with SBN and, (a) no applied field, (b) applied field of 3kV

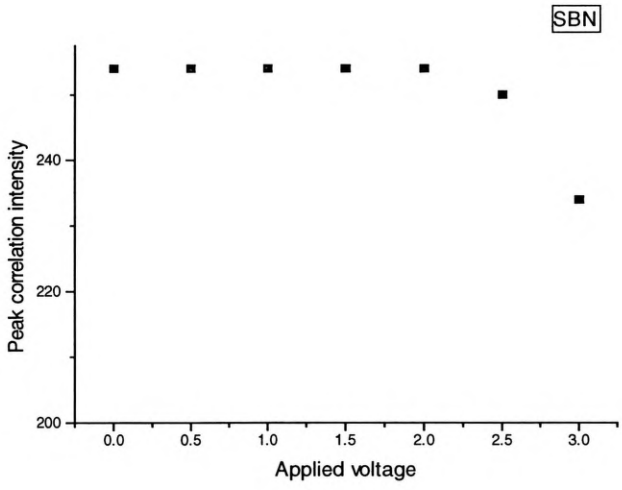

Fig. 5.10 The dependence of the peak correlation intensity upon applied field on the KNSBN crystal

applied voltage, the peak intensity of correlation output vibrates evidently from time to time. Fig.5.10 describes how the peak correlation intensity depends on the applied voltage. From 0kV to 2.5 kV, the PCI shows no visible change, after that, while the voltage carries on increasing, the PCI starts to decrease; at 3kV, the PCI was reduced by 10%. This is not particularly serious, but the signal-to-noise ratio, which is defined as the ratio of the peak correlation intensity to the mean intensity outside the 50% peak, shows a more serious decrease. Fig. 5.11 shows the SNR of the output plane varying with the applied field. When the applied voltage is restricted to within 1kV, the SNR almost remains unchanged and the contour of the correlation patterns shows no obvious difference, beyond this limit the SNR has an evident drop (a 31% decrease from 1kV to 1.5kV), when the applied voltage reaches 3kV, the SNR drops by as much as 50%.

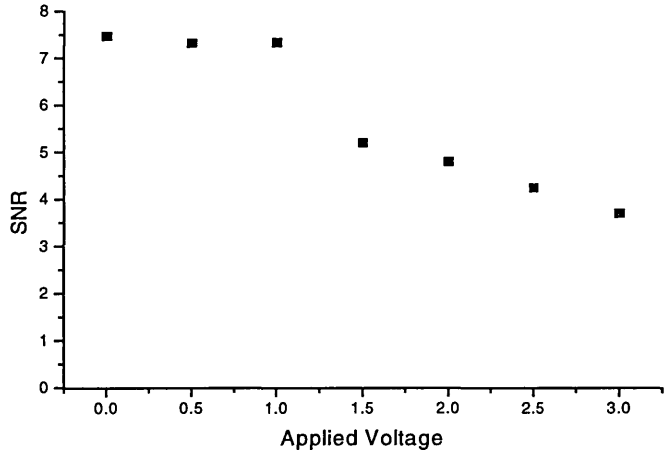

Fig. 5.11 The variance of the SNR of the correlation signal vs. applied voltage on KNSBN

Evidently the applied field can hardly improve, if not worsen, the correlation output. Also, no matter whether there is an applied field, the correlation performance of the JTC with KNSBN is not as good as that with BSO, the correlation peak of the correlator with

KNSBN is much broader than that with BSO, and the highest SNR is only1/3 of that of BSO.

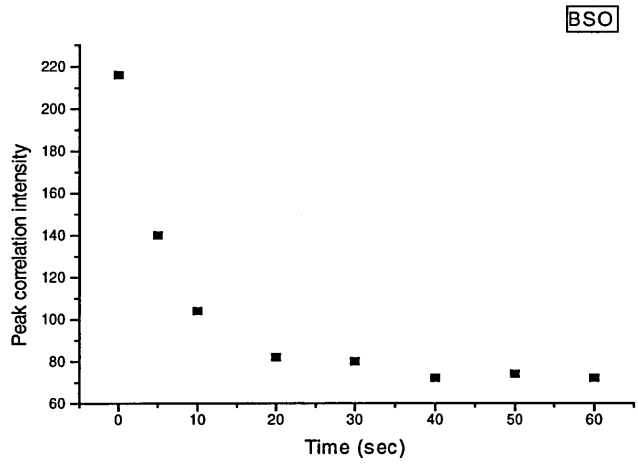

Fig. 5.12 The variation of the peak correlation intensity along erasure time (BSO)

Next, we investigate the grating erasure time of the two crystals. Fig. 5.12 is the variation of the peak correlation intensity (the applied voltage is 5kV) after shutting down the write beam. It is shown that the correlation intensity asymptotes (the correlation signal disappears completely from the screen of monitor) in about 15 seconds. The period of erasure can become much shorter than 15 seconds if an erasure beam is used to illuminate the crystal. The property of fast erasure is useful for updating images in real time processing. For KNSBN, the situation is totally different. During the first 30 minutes after switching off the incident beam, there is no evident change of the correlation pattern on the monitor. Fig.5.13 shows the change of PCI (without applied field) after the write beam has been turned off. It needs about 150 minutes for the correlation signal to disappear from the screen. If we use another argon beam to illuminate the crystal, the process of erasure can be shortened.

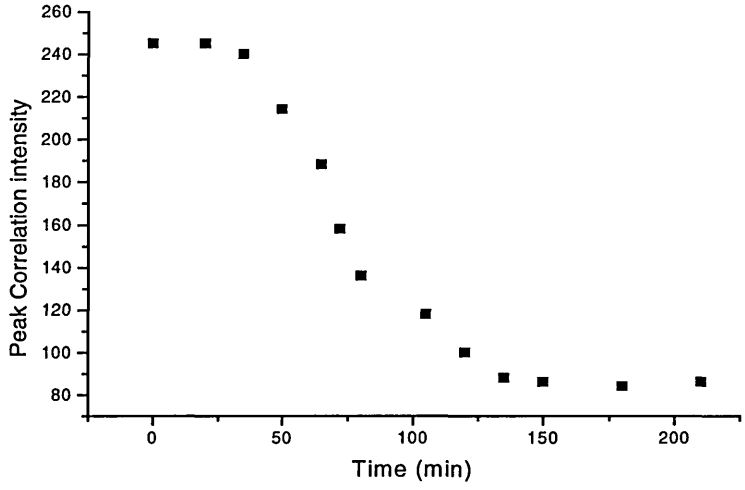

Fig. 5.13 The change of the peak correlation intensity with the erasure time (KNSBN)

In this section, we have investigated the performance of the photorefractive crystals BSO and KNSBN in a joint transform correlator. The correlation output patterns from the JTC with both crystals, the dependence on applied field, the variation of the signal-to-noise ratio, and the time to erase gratings inside the crystals are compared. BSO can only work effectively under the condition that it is used with an appropriate high-voltage, and the short grating erasure time makes it suitable for real time processing. On the other hand, SBN can work as a recording material with or without an applied field, in fact, the signal-to-noise ratio of the correlation output without an applied field is higher than that with an applied field. The time needed for erasing the grating inside the SBN crystal is much longer than the BSO. Generally, the JTC with the crystal KNSBN performs not so well as the one with BSO, the correlation peak is broader and the signal-to-noise is lower. However, the memory of this crystal may make it an ideal material for other uses, such as optical storage.

Nevertheless, the photorefractive JTC for pattern recognition has its deficiencies, such as low discrimination, and broad correlation peaks. The next a few chapters deal with the

methods to improve the performance of a photorefractive JTC by additional processing of the reference and scene functions.

Chapter 5: References

S. Bian, and J. Frejlich, "Actively stabilized holographic recording for the measurement of photorefractive properties of a Ti-doped KNSBN crystal", J. Opt. Soc. Am. B, **12**, 2060-2065 (1995).

A.Carnicer, E. Martin-Badosa, I. Juvells and S. Vallmitjana, "Spatial envelop-free nonlinear joint transform correlator", Opt. Comm. 114, 336-343 (1995).

H. C. Chen, Y. H. Xu, " Growth and some properties of undoped and doped $(K_{1-x}Na_x)_{0.4}(Sr_{1-y}Ba_y)_{0.8}Nb_2O_6$ single crystals with tungsten-bronze structure," J. Crys. Grow. **96**, 357-362 (1989).

N.J. Cook, "Properties and processing applications of photorefractive BSO", PhD thesis (University of Abertay Duindee, Supervisor: Colin M. Cartwright), Chapter 4, 1998.

D.A. Gregory, " Real-time pattern recognition using a modified liquid crystal television", Appl. Opt., **25**, 467-469 (1986).

S. Jutamulia, T.W. Lin and F.T.S. Yu, "Real-time noncoherent correlator using liquid crystal television", Opt. Comm. 64(2), 115-119 (1987).

J.C. Kirsch, D.A. Gregory, M.W. Thie and B.K. Jones, "Modulation characteristics of the Epson liquid crystal television", Opt. Eng. 31(5), 963-969 (1992).

B. L. Liang, Z. Q. Wang, G. G. Mu, J. H. Guan, and C. M. Cartwright, "Diffraction properties of transmission photorefractive volume gratings in a Ce:KNSBN crystal", Appl. Opt., **38**(26), 5552-5555 (1999).

H.K. Liu, J.A. Davis and R.A. Lully, "Optical-data-processing properties of a liquid-crystal television spatial light modulator", Opt. Lett., **10**, 635-637 (1985).

P. L. Ramazza, and M. J. Zhao, "Experimental study of two-wave mixing amplification in Cu-doped KNSBN," Opt. Commun. **102**, 93-99 (1993).

D. Sun, J. Chen, X. Lu, Y. Song, Z. Shao, and H. Chen, "Growth and self-pumped phase conjugation of Ce-doped $KNa(Sr_{0.61}Ba_{0.39})_{0.9}Nb_2O_6$ crystal," J. Appl. Phys. **70**(1), 33-35, (1991).

Y. Tomita, J. Bergquist, and M. Shibata, "Photorefractive properties of undoped, Cr-doped, and Cu-doped potassium sodium strontium barium niobate crystals" J. Opt. Soc. Am. B **10**(1),94-99 (1993).

S. Vallmitjana, A. Carnicer, E. Martin-Badosa, I. Juvells, "Nonlinear filtering in object and Fourier space in a joint transform optical correlator: comparison and experimental realization", Appl. Opt. **34**, 3942-3949 (1995).

H. Y. Wang, M. Z. Tian, J. L. Lin, S. H. Huang, J. Q. Yu, H. C. Chen, and Q. Z. Jiang, "Study of two-wave coupling in Cu:KNSBN using red light," Opt. Commun. **115**, 563-567 (1995).

J. Xu, Y. Wu, S. Liu, G. Zhang, D. Sun, Y. Song, and H. Chen, "High-performance self-pumped phase conjugator with a multichannel in KNSBN:Cu crystal", Opt. Lett., **16**, 1255-1257 (1991).

F.T.S. Yu, S. Jutamulia, T.W. Lin and D.A. Gregory, "Adaptive real-time pattern recognition using a liquid crystal TV based joint transform correlator", Appl. Opt., **26**, 1370-1373 (1987).

H. Zhang, B. Guo, H. Jiang, Y. Shih, and L. Yan, "Characterization of the KNSBN:Cu crystal with two-wave coupling at visible and infrared wavelengths," Appl. Phy. B. **61**, 207-211 (1995).

J. Zhang, H. Lui, and W. Jia, "Investigation into self-pumped mutually pumped phase conjugation with beams entering the negative c face of doped $(K_{0.5}Na_{0.5})_{0.2}(Sr_{0.75}Ba_{0.25})_{0.9}Nb_2O_6$ crystal", Appl. Opt., **36** 3753-3761 (1997).

Chapter 6 Triple Joint Transform Correlator

6.1 The optical Incoherent –Erasure Technique

The joint transform correlator (JTC) (Weaver, 1966) is well known as a useful tool for pattern recognition. It has the advantages of the ease of updating the image in real time, easy implementation and robustness to optical alignment as compared with the VanderLugt correlator (VanderLugt, 1964). However, the conventional JTC performs in all aspects as a matched-filter-based correlator (Khoury, 1994), which suffers from some deficiencies, such as broad correlation peaks and relatively low discrimination ability. In order to improve the performance of the conventional JTC in terms of discrimination ability, as well as the signal-to-noise ratio, several correlation filters have been designed and additional non-linearizing methods (Javidi, 1989; Horner, 1992), such as thresholding and binarizing , have been employed. There have been various techniques proposed in recent years. In these methods, either the reference images are pre-processed to achieve different filters and different levels of nonlinearity or the joint power spectra are processed directly in the Fourier plane. Either way, the property of real-time loses since computer time is needed to processing images or JPS.

In recent years, the use of the incoherent-erasure beam in two-beam-mixing and four-beam-mixing geometries in photorefractive materials has been shown to modify the spatial frequency characteristics of the wave-mixing processing (Alam, 1998). It allows one to perform incoherent-coherent conversion and realizes many real-time spatial frequency operations, novelty filtering and optical correlation.

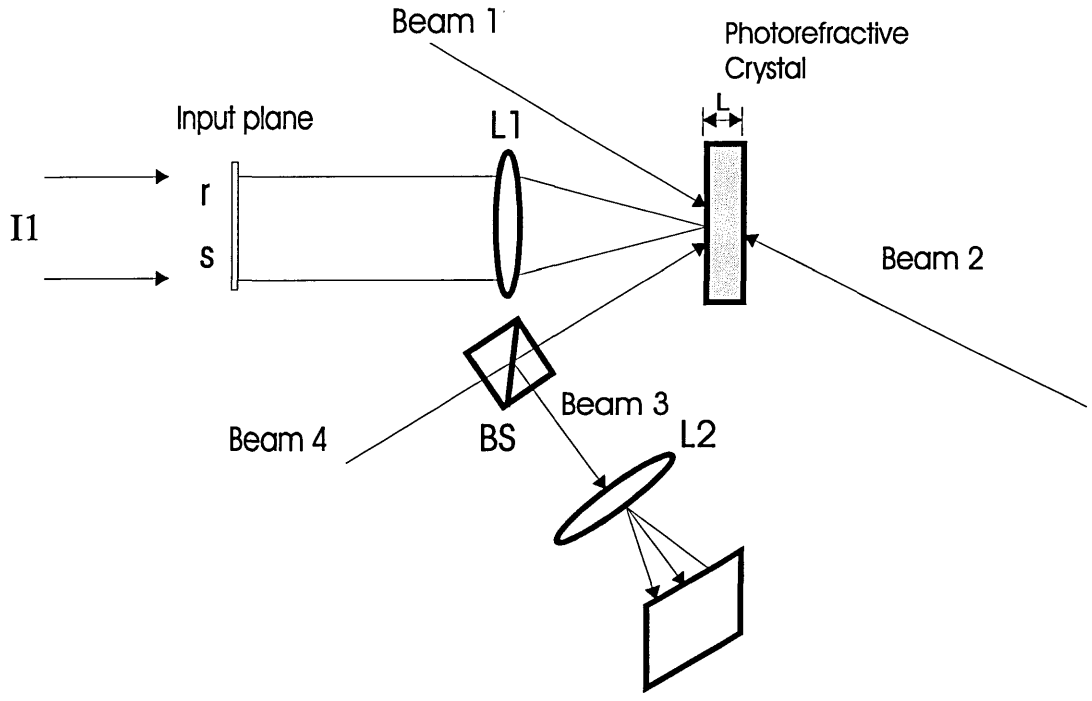

Fig. 6.1 Incoherent-erasure JTC architecture

As an example, the architecture of the incoherent-erasure joint optical correlator is shown in Fig. 6.1, where coherent beams 1 and 4 write a grating in a photorefractive crystal. This grating is read out by the coherent beam 2 to generate a phase conjugate beam, i.e., beam 3, as shown in fig.6.1. Another beam I_i with wavelengths λ_i, which is temporally incoherent with write beams 1 and 4, passes through the input joint image which is Fourier transformed by lens L_1, which is focused into the photorefractive crystal to produce the JPS. The JPS is formed inside the crystal to generate charge carriers. These charge carriers generated in the crystal reduce the grating contrast or erase it. This erasure is dependent on the intensity $|R(p,q)+S(p,q)|^2$. Consider a photorefractive crystal with a coupling coefficient γ, thickness L in the direction of propagation, and a small absorption coefficient α. Before the erasure beam is introduced, the phase conjugate beam amplitude A_3' in the undepleted pump case is given by (Alam, 1998)

$$A_3' = \frac{A_1 A_4^* A_2 \gamma L}{I_c} = m\frac{A_2}{2}\gamma L \tag{6.1}$$

where * denotes the complex conjugate operation, m represents the grating modulation index, defined by

$$m = \frac{2A_1 A_4^*}{I_c} \tag{6.2}$$

and I_c represents the total intensity of the coherent beams (1, 2 and 4) incident on the crystal, given by

$$I_c = |A_1|^2 + |A_2|^2 + |A_4|^2 \tag{6.3}$$

where A_1, A_2 and A_4 represent the complex amplitude of the beam 1,2, and 4, respectively.

As the JPS is focused on the crystal, the generation of charge carriers by the absorption locally erases the existing grating. The erasure is dependent on the intensity of the JPS, i.e., the joint transform interference grating $|R(p,q)+S(p,q)|^2$. The effective index of modulation m_{eff} after erasure, is given by

$$m_{eff} = \mu\left\{1 + (I_i / I_c)[R(p,q)+S(p,q)]^2 (\lambda_i f_1)^2 (\alpha_i \lambda_i)/(\alpha_c \lambda_c) \exp[(\alpha_c - \alpha_i)L]\right\} \tag{6.4}$$

where I_i represents the intensity of the input beam before passing through the input joint image; α_c and α_I are the absorption coefficients corresponding to the coherent and input beam wavelengths λ_c and λ_I, respectively; and f_i is the focal length of lens L_1. The amplitude of the phase conjugate beam after erasure can be expressed as

$$A_3(p,q) = [(A_1 A_4^*) A_2 \gamma L] / \left\{ I_c + I_i \frac{|R(p,q)+S(p,q)|^2}{(\lambda_i f_1)^2 (\alpha_i \lambda_i / \alpha \lambda_{cc}) \exp[(\alpha_c - \alpha_i)L]} \right\} \tag{6.5}$$

Using Eq. (6.1), Eq. (6.5) can be written as

$$A_3(p,q) = A_3^{'} / \left\{ 1 + \frac{(I_i / I_c)\left|R(p,q) + S(p,q)\right|^2}{(\lambda_i f_1)^2 (\alpha_i \lambda_i / \alpha_c \lambda_c) \exp[(\alpha - \alpha_{ic})L]} \right\} \\ = A_3^{'} t(p,q) \tag{6.6}$$

In Eq. (6.6), $t(p,q)$ represents the input-output nonlinear transfer function of the incoherent-erasure JTC and can be expressed as

$$t(p,q) = \frac{1}{1 + r_{eff}(p,q) E(p,q)} \tag{6.7}$$

where $E(p,q)$ is the transmitted normalized energy spectrum and $r_{eff}(p,q)$ is the effective beam ratio, which are defined as

$$E(p,q) = \frac{\left|R(p,q) + S(p,q)\right|^2}{E_0^2} \tag{6.8}$$

and

$$r_{eff}(p,q) = \frac{E_0^2}{(\lambda_i f_i)^2} \frac{I_i}{I_c} \frac{\alpha_i \lambda_i}{\alpha_c \lambda_c} \exp[(\alpha_i - \alpha_c)L] \\ = \frac{r_0 E_0^2}{(\lambda_i f_1)} \frac{\alpha_i \lambda_i}{\alpha_c \lambda_c} \exp[(\alpha_i - \alpha_c)L] \tag{6.9}$$

where E_0 is the integrated transmissivity of the input joint image $g(x,y)$, and $r_0 = I_i / I_c$ is the integrated beam ratio. The effective beam ratio is controlled by the experimental settings and the material characteristics and sensitivity for different wavelengths. It has been proved that this incoherent erasure technique can largely improve the performance of the joint transform correlator (Alam, 1998).

6.2 Coherent Triple Joint Transform Correlator

In this section, we present a coherent method to modify the matched-filter-based joint transform correlator. In our implementation, in addition to the two beams forming the joint power spectrum in the Fourier plane, a third coherent beam is used to generate filters or non-linearity in order to increase the discrimination capability of the joint transform correlator. The three beams form a so-called triple correlator. By the technique of triple correlation, we can change the Fourier spectrum and improve the correlation performance. For example, the triple correlation technique makes it possible to utilise only phase information at the Fourier plane by putting a pre-processed reference image in the third beam. The image in the third beam is calculated from a theoretical filter or a nonlinear processing technique, and then transferred into object space. The experiment is implemented with a liquid crystal television as the third input image, and a photorefractive crystal BSO is used as the dynamic holography medium in Fourier space. The filter encoding techniques are also necessary to encode the negative values of the third beam (Vallmitjana, 1995). The computer simulation and experimental results show that the triple correlation improves the performance of joint transform correlation.

It is known that the conventional JTC has some drawbacks such as low discriminations. In order to avoid these shortcomings, there are many ways in which references are processed before they are displayed in the input plane of the JTC. Assuming that after the processing, the reference becomes $r'(x-x_0,y)$, and the cross correlation term in the Fourier plane should be $R'(p,q)S^*(p,q)\exp(-j2x_0p)$, instead of $R(p,q)S^*(p,q)\exp(-j2x_0p)$. Efforts have been made in choosing the $r'(x-x_0,y)$ to achieve sharp correlation peaks and high discrimination ability.

Now a method is introduced to process the reference image, instead of filtering the reference in advance, we use the third beam to filter it or change it at the Fourier plane.

Assume that the image in the third beam, which is coherent to the others, is e(x-x_0, y), then we obtain the joint power spectrum of three images

$$\begin{aligned}|H'(p,q)|^2 &= |R(p,q)+E(p,q)+S(p,q)|^2 \\ &= |R'(p,q)+S(p,q)|^2 \\ &= R'(p,q)R^*(p,q)+S(p,q)S^*(p,q)+R^*(p,q)S(p,q)\exp(j2x_0p) \\ &+ R'(p,q)S^*(p,q)\exp(-j2x_0p)\end{aligned} \tag{6.10}$$

By choosing the form of E (p, q), we can change the Fourier spectrum R(p, q) to R'(p,q), and thereby enhance the output correlation performance. For example we can choose E(p, q) to make R'(p,q) be a phase-only or a binary phase-only filter. For a phase-only filter, it should be

$$R'(p,q) = R(p,q)+E(p,q) = \frac{R(p.q)}{|R(p,q)|} \tag{6.11}$$

Thus

$$E(p,q) = \frac{R(p,q)}{|R(p,q)|} - R(p,q) \tag{6.12}$$

And for the binary phase only filter

$$R'(p,q) = R(p,q)+E(p,q) = \begin{cases} 1 & \text{for } R'(p,q) \geq V_T \\ 0 & \text{for } R'(p,q) < V_T \end{cases} \tag{6.13}$$

V_T is the threshold value, E(p, q) can be calculated pixel by pixel. And the best filter can be chosen by varying the threshhold value.

Because e(x, y) is a real image in the object plane, so E(p, q) must be transferred to e(x, y) by a inverse Fourier transform. After that, this image is a real function taking

positive and negative values in different zones. To implement an image in an amplitude optical modulator or a photographic register, the amplitude transmission should be non-negative. One possibility to encode an image in real space with only positive values is to use holographic techniques. There are several methods to be chosen. One of the techniques used for coding is, as shown in section 5.3, to decompose the function in two parts, the positive and negative part, which are encoded in Ronchi gratings with the same frequency but in opposition of phase.

6.2.1. Computer simulation results

In the computer simulations, the performance of the triple correlator and conventional joint transform correlator were compared. The performance criteria used are the correlation peak intensity (CPI) with a quantization of 0-255, the signal-to noise ratio (SNR), the peak to sidelobe ratio (PSR) and the half-correlation-peak-width (HCPW). The SNR is defined as the ratio of the peak correlation intensity to the mean intensity outside a 50% peak value in the correlation which represents the sharpness of the correlation peak and determines the chance of an error in pattern recognition. The peak to sidelobe ratio (PSR) is defined as the ratio of the auto-correlation peak intensity to the highest cross-correlation correlation peak intensity. HCPW is the width of the correlation term at half its peak value (measured as pixel numbers). A micro-computer and IDL software were employed for the simulations.

First, the simulation is performed with a single object English letter O and the reference O in the input plane. Fig. 6.2 shows (a) image in the input plane, (b) three dimensional plot of the correlation output with conventional JTC and (c) three dimensional plot of the correlation output with triple corrrelator. In the next step, the performance of the triple correlator was tested with multiple objects. Three English letters "O G A" are in the scene. Fig 6.3 shows (a) image in the input plane, (b) three dimensional plot of the correlation output with a conventional JTC and (c) three dimensional plot of the correlation output with triple correlator. It is apparent from these

plots that the correlation performance is improved by employing the third beam. Sharper correlation peaks and higher discrimination ability have been observed.

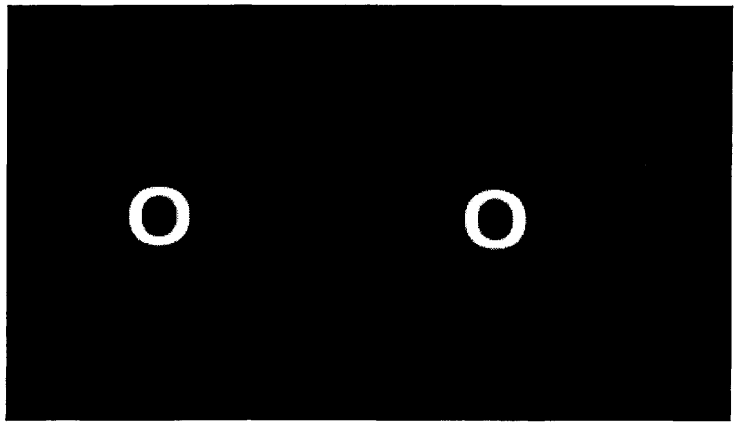

(a)

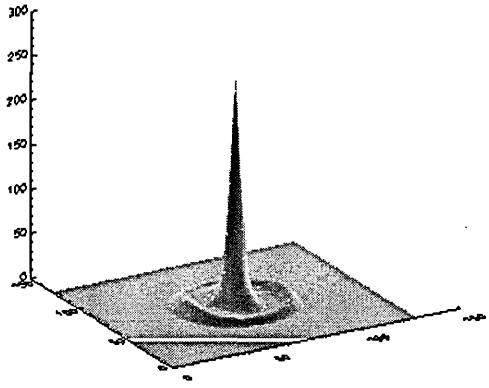

(b)

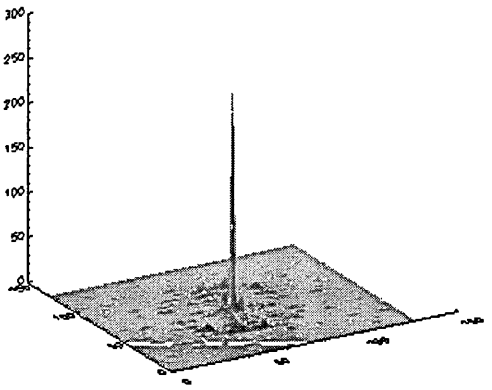

(c)

Fig.6.2 Computer simulation results with single object, (a) input image, (b) three dimensional plot of the correlation output with conventional JTC, (c) three dimensional plot of the correlation output with triple JTC.

(a)

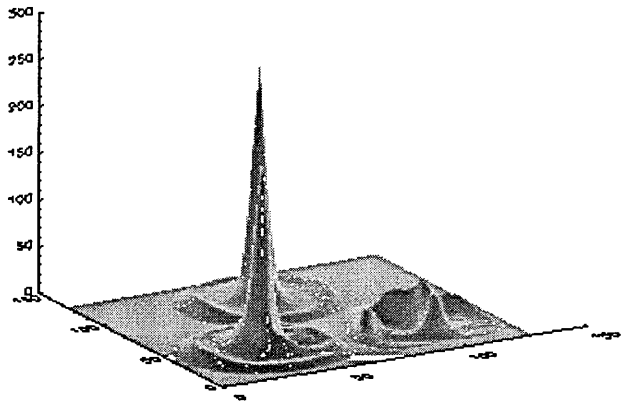

(b)

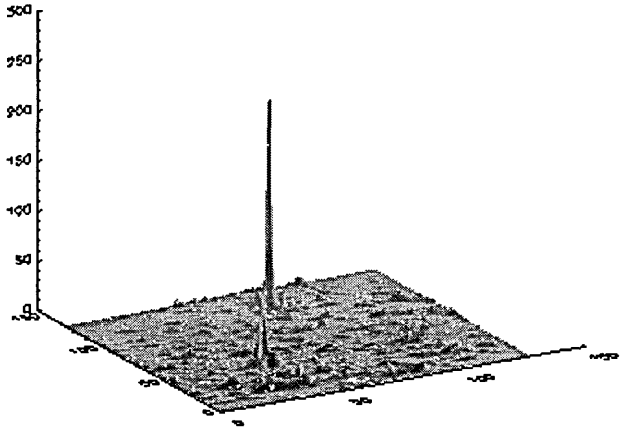

(c)

Fig.6.3 Computer simulation results with multiple objects, (a) input image, (b) three dimensional plot of the correlation output with conventional JTC, (c) three dimensional plot of the correlation output with triple JTC.

To illustrate the correlation performance more clearly, some numerical results are shown in Table 6.1. Column 1 lists the type of correlators. CJTC denotes the conventional joint transform correlator and TJTC denotes the triple correlator. Columns 2 - 5 list the peak-correlation-intensity, signal-to-noise ratio, correlation peak-to-sidelobe ratio and the half-correlation-peak-width. It is shown that the SNR and PSR have improved by a factor of 5 and 3 respectively, and the HCPW has reduced from 33 pixels to 2 pixels.

	CPI	SNR	PSR	CHPW
CJTC	230	140	1.3	33
TJTC	255	876	3.1	2

Table 6.1. Computer simulation results of correlation output with CJTC and TJTC.

6.2.2 Experimental Results

Fig.6.4 shows the experimental arrangement used. The argon ion laser was operated at λ=514.5nm and the beam was expanded and collimated to 42mm in diameter by BE1. The polarisation beam splitter (PBS1) was used to divide the argon laser beam in two beams, one beam acts as a joint correlation beam and the other acts as the third beam. The beam ratio can be adjusted by rotating the first half-wave plate HWP1. L1 and L2 are transform lenses and have the same focal length. The scene and reference images are displayed side by side in IP1. The distance between the scene and reference makes a fringe spacing of 12.3μm. Images of 768 x 512 pixels are generated by a frame grabber and scaled to ensure correct registration of pixel on the LCTV in the position of IP2. The angles of polariser (P) and analyser (A) are chosen to give LCTV amplitude mostly modulation. The Fourier transform is formed at the BSO crystal which is positioned at the common back focal plane of the lenses L1 and L2. Half-wave plates HWP2 and HWP3 are used to change polarization direction to vertical. In the read-out part, He-Ne laser light (λ = 633nm) is expanded and collimated by BE2. Half-wave plate HWP4 with a polaroid P1 varies the beam intensity, so that the joint power spectrum grating can be read by a low power He-Ne laser. The correlation output is formed by transform lens L3, and an interference filter IF and a polaroid P2 are used to suppress the background noise. Then the image is detected by a CCD camera positioned at the back focal plane of the transform lens L3 and linked to the same frame grabber. The received images are captured by a micro-computer and then are processed using IDL software. M (1-3) are mirrors. BS1 and BS2 are beam splitters.

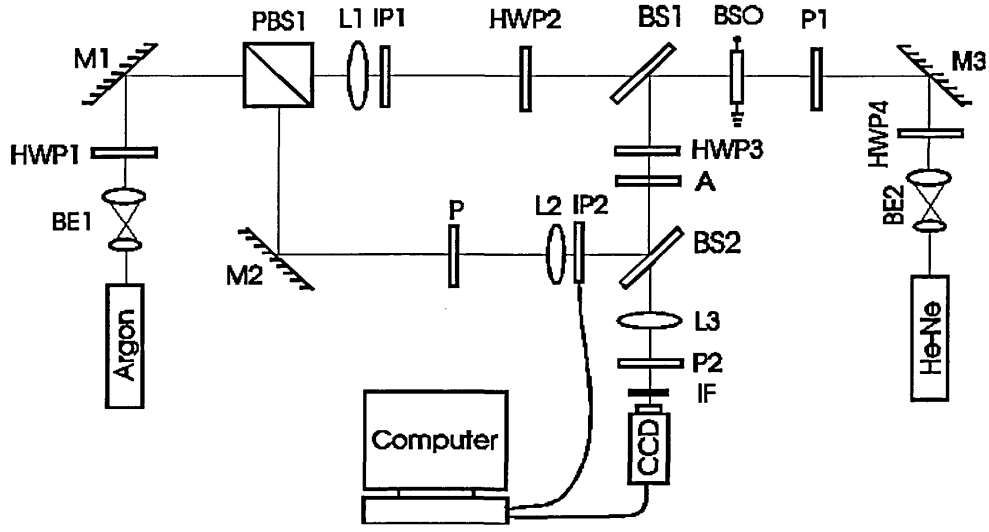

Fig. 6.4 Triple JTC experimental set-up

Three different scenes are used for the experiment. Fig 6.5, 6.6, and 6.7 shows three input images and their correlation results, respectively, in which (a) is the input images, (b) is correlation output planes of conventional JTC, c) is correlation output planes of the triple JTC, (d) is three-dimensional plots of the conventional JTC and (e) is three-dimensional plots of the triple correlation. The three scenes are the single English letter O , multiple English letters O, A and G correlating with the letter O and the shapes Star-Circle-Rectangle correlating with Star. It is apparent from these results that the auto-correlation peaks from the triple JTCs are sharper than the conventional ones, and for multiple objects the cross-correlation peaks are suppressed more than conventional ones. However, the background noise level increases a little with the triple JTC, partly because the coherent noise caused by three beams is greater than just the two. The standard deviation of the background noise increases as much as from 5.2 (CJTC) to 8.6 (TJTC). Table 6.2 lists the correlation results of the two type correlators numerically. The correlation results of Fig 6.5, Fig. 6.6 and Fig. 6.7 are shown in rows 1,2 and 3, respectively. Column 1 lists the types of correlators, CJTC denotes conventional JTC and TJTC denotes triple JTC. Column 2, 3, 4 and 5 list the peak-correlation-intensity, the

signal-to-noise ratio, peak-to-sidelobe ratio and half-correlation-peak-width for different images and different correlators. It is shown that among all the criteria, the PSR has highest enhancement with the triple correlation technique in experiment.

(a)

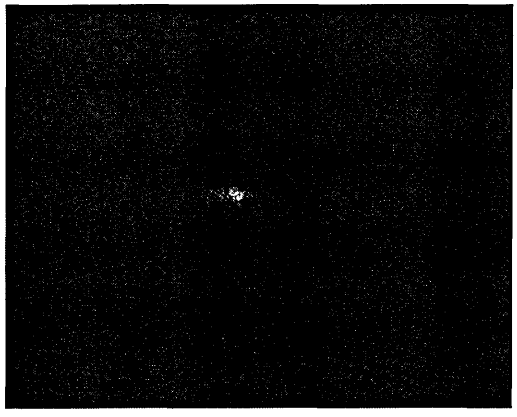

(b)

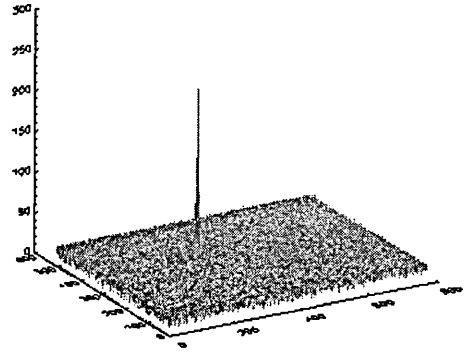

(d)

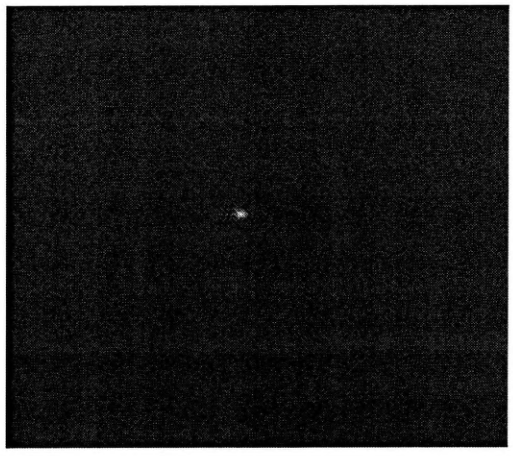

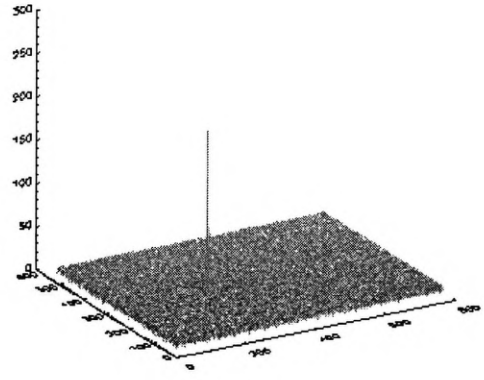

(c)

(e)

Fig. 6.5 Experimental results with single object, (a) input image, (b) Correlation output plane of CJTC, (c) correlation output plane of TJTC, (d) three dimensional plot of (b), (e) three dimensional plot of (c).

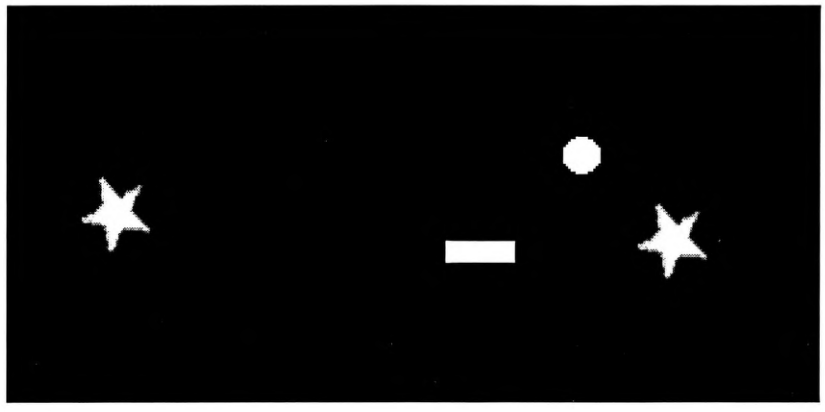

(a)

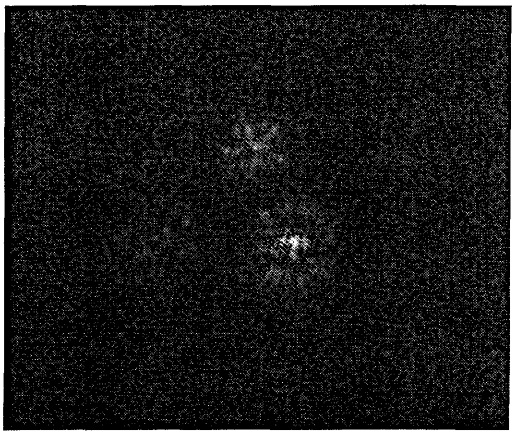

(b)

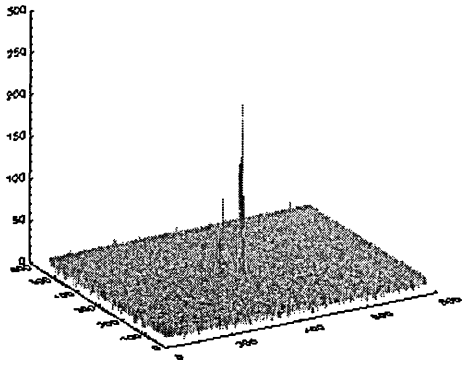

(d)

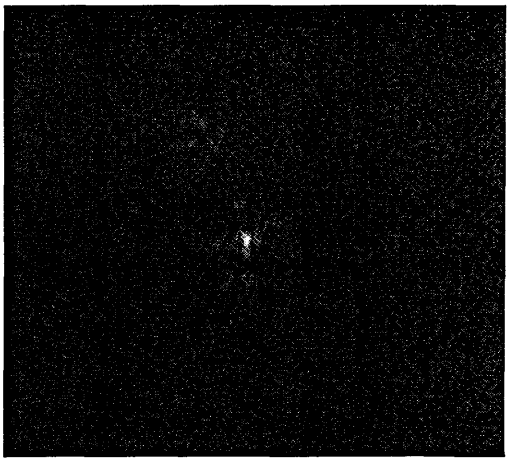

(c)

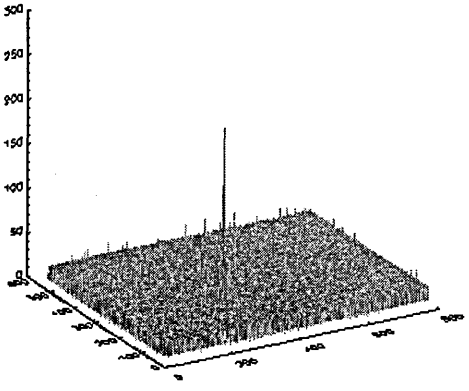

(e)

Fig. 6.6 Experimental results with multiple literal objects, (a) input image, (b) Correlation output plane of CJTC, (c) correlation output plane of TJTC, (d) three dimensional plot of (b), (e) three dimensional plot of (c).

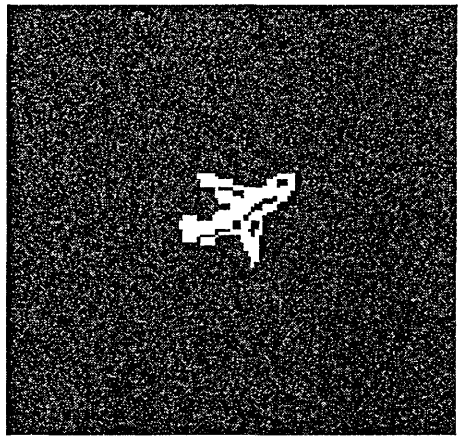

(a)

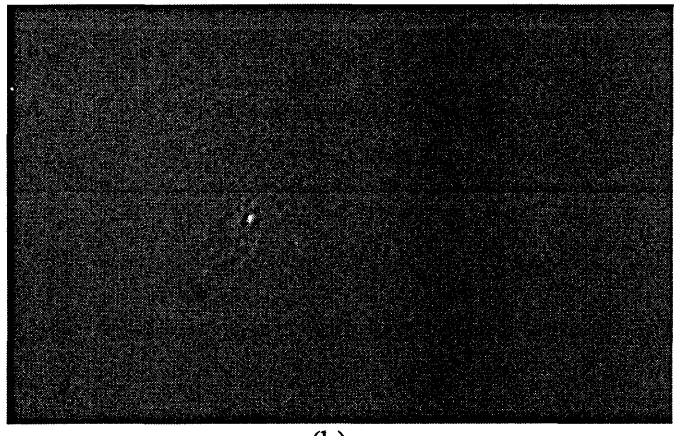

(b)

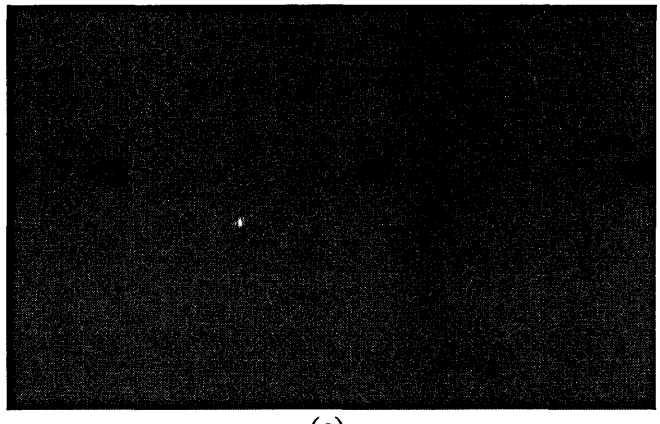

(c)

Fig. 6.7 Experimental results with multiple non-literal objects, (a) input image, (b) Correlation output plane of CJTC, (c) correlation output plane of TJTC.

		PCI	SNR	PSR	HCPW
1	CJTC	118	14	--	15
	TJTC	111	18	--	2
2	CJTC	126	17	2.6	18
	TJTC	116	19	6.7	12
3	CJTC	141	11	--	16
	TJTC	106	15	--	9

Table 6.2. Experimental results of correlation output with CJTC and TJTC.

In this way, the frequency spectrum in the Fourier plane of a conventional joint transform correlator has been modified with a third coherent beam and an encoded image in its object plane as the third input. The image could be chosen to implement a special filter or as a non-linearity. Both computer simulations and experimental results show that correlation performance has been improved with this method. However, in the experiment employing the third beam, especially in the case of multiple objects, the background coherent noise has increased a little.

6.3 Incoherent Triple Joint Transform Correlator

Just for a comparison, the correlation results of incoherent TJTC are listed in the last section of this chapter. The difference of the incoherent triple JTC from the coherent triple JTC here is the filter which is put into the incoherent read-out He-Ne beam. The experimental set-up is shown in Fig. 6.8. The implementation is similar with photorefractive JTC. The only difference is that the band-pass functions are displayed at IP1 filtering the JPS.

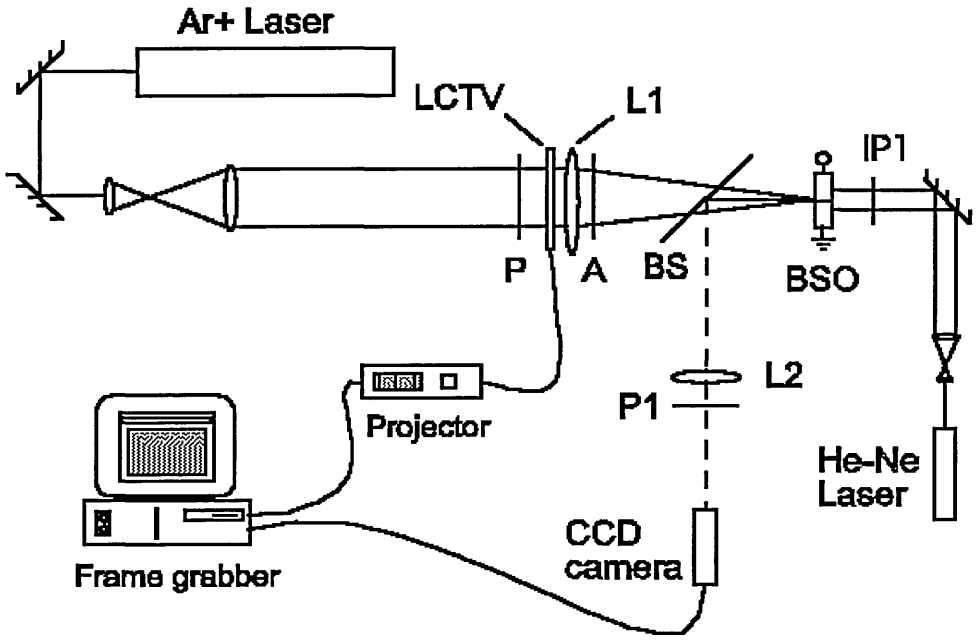

Fig. 6.8 The experimental set-up

The correlation term in the Fourier plane becomes

$$I' = R(p.q) * S(p,q) * T(p,q) \tag{6.14}$$

where T(p, q) is the third image inserted in the read-out beam to produce a band-pass operation. The experimental results are shown in the fig. 6.9 and 6.10. It is obvious that the filters have made the correlation peak become sharper, but caused some loss of correlation peak intensity.

(a)

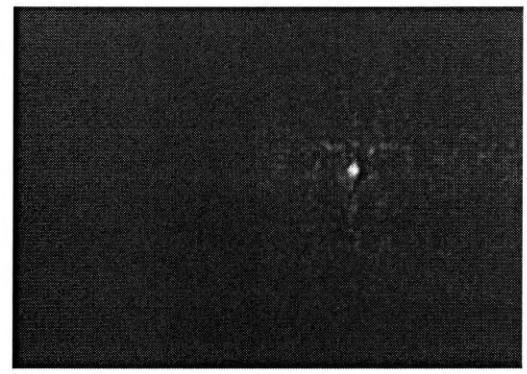

(b)

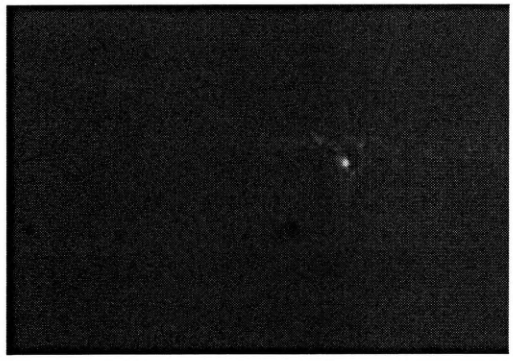

(c)

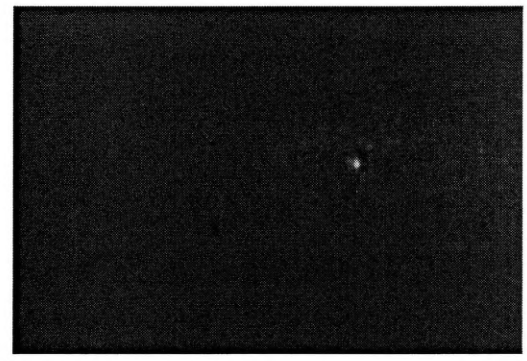

(d)

Fig. 6.9 Experimental results from the incoherent TJTC, (a) the input image, (b) the correlation result from conventional JTC, (c) and (d) the correlation results from the triple JTCs with different filtering functions

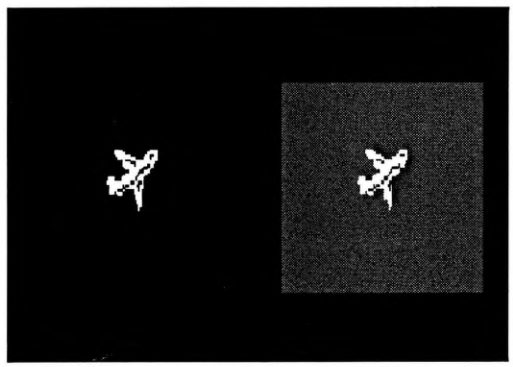

(a)

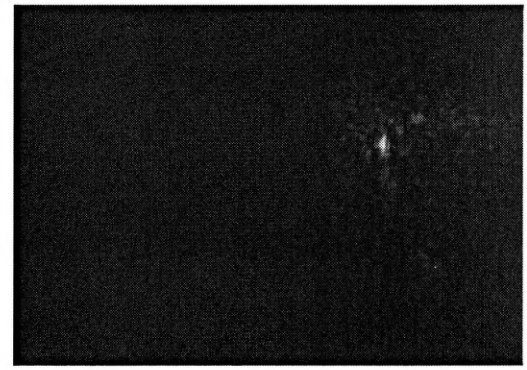

(b)

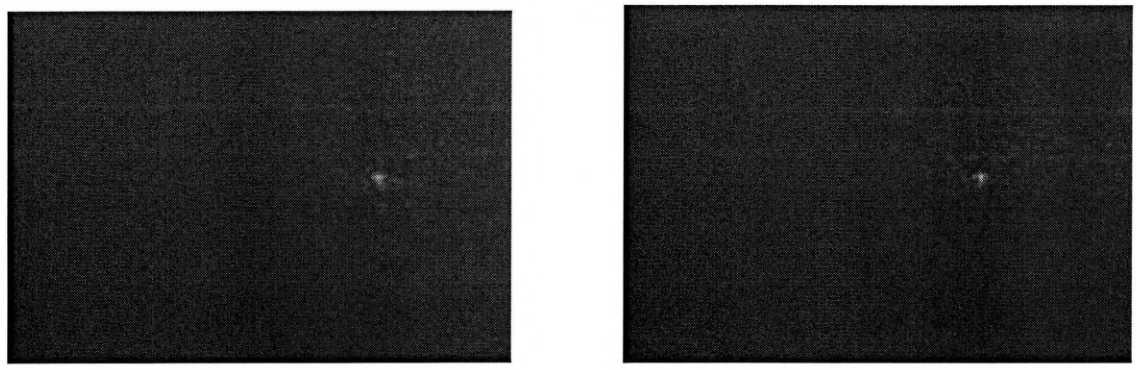

(c) (d)

Fig. 6.10 Experimental results from the coherent TJTC with noisy scene, (a) the input image, (b) the correlation result from conventional JTC, (c) and (d) the correlation results from the triple JTCs with different filtering functions

In this experiment, the incoherent triple joint transform correlator has improved the correlation peak sharpness, which is helpful to avoid false recognition, but meanwhile it has reduced the correlation peak intensity. The performance needs to be improved for pattern recognition application. One important application of incoherent triple joint transform correlation, the wavelet transforms in a photorefractive JTC, will be introduced in Chapter 7.

Chapter 6: References

F. Ahmed, A.S. Awwal and M.A. Karim, "Improved recognition performance with synthetic correlator", Microwave and Opt. Tech. Lett., **14** (1997), 274-278.

M.A. Alam and J.S. Khoury, "Fringe-adjusted incoherent erasure joint transform correlator", Opt. Eng. 37(1), 75-82 (1998).

G. Asimellis, J. Khoury and C. L. Woods, "Experimental demonstration of the holographic in coherent-erasure joint-transform correlator", Opt. Eng. **36** (1997), 2392-2398.

J.L. Horner and P.D. Gianion, "Phase-only matched filtering", Appl. Opt., **23** (1984) 812-816.

J.L. Horner, B. Javidi and J. Wang, "Analysis of the binary phase-only filter", Opt. Comm. **91** (1992), 189-192.

J.L. Horner and J. Leger, "Pattern recognition with binary phase-only filter", Appl. Opt., **24** (1985) 609-611.

B. Javidi and J.L. Horner, "Single spatial light modulator joint transform correlator", Appl. Opt. **28** (1989), 1027-1032.

B. Javidi, "Nonlinear joint power spectrum based optical correlation", Appl. Opt. **28** (1989), 2358-2367.

B. Javidi, J.L. Horner, "Real-time Optical information processing", Academic Press, INC., San Diego (1994).

J. Khoury, J.S. Kane, G. Asimellis, M. Cronin-Golomb and C. Woods, "All-optical nonlinear joint Fourier transform correlator", Appl. Opt. **33** (1994), 8216-8225.

G. Lu, Z. Zhang, S. Wu, and F.T.S. Yu, "Implementation of a non-zero-order joint-transform correlation by use of phase-shifting techniques", Appl. Opt. **36** (1997) 470-483.

G. Lu, F.T.S. Yu, "Performance of a phase-transformed input joint transform correlator", Appl. Opt. **35** (1996), 304-313.

T. Nomura, "Phase-encoded joint transform correlator to reduce the influence of extraneous signal", Appl. Opt. **37** (1998), 3651-3655.

S.k. Rogers, J.D. Cline, M. Kabrisky, "New binarization techniques for joint transform correlation", Opt. Eng. **29** (1990), 1088-1093.

C. Soutar, Z.Q. Wang, C.M. Cartwright and W.A. Gillespie, "Real-time optical intensity correlator using photorefractive BSO and liuiquid crystal television", J. Mod. Opt. **39** (1992), 761-769.

A. Vanderlugt, "Signal detection by complex spatial filtering", IEEE Trans. on Inf. Theory **IT-10**, (1964) 139-145.

J. Wang and B. Javidi, "Multiobject detection using the binary joint transform correlator with different types of thresholding methods", Opt. Eng. **33** (1994), 1793-1805.

S. Vallmitjana, A. Carnicer, E. Martin-Badosa and I. Juvells, "Nonlinear filtering in object and Fourier space in a joint transform optical correlator: Comparison and exprimental realization", Appl. Opt., **34** (1995) 3942-3949.

F.T.S. Yu, "Optical Information Processing", Wiley-Interscience, New York (1983).

H. Zhang, C. Cartwright, M. Ding, and A. Gillespie, A triple joint transform correlator, SPIE **3715**, 185-196 (1999).

S. Zhong, J. Jiang, S. Liu and C. Li, "Binary joint transform correlator based on differential processing of the joint transform power spectrum", Appl. Opt. **36** (1997), 1776-1780.

Chapter 7. Wavelet Transform in a Joint Transform Correlator

The wavelet transform is a subject of interest in optics and other fields. It is superior to the Fourier transform in some aspects. The wavelet transform and its application in the joint transform correlator for various purposes are proposed in this chapter.

7.1 The wavelet transform

As mentioned before, the Fourier transform is the mathematical basis of modern optics. However, the Fourier transform has its own limitations. For example the Fresnel transform has been used, instead of the Fourier transform, if a space-variant optical correlator is required. Another shortcoming is that a truncation of the integration to a finite interval inevitably causes a time-domain resolution problem (Li and Sheng, 1998). To overcome this drawback, modified Fourier transforms, such as the windowed Fourier transform and short-time Fourier transform have been introduced. Among them, a useful transform proposed by Gabor (Li and Sheng, 1998) is defined as

$$G(t,\omega)=\int_{-\infty}^{\infty} f(x)g(x-t)\exp(-j\omega x)dx, \tag{7.1}$$

where f(x) is the original function, g(t) is called the window function. The transform is commonly referred to as the Gabor transform. The real significance of the Gabor transform is that it uses a well-localized Gaussian function g(t) as its window, so that a long duration signal can be analyzed piecewise with fairly good time and frequency resolution. Reconstruction of the original signal from its Gabor transform can be obtained with

$$f(t)=\int_{-\infty}^{\infty}\int_{-\infty}^{\infty} G(\tau,\omega)g(\tau-t)\exp(j\omega\tau)d\tau d\omega \tag{7.2}$$

The Gabor transform has been widely used for signal and image analysis. However, one serious problem with the Gabor transform is for those applications in which spectra are wide but it is difficult to pre-specify the analysis resolution. The wavelet transform was invented to overcome this inconvenience. Although the basic concepts of the wavelet can be traced back to almost a century ago, the work by Daubechies in late 1980's first identified some key mathematical features of the wavelet (Daubechies, 1988). And in 1984, the phrase wavelet transform was officially coined to the locality-oriented multi-solution –based transform.

The wavelet transform allows the decomposition of a one- or two-dimensional signal into a time-frequency or a space-frequency joint representation. The signal to be analyzed is correlated with a bank of functions, called wavelets. Each of the wavelets is derived from an original mother wavelet by means of dilation and shift operations. For the continuous wavelet transform, first select a finite-duration window function $\psi(x)$ to be a mother wavelet, with an admissible condition (Li and Sheng, 1998)

$$C_{\Psi} = \int_0^{\infty} \frac{|\Psi(u)|^2}{u} du < \infty \tag{7.3}$$

where Ψ(u) is the Fourier transform of $\psi(x)$. Any $\psi(x)$ that satisfies this admissibility condition can serve as a mother wavelet. The admissible condition implies that $|\Psi(0)|^2 = 0$ or, in the space domain, $\int_{-\infty}^{\infty} \psi(x)dx = 0$. Thus a qualified wavelet should have a zero mean or should behave like a band-pass filter in the Fourier frequency domain.

A selected mother wavelet can generate a family of daughter wavelets by shifts and dilations, i.e.

$$\psi_{a,b}(x) = \frac{1}{\sqrt{a}}\psi\left(\frac{x-b}{a}\right) \tag{7.4}$$

where the coefficient $1/\sqrt{a}$ is used to equalize the energy contained in each daughter wavelet. With a family of wavelets $\psi_{a,b}(x)$, the continuous wavelet transform is defined as the inner product of the signal and these wavelets,

$$\begin{aligned} WT[f(x)] &= W(a,b) = \left\langle f(x), \psi^*_{a,b}(x) \right\rangle \\ &= \int_{-\infty}^{\infty} \frac{1}{\sqrt{a}}\psi^*\left(\frac{x-b}{a}\right) f(x)dx. \end{aligned} \tag{7.5}$$

In this way, the features corresponding to different frequency spectra can be extracted. To make sure there is no information loss in this transform, the signal reconstruction or the inverse wavelet transform can be defined as:

$$\begin{aligned} WT^{-1}[W(a,b)] &= f(x) \\ &= \frac{1}{C_\Psi}\int_{-\infty}^{\infty}\int_{-\infty}^{\infty} W(a,b)\Psi_{a,b}(x)\frac{dadb}{a^2} \end{aligned} \tag{7.6}$$

The wavelet transform has been shown to be useful in many areas including pattern recognition. The wavelet transform can be thought of as a correlation between a wavelet and an input signal. The 2-D wavelet transform of an image f (x, y) can be written as:

$$W_f(a,b;x,y) = f(x,y) * \psi_{ab}(x,y) = \iint f(x,y)\psi^*_{ab}(x,y)dxdy \tag{7.7}$$

Wavelets are generated from a mother wavelet function $\psi(x,y)$ as follows

$$\psi_{ab}(x,y) = \frac{1}{a}\psi\left(\frac{x-b_x}{a}, \frac{y-b_x}{a}\right) \tag{7.8}$$

where a is the scale parameter and b = (b_x, b_y) the shift parameter. The wavelet transform in the frequency domain is

$$W_f(a,b;x,y) = \int_{-\infty}^{\infty}\int_{-\infty}^{\infty} F(u,v)\Psi^*(au,av)\exp[2\pi i(b_x u + b_y v)]dxdy \qquad (7.9)$$

where a capital letter indicates a Fourier transformation. The factor $\Psi^*(au,av)$ can be interpreted as a frequency filter and implemented in an optical correlator. Because a wavelet can be thought of as a band-pass filter, an image can be viewed in a particular scale or frequency band after cross-correlation with wavelet. The cross-correlation result is an image corresponding to the frequency band of the wavelet. When the scale parameters varies, the filter is reduced or dilated, so it is possible to work in different zones of the frequency spectrum of the image f (x, y).

7.2 Image feature extraction with wavelet filters

The wavelet transform is superior to Fourier analysis for feature extraction, such as edges, corners, and other local features of the image. Among all the features, edges are often the most informative features of an image. One can enhance the high-frequency components in the Fourier plane to obtain edges and derivatives of the image. However, the high-pass filters are sensitive to noise (Li, 1996). Image singularity can be not only detected but also characterised by the multiscale wavelet transform. Because a wavelet can be thought of as a bandpass filter, an image can be therefore viewed in a particular scale or frequency band after cross-correlation with a wavelet.

Unlike the Fourier transform, the kernel of the wavelet transform is not unique. The choice of a transform kernel is highly dependent on the application. The Haar's wavelet was commonly used in early wavelet applications. It is a bipolar step function in one dimension:

$$h(t)=\begin{cases}1 & 0\le t\le 1/2\\ -1 & 1/2\le t\le 1\\ 0 & other\end{cases} \tag{7.10}$$

The Haar's wavelet is easy to represent with binary electro-optic devices because of its bipolar character, and it is very useful as an edge and corner detector.

The 2-dimensional Haar's wavelets are often used to detect corners, horizontal edges, and vertical edges of a 2-D image. For clearer expression, the 2-D Haar's wavelet can be written as an operator (Wang, 1995):

$$h(x,y)=\begin{vmatrix}1 & -1\\ -1 & 1\end{vmatrix} \tag{7.11}$$

It is known as an effective corner detector. From this, the horizontal and vertical edge detectors can be separated:

$$Haar_h=\begin{vmatrix}1\\ -1\end{vmatrix} \qquad Haar_v=\begin{vmatrix}1 & -1\end{vmatrix} \tag{7.12}$$

where $Haar_h$ and $Haar_v$ represent the horizontal edge and vertical edge wavelet. The Haar's wavelet transform is the convolution of an image with these operators of different sizes. Here the feature-extraction processing in an optical correlator is simulated with the software IDL. The wavelet functions are calculated and then the operation of optical correlation is simulated to obtain the output signals. The target object selected is the English letter 'H'. Fig. 7.1 shows the simulation results of the Haar's wavelets with letter H, (a) the object letter 'H', (b) the correlation result of the corner filter with the letter 'H', (c) and (d) are the correlation results with $Haar_h$ and $Haar_v$, respectively. It is shown that the corners, horizontal edges and vertical edges of the target have been extracted.

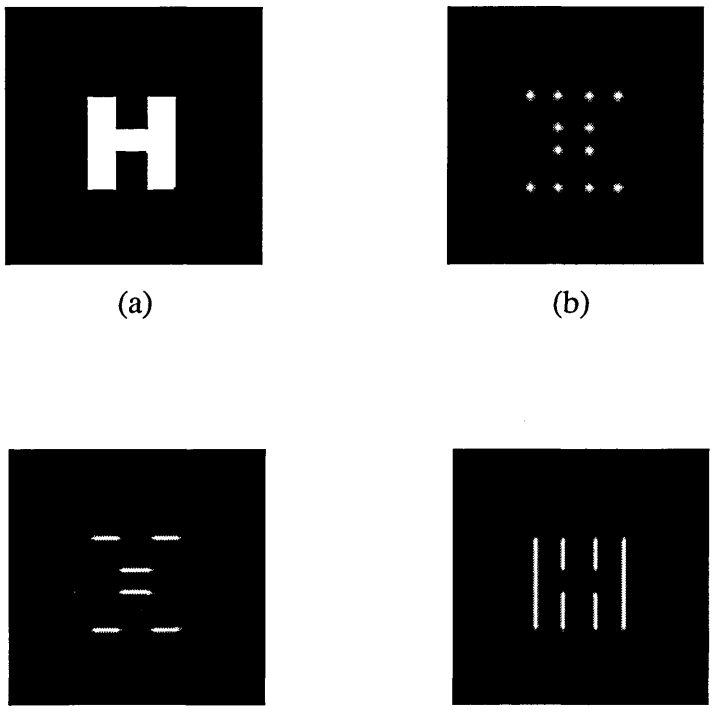

(a) (b)

(c) (d)

Fig. 7.1 Computer simulation results of the Haar's wavelets, (a) the target image letter 'H', (b) the correlation result with Haar's corner wavelet, (c) with Haar's horizontal edge wavelet, and (d) with Haar's vertical wavelets.

One important aspect in image processing is to detect the abrupt change of the gray scale and reveal the edge of the image. The operator $Haar_h$ and $Haar_v$ are designed only for two special orientations. If we need to sharpen the whole edge of an image, we can filter the image in two orthogonal directions separately, then combine the results by vector computing. The Roberts gradient is well known as an edge detector. It is performed by convolving an image with two 2×2 kernels to approximate the horizontal and the vertical strength of the edge at each pixel location (Wang, 1995):

$$R_+ = \begin{vmatrix} 1 & 0 \\ 0 & -1 \end{vmatrix}, \qquad R_- = \begin{vmatrix} 0 & 1 \\ -1 & 0 \end{vmatrix} \tag{7.13}$$

Both of them can possibly be used for edge enhancement. Fig. 7.2 shows the computer simulation results of the letter 'H' and an aircraft with the Roberts gradient, (a) the

original image airplane, (c), (d), (e) and (f) edge-enhanced images with different Roberts filters. It is apparent that the edge of the object image has been extracted.

(a)

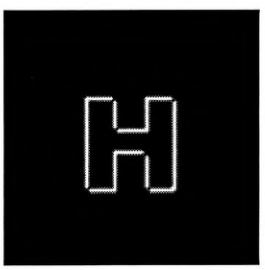

(b)

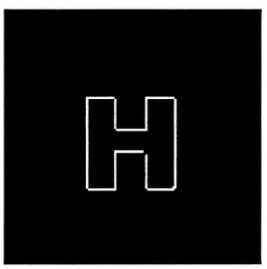

(c)

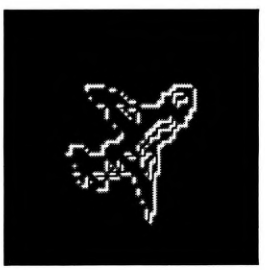

(d)

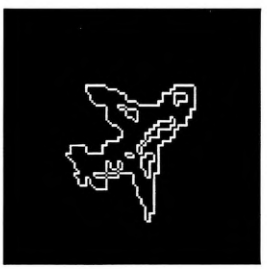

(e)

Fig. 7.2 The simulation results of the Roberts gradient, (a) the target object airplane, (b) and (c) the correlation results of the letter 'H' with the Roberts gradients of different sizes, (d) and (e) are the correlation results of the (a) with the Roberts gradients of different sizes.

The next filter used in simulation is the Mexican-hat wavelet with different scaling factors. The 2-D mother Mexican-hat wavelet can be expressed as (Alam, 1999):

$$h(x,y) = \left[1-(x^2+y^2)\right]\exp\left(-\frac{x^2+y^2}{2}\right) \tag{7.14}$$

with the scaling factor a, the daughter wavelet is

$$h_a(x,y) = \frac{1}{a}h\left[\frac{x}{a},\frac{y}{a}\right] \tag{7.15}$$

The simulation results are shown in fig. 7.3, (a) is the correlation with dilation = 4, and (b) is the result with dilation = 3. It is shown that the Mexican-hat wavelets have blocked some parts of the image and enhanced other parts, if the enhanced parts are important for identifying the image, the discrimination ability of an optical correlator should be improved by employing the Mexican-hat wavelet into the optical implementation.

(a) (b)

Fig. 7.3, (a) is the correlation with dilation = 4, and (b) is the result with dilation = 3.

7.3 Photorefractive JTC with Wavelet transforms

In the field of pattern recognition, the wavelet transform is not only known as an effective tool for feature extraction, but the wavelet transform filters have also been used to modify the correlation profiles of optical correlators. Lu et al. showed the possibility of wavelet transforms incorporated in a JTC to enhance the discrimination ability (Lu, 1992). A photorefractive JTC with wavelet filters has been reported by R. Tripathi et al. (Tripathi,1997), in which a photorefractive $BaTiO_3$ crystal has been used as the recording medium to distinguish between two nearly similar input patterns. Li et al. have shown that with a bandpass wavelet filter in the Fourier plane, a JTC could perform the correlation between the wavelet transforms of two images (Li, 1996).

In this section, a real-time photorefractive joint transform correlator with wavelet transform filters is presented to improve the correlation performance. The Mexican-hat wavelets are used in the correlator in the frequency domain, instead of in the space domain as the Mexican-hat wavelet functions have negative values in space domain but have positive Fourier spectra. The experiments were implemented with a liquid crystal television (LCTV) as the spatial light modulator (SLM). In the Fourier plane, a photorefractive crystal BSO is used as the dynamic holographic medium. Compared with $BaTiO_3$, BSO responds to optical stimulation rather faster, so it is a good choice for nonlinearly recording the joint power spectrum (JPS) to realize the real-time holographic writing and reading. The signal-to-noise ratio, discrimination ability and noise robustness of the wavelet transform JTC are compared with the conventional JTC.

As shown in chapter 5, the joint power spectrum in the frequency plane of a JTC is

$$\begin{aligned} I(p,q) &= \left|R(p,q)+S(p,q)\right|^2 \\ &= R(p,q)R^*(p,q)+S(p,q)S^*(p,q)+R^*(p,q)S(p,q)\exp(j2x_0p) \\ &\quad +R(p,q)S^*(p,q)\exp(-j2x_0p) \end{aligned} \tag{7.16}$$

where $R(p,q)=|R(p,q)|\exp[j(\varphi_R(p,q)]$ and $S(p,q)=|S(p,q)|\exp[j(\varphi_S(p,q)]$ are the Fourier transforms of the reference and the scene.

Theoretically, the result should be the same when a wavelet function is introduced into a JTC in either the object space domain or in the spatial frequency domain. However, because of its admissible condition, the original wavelet functions should have zero mean, which leads to the requirements of registering negative values and, perhaps, also phase information in the input plane. On the other hand, many wavelet functions, such as the Mexican-hat wavelet and Gaussian wavelet, have only positive spectra in the frequency domain and, furthermore, after suitable binarization processing, some of these spectra may have only several discrete values. This shows that these functions can be easily implemented with an amplitude modulated spatial light modulator as well as by computer-generated holography methods. In this way, the wavelet transform of an image can be realized more conveniently in the frequency domain.

After filtering with a wavelet transform function in the Fourier domain, the reference and object spectra become $R'(p,q)=R(p,q)H^*(p,q)$ and $S'(p,q)=S(p,q)H^*(p,q)$, and then the joint power spectrum is

$$\begin{aligned} I'(p,q) &= |R'(p,q)+S'(p,q)|^2 \\ &= R'(p,q)R'^*(p,q)+S'(p,q)S'^*(p,q)+R'^*(p,q)S'(p,q)\exp(j2x_0p) \\ &+ R'(p,q)S'^*(p,q)\exp(-j2x_0p) \end{aligned} \tag{7.17}$$

By choosing the right wavelet functions and the right scaling factors, suitable frequency parts of the original images can be extracted, and therefore, sharper correlation peaks, higher discrimination and higher noise robustness can be obtained.

7.3.1 The experimental set-up

In our experiment, a couple of 2-D Mexican-hat wavelets with different dilation factors have been used as spatial filters. It is a function with rotational symmetry. The mother Mexican-hat wavelet is the second derivative of the Gaussian function

$$h(x,y)=\left[1-(x^2+y^2)\right]\exp\left(-\frac{x^2+y^2}{2}\right) \tag{7.18}$$

It is even and real, and the wavelet admissible condition is satisfied. The Fourier transform of the Mexican-hat wavelet is

$$H(p,q)=4\pi^2(p^2+q^2)\exp\left[-2\pi(p^2+q^2)\right] \tag{7.19}$$

with the dilation factor a, the Fourier spectrum is

$$H_a(p,q)=4\pi^2a^2(p^2+q^2)\exp\left[-2\pi a^2(p^2+q^2)\right] \tag{7.20}$$

$\left|H_a(p,q)\right|^2$ is the filter inserted in the Fourier domain. $\left|H(p,q)\right|$ is proportional to $\left|H(p,q)\right|^2$ for the binarized Mexican-Hat as it is even and real valued. By varying the factor a, different bandpass operations can be obtained.

The experimental set-up is shown in Fig. 7.4. The argon ion laser beam is expanded and collimated to 42mm in diameter. The beam intensity can be adjusted by rotating a half-wave plate. L1 is the first Fourier transform lens. Input images of 768 x 512 pixels are generated by a frame grabber and scaled to ensure the correct registration of pixel on the LCTV. The angles of polariser (P) and analyser (A) are chosen to operate LCTV in amplitude-mostly modulation. The distance between the reference and target gives a fringe spacing of 12.4 μm, which ensures that the cross-correlation signal is adequately

separated from the dc part. The Fourier transform is formed at the BSO crystal which is positioned at the back focal plane of the lens L1. For the read-out part, He-Ne laser light is expanded and collimated so that the joint power spectrum grating can be addressed. The wavelet functions are displayed at IP1 filtering the JPS. The correlation output is formed by lens L2, and an interference filter IF and a polaroid P1 are used to suppress the background noise. The output correlation signal is detected by a CCD camera positioned at the back focal plane of the transform lens L2 and linked to the same frame grabber. These correlation images are captured by a microcomputer and then are processed with the IDL software.

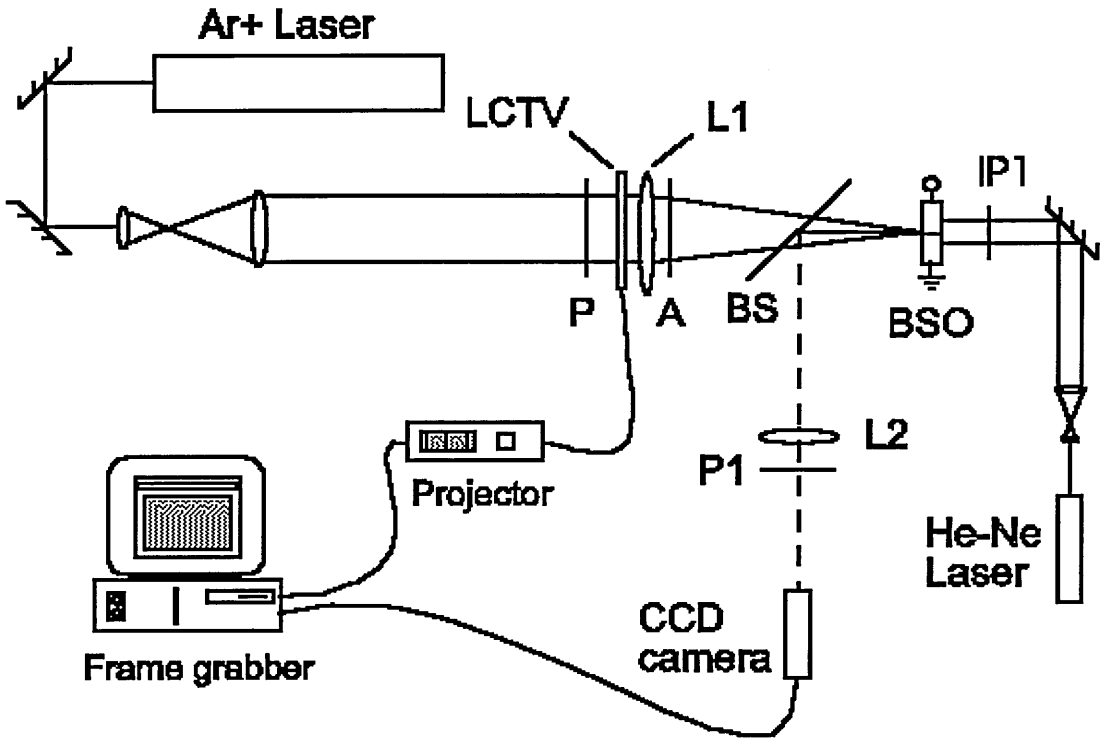

Fig. 7.4 The experimental set-up

7.3.2 Experimental results and discussions

Three 768×512images have been used in the experiment, for testing the signal-to-noise (SNR) ratio, which is defined as the rate of the peak correlation intensity to the

mean intensity outside 50% of the peak value, the noise robustness and discrimination ability, respectively. In Fig.7.5, 7.6 and 7.7, (a) is the JTC input scene, (b) is the correlation output with conventional JTC, (c), (d) and (e) are the correlation output with wavelet JTC of different dilation factors.

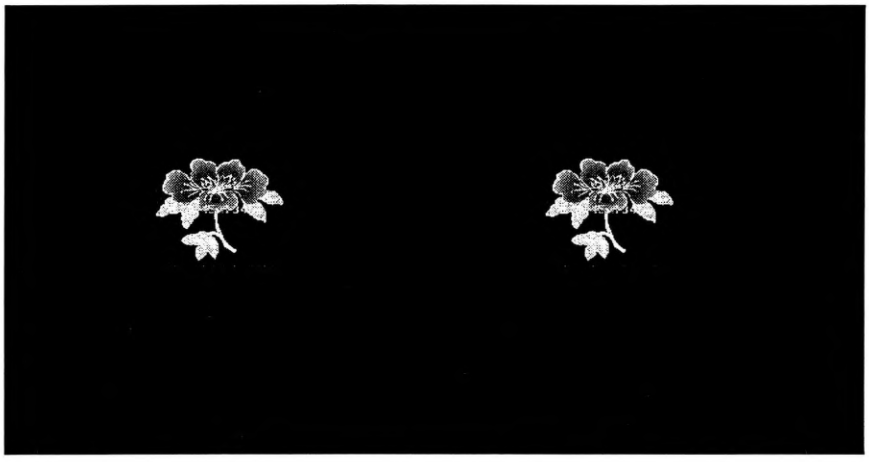

(a)

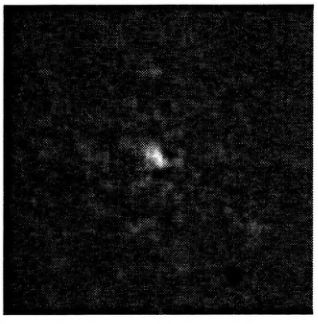

(b)

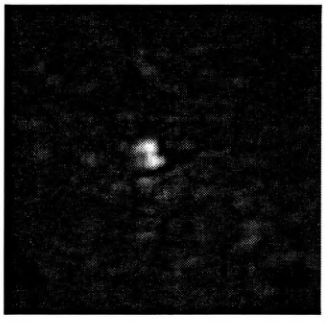

(c)

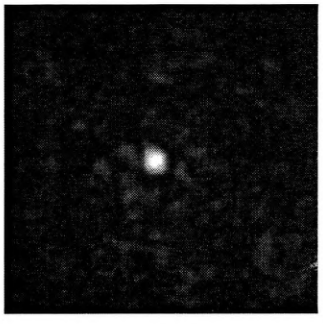

(d)

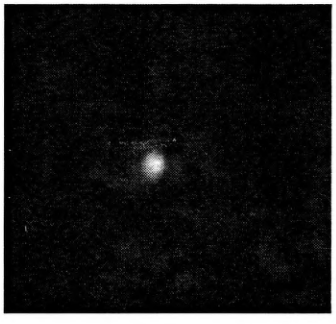

(e)

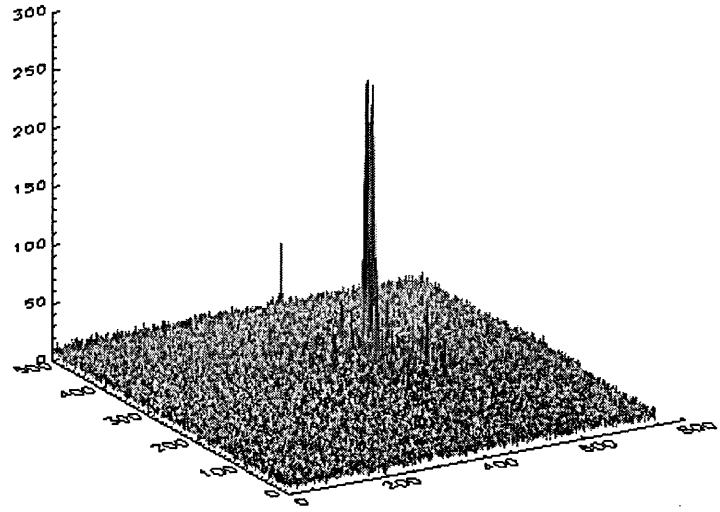

(f)

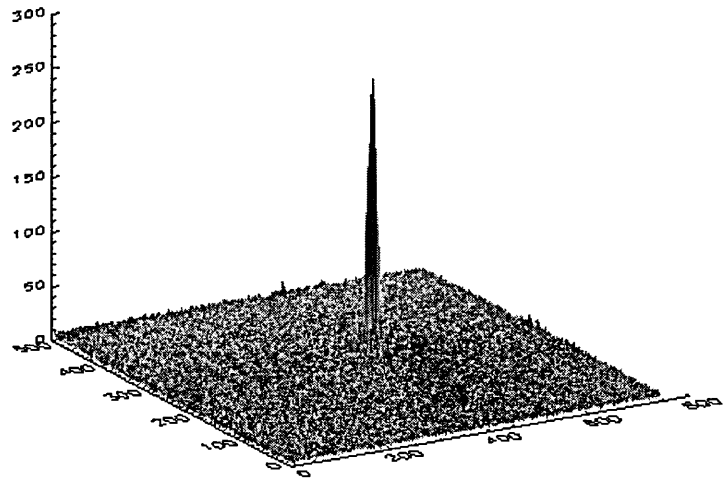

(g)

Fig. 7.5 The experimental results with a single object, noise-free scene, (a) the input scene; (b) the correlation output with a conventional JTC; (c), (d) and (e) the correlation output of a wavelet transform JTC with different dilation factors, (f) three dimensional plot of (b), and (g) three dimensional plot of (d).

The input image of fig. 7.5 is a single object flower with gray levels. With this image in the JTC, there are some side lobes around the peak, and it seems that they can not be eliminated by adjusting the set-up. However, with wavelet filters at the frequency plane, the noise can be reduced. The amount of reduction depends on the dilation factor chosen to build the filter. The SNR for the output plane of the conventional JTC is15:1, and those of the wavelet JTC are 17:1 (for a = 1.5), 19:1 (for a = 2.0) and 13:1 (for a = 2.5). From these numerical results, it is obvious that the SNR can be improved with suitable scaled wavelet filters. However, when the dilation factor is too large, the peak correlation intensity decreases a lot, this may even lead to a decrease of SNR (as shown in fig.3(a)). There is a trade-off between PCI and SNR, an effective wavelet filter should be the one which can achieve a high SNR without much loss of peak correlation intensity. For a clearer comparison, three dimensional plots of the entire correlation plane (768 x 512) of fig. 7.5 (b) and (d) are presented in fig.7.5 (f) and (g), respectively. It is clear that a sharper correlation peak and suppression of the side lobes have been obtained.

In general, signals are localized but noise is global (Li and Sheng, 1998). The wavelet transform gives a chance to match on a local signal basis and suffer less noise disturbance. Fig. 7.6 shows the correlation results of a single input object, an aircraft with random background noise. (b) is the output plane of the conventional JTC, (c) , (d) and (e) are the output planes of wavelet JTC with dilation factors 1.5, 2.0, and 2.5, respectively. It is obvious that the noise level has reduced along with the increase of the dilation factor. This is a little different from the result obtained from the noise free scene (see the last paragraph). In fact, the SNR from the images (b), (c), (d) and (e) are 7.4, 7.8, 9.2, and 10.4. A possible explanation is that the wavelet with suitable large dilation factors are more effective for depressing background noise than sharpening correlation peaks.

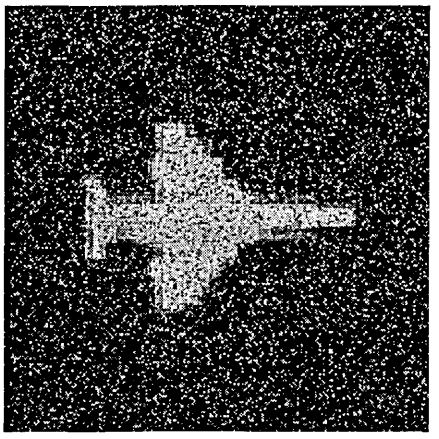

(a)

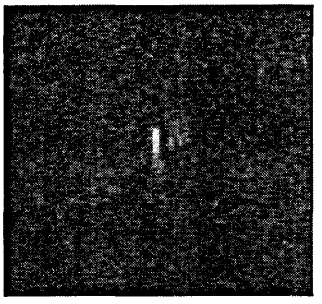

(b)

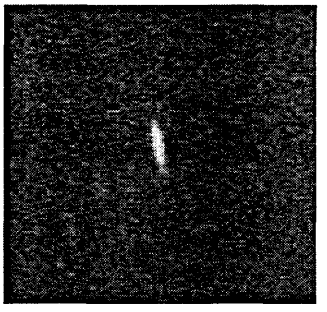

(c)

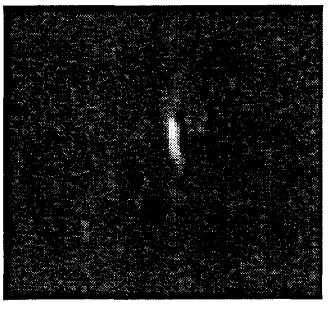

(d)

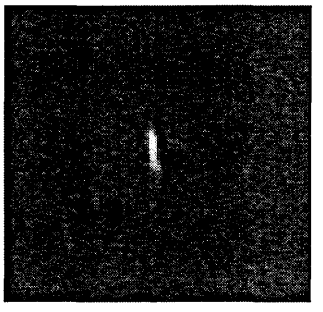

(e)

Fig. 7.6 The experimental results with a noisy scene (a) the input scene; (b) the correlation output with a conventional JTC; (c), (d) and (e) the correlation output of a wavelet transform JTC with different dilation factors.

Fig. 7.7 deals with the situation of multiple objects at the input scene. Three shapes star, circle and rectangle are in the scene. Fig. 7.7 (b) is the correlation output of the conventional JTC, the ratio of the first cross-correlation intensity (star with circle) I_2 and the auto-correlation peak intensity (star with star) I_1 is 0.8, and the ratio of the second cross-correlation peak intensity (star with rectangle) I_3 to I_1 is 0.59. After involving the wavelets, I_2/I_1 becomes 0.51, 0.45 and 0.40, and I_3/I_1 becomes 0.33, 0.24 and 0.13, corresponding to three different dilation factors respectively. No doubt, the cross-correlation peaks have been suppressed, which means higher discrimination has been obtained. However, the same problem occurs as in fig. 7.5. As the dilation factor increased, the auto-correlation peak also reduced a lot. The consequence is, after scaling the correlation planes, the background noise level is relatively high. In fig.7.5 (e), the output plane looks quite noisy. Table 7.1 summarizes the numerical results of fig. 7.5, 7.6 and 7.7, a is the dilation factor and the PCI, SNR and PSR are defined in 6.2.

	Filter	a	PCI	SNR	PSR
Fig.7.5	Conventional		185	15	
	Wavelet_1	1.5	166	17	
	Wavelet_2	2.0	168	19	
	Wavelet_3	2.5	151	13	
Fig.7.6	Conventional		164	7.4	
	Wavelet_1	1.5	152	7.8	
	Wavelet_2	2.0	152	9.2	
	Wavelet_3	2.5	147	10.4	
Fig.7.7	Conventional		205		0.8
	Wavelet_1	1.5	179		0.51
	Wavelet_2	2.0	172		0.45
	Wavelet_3	2.5	156		0.40

Table 7.1 Summary table of the results in fig. 7.5, 7.6 and 7.7.

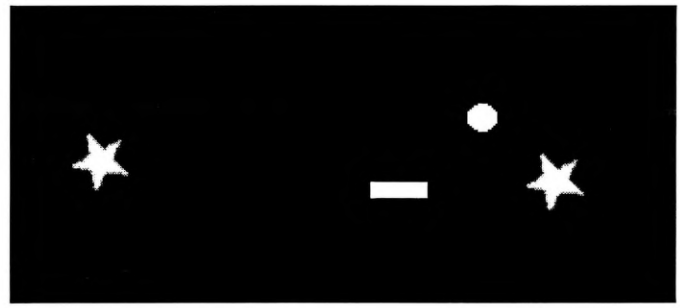

(a)

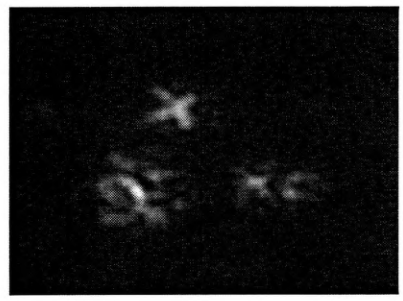

(b)

(c)

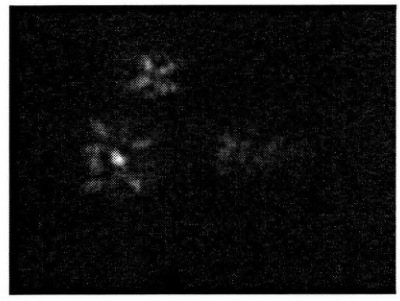

(d)

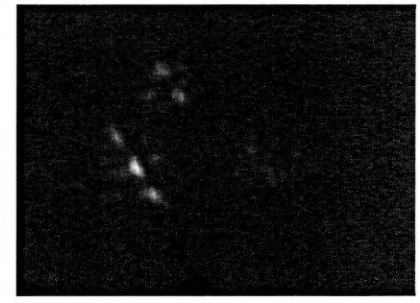

(e)

Fig. 7.7 The correlation results with multiple objects, (a) the input plane; (b) the correlation output with a conventional JTC; (c), (d) and (e) the correlation output of a wavelet transform JTC with different dilation factors.

7.4 Image feature extraction in a photorefractive joint wavelet transform correlator

7.4.1 Computer Simulations

Prior to experimental implementation, the feature-extraction processing was simulated. We calculated the wavelet functions and encoded them as images with only positive values, as discussed in section 5.3. Then we simulated the operation of joint transform correlation to obtain the output signals. The target object selected is the English letter 'T'. Haar's wavelet, Robert's gradient and Mexican-hat wavelets with different scaling factors have been used in the simulation.

Fig. 7.8 shows the simulation results, (a) the encoded Haar's wavelet filter, (b) the object letter 'T', (c) the correlation result of the encoded filter with the letter 'T', (d) and (e) are the correlation results with $Haar_h$ and $Haar_v$, respectively. It is shown that the corners, horizontal edges and vertical edges of the target have been extracted.

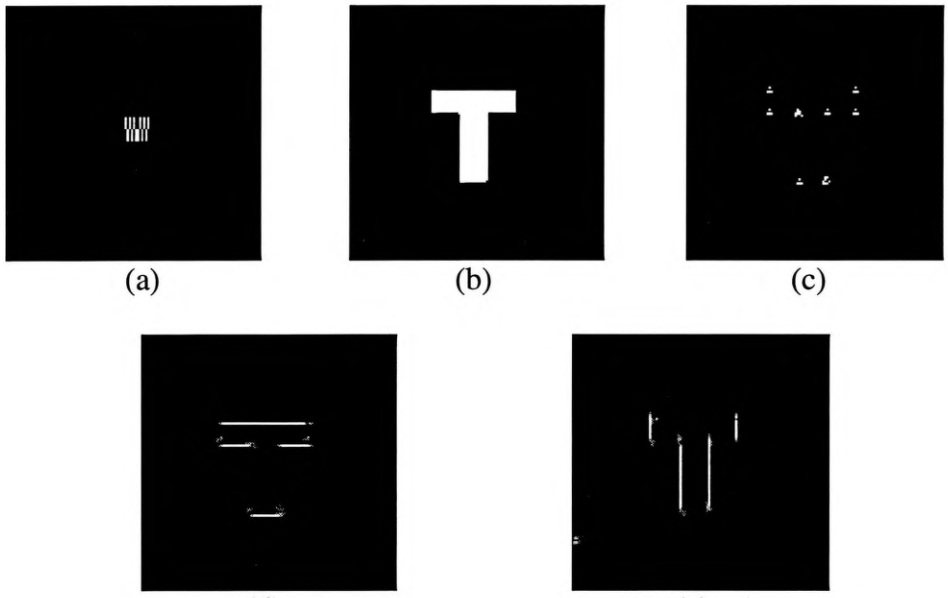

Fig. 7.8 Computer simulation results with Haar's wavelet: (a) Encoded Haar's wavelet, (b) the object letter T, (c) the correlation result of the letter 'T' with the encoded Haar's wavelet, (d) correlation result with the encoded horizontal Haar's wavelet, and (e) the correlation result with vertical Haar's wavelet.

Fig.7.9 shows (a) the encoded 2 x 2 Roberts gradient and (b) the correlation result of the letter 'T' with Roberts gradient. It is apparent that the edge of the object image has been extracted.

(a) (b)

Fig. 7.9 Computer simulation result with Roberts gradient: (a) the encoded Roberts gradient, and (b) the correlation result of the letter 'T' with Roberts gradient.

The last filter used in simulation is Mexican-hat wavelet with different scaling factors. The simulation results are shown in fig. 7.10, (a) is the encoded Mexican-hat wavelet, (b) is the correlation with dilation = 2.8, and (c) is the result with dilation = 3.5.

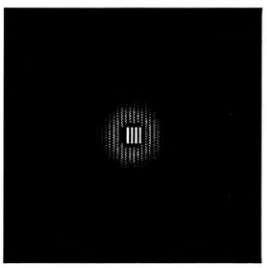

(a)

(b) (c)

Fig. 7.10 Computer simulation results with Mexican-hat wavelet: (a) the encoded Mexican-hat wavelet, (b) and (c) are the correlation results with Mexican-hat wavelet functions with dilation factors of 2.8 and 3.5, respectively.

7.4.2 The optical experimental for image feature extraction

The experimental set-up of the photorefractive joint transform correlator is shown in fig. 5.2. The wavelet filters and the target images are displayed side by side in the input plane IP for image feature extraction.

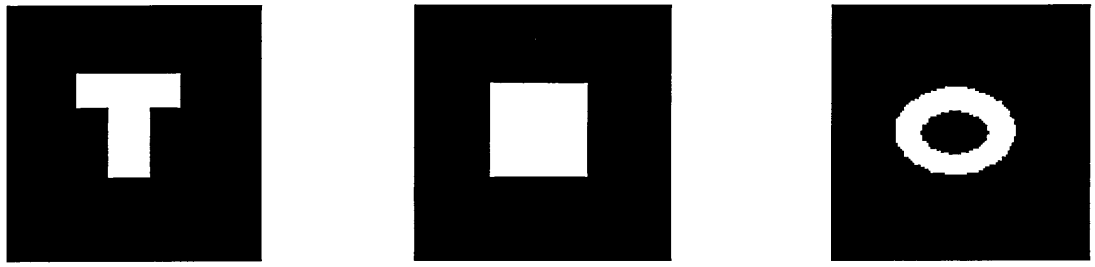

(a) (b) (c)

Fig. 7.11 Three input images used in the experiment, (a) the letter 'T', (b) a square and (c) an oval ring.

Fig. 7.11 displays several input images used in the experiment, (a) the letter 'T', (b) a square, and (c) an oval ring. Firstly, the encoded Haar's wavelet filter and the square are displayed in the input plane of the correlator. Fig. 7.12 (a) shows the correlation result, it is quite clear that the four corners of the square have been picked out. The results of the wavelet $Haar_h$ and $Haar_v$ are shown in (b) and (c) respectively. They extract the horizontal and vertical edges.

Fig. 7.13 shows the experimental results of the letter 'T' correlating with the Mexican-hat wavelet with two different scaling factors, (a) a = 2.8 and (b) a = 3.5.

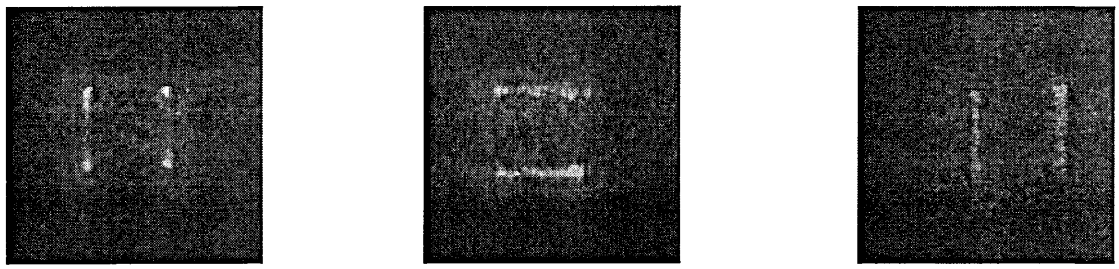

(a) (b) (c)

Fig. 7.12 The experimental results of the square correlating with (a) Haar's wavelet, (b) the horizontal Haar's wavelet, and (c) the vertical Haar's wavelet.

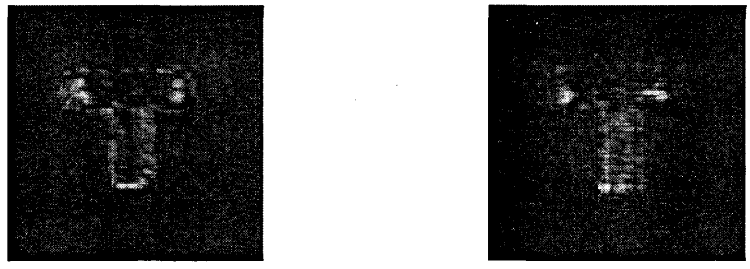

(a) (b)

Fig. 7.13 The experimental results of the letter 'T' correlating with Mexican-hat wavelet with dilation factors of, (a) 2.8 and (b) 3.5.

Finally, because edges are often the most important feature of an image, we used all three different images in the experiment with the Roberts gradient. Fig. 7.14 shows the correlation results of the Roberts gradient filter correlating with (a) the English letter 'T', (b) the square and (c) the oval ring. It is obvious that this filter can be used to extract edges formed by either lines or curves. To show the edge-enhanced effects more clearly, the horizontal cross-sections of fig. 7.12 (b), and fig. 7.14 (b) are shown in fig. 7.15 (a) and (b), respectively. By comparing the original image and the edge-enhanced reconstruction, it shows that the edge-extraction operation with encoded Roberts gradient is quite effective in a photorefractive JTC.

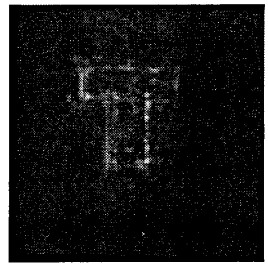

(a)

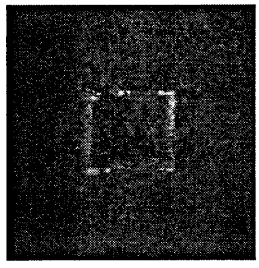

(b)

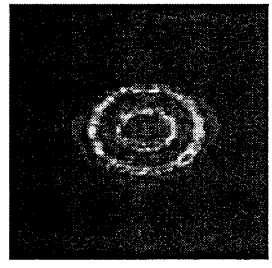

(c)

Fig. 7.14 The experimental results of the encoded Roberts gradient with (a) the shape square, (b) the letter T, and (c) the oval ring.

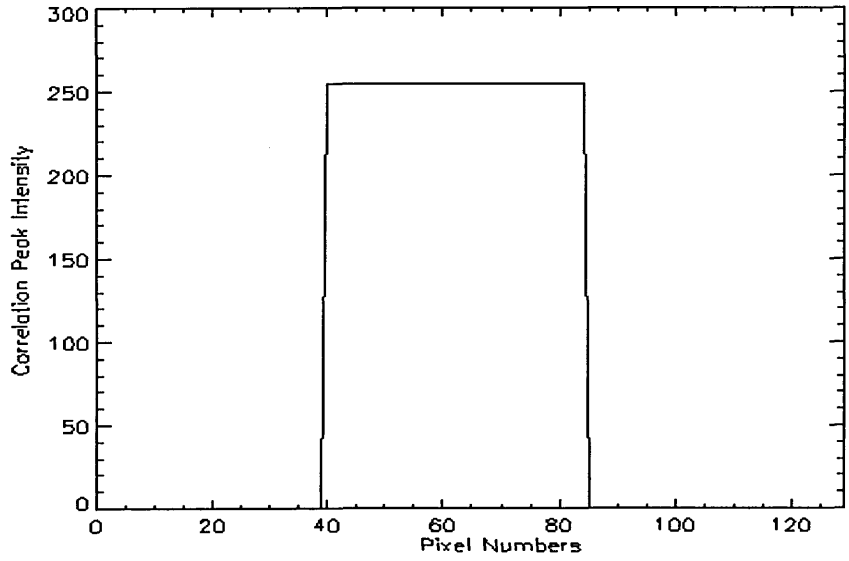

(a)

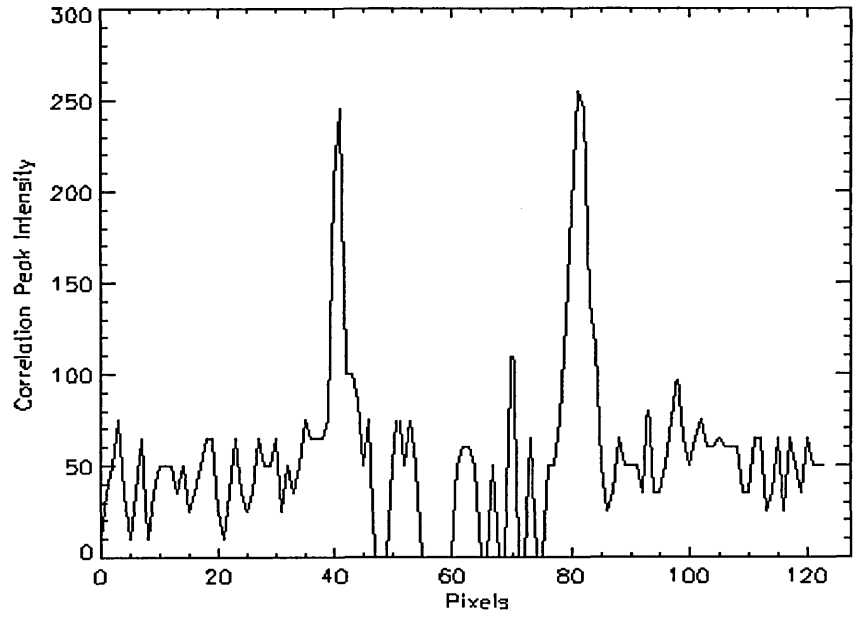

(b)

Fig. 7.15 The horizontal cross-sections of, (a) fig. 7.11(b), and (b) fig.7.14 (b).

In this section, we have demonstrated a photorefractive joint transform correlator with various wavelet filters to extract different kinds of features of images. Both computer simulation and experimental results have shown that these encoded wavelet filters work effectively in the photorefractive JTC with the purpose of extracting different local features of images.

Chapter 7: Reference

M.S. Alam, "Wavelet based joint transform correlation", Proceedings of the SPIE, 3715, 236-247, Orlando, 1999.

N. J. Cook, A. Carnicer, S. Vallmitjana, I. Juvells, C.M. Cartwright, and W.A. Gillespie, "Implementation of a photorefractive binary joint transform correlator" J. Opt. Soc. Am. B. **15**(7), 1977-1984 (1998).

P. S. Erbach, D. A. Gregory and X. Yang, "Optical wavelet transform by the phase-only joint-transform correlator", Appl. Opt. **35**(17), 3117-3126 (1996).

S.P. Kozaitis and M.A. Getbehead, " Multiple-input joint transform correlator for wavelet feature extraction", Opt. Eng. **37**(4) 1325-1331 (1998).

Y. Li, and Y. Sheng, Optical pattern recognition (Eds. Yu, Jutamulia), Cambridge University Press, Cambridge, 1998 (Chapter 3).

J. Li, Y. Zhang and J. Hu, "Object recognition with a wavelet-transform-based joint transform correlator", Opt. Eng. **35**(3) 775-777 (1996).

X.J. Lu, A. Katz, E.G. Kanterakis and N.P. Caviris, "Joint transform correlator that uses wavelet transforms," Opt. Lett. **17**, 1700-1702 (1992).

R.A. Maestre, J. Carcia and C. Ferreira, "Pattern recognition using sequential matched filtering of wavelet coefficients", Opt. Comm. **133**. 401-414 (1997).

I. Daubechies, Comm. Pure Appl. Math. 41, 909-996 (1988).

D. Roberge, and Y. Sheng, "Optical composite wavelet-matched filter", Opt. Eng. **33**(7), 2290-2295 (1994).

Y. Sheng, D. Roberge, and H.H. Szu, "Optical wavelet transform", Opt. Eng. **31**(9), 1840-1845 (1992).

R. Tripathi, J. Joseph, and K. Singh, " Pattern discrimination using wavelet filters in a photorefractive joint-transform correlator", Optics Comm. **143**, 5-10 (1997).

R. Tripathi and K. Singh, "Pattern discrimination using a bank of wavelet filters in a joint transform correlator", Opt. Eng. **37**(2), 532-538 (1998).

D. Gabor, Proc. Inst. Electr. Eng. 93, 429-457 (1946).

W. Wang, G. Jin, Y. Yan, and M. Wu, "Joint wavelet-transform correlator for image feature extraction", Appl. Opt. **34**(2), 370-376 (1995).

C. S. Weaver and J. W. Goodman, "Technique for optically convolving two functions," Appl. Opt. **5**, 1248-1249 (1966).

Y. Yang, " Optical joint transform correlator for automatic target recognition", J. Optics (Paris), **27**(1), 3-11 (1996).

Chapter 8 Rotationally Invariant Photorefractive Joint Transform Correlator

8.1 The Photorefractive JTC with Circular harmonic Filters

The joint transform correlator has proved to be a useful tool for pattern recognition. Compared with spatial-filter-based correlators, JTC is less sensitive to system alignment and is well suited to real-time processing. However, just like traditional correlators, the performance of the JTC degrades under distortions such as change of scale and orientation. It is well known that rotational invariance can be achieved by the use of circular-harmonic filters (CHF), but the use of CHF has been limited since the consequences of full rotational invariance would be highly reduced light efficiency and low discrimination because any circular harmonic component (CHC) contains only part of the spatial information of the object. For the photorefractive JTC, the situation is even worse. Very few papers have reported a JTC implementation with both photorefractive recording materials and CHFs, probably because the large difference in the light transmission of the reference and scene images in the input plane causes low fringe modulation in the Fourier plane and hence degrades the quality of the output correlation signal. Obviously, more than one CHC can be combined to construct a filter, which will contain more information from the target and result in higher light transmission and energy efficiency, but full rotational invariance is usually lost with multiple CHCs (Chang, 1997).

The phase only filter (POF) (Horner, 1984) is well known for its high discrimination and high optical efficiency. However there are still some problems of utilising a circular harmonic POF in a JTC. Firstly, for a real-time photorefractive JTC, it is necessary to encode a circular harmonic POF to a non-negative reference image before it is displayed, and secondly, with a circular harmonic phase only filter at the input plane of JTC, the

light transmission of reference image is even worse than matched-filter-based CHFs. As a result of the lower modulation in the Fourier plane the correlation output is even poorer.

In our work, in order to improve the light transmission of the references, we used the 'IDL' software to scale both the matched filter and phase only filter before display at the joint input plane. The experimental results from the circular harmonic JTC and circular harmonic phase only JTC are compared for several single circular harmonic components. After that we used a multiple CHF in a JTC to follow the track of an aircraft with rotations within ±90. The experiments are implemented with a liquid crystal television as the third input image and, at the Fourier plane, a BSO crystal is used as the dynamic holography medium, which records the JPS nonlinearly to realize real-time holographic writing and reading and also, under the condition of large modulation, can produce approximate quantizing process.

8.2 Experimental Comparison of CHF and Phase-only CHF in a JTC

The reference object selected is the English letter E, chosen for its lack of circular symmetry. The zero order and the second order circular harmonic components were used in turn to form either the matched filters or the phase only filters. The performance criteria used were the peak correlation intensity, PCI , (with a scaling of 0-255) and the signal-to-noise ratio, SNR, which is defined as the ratio of the peak correlation intensity to the mean intensity outside the 50% peak value in the correlation plane and as such represents the sharpness of the correlation peak and consequently determines the probability of an error in detection.

The experimental set-up is shown in Fig. 5.3. Input images of 768 x 512 pixels are generated by a frame grabber and scaled to ensure the correct registration of pixels on the LCTV. The scene and the circular harmonic filters are displayed side by side in the input plane P1. In order to increase the fringe modulation in the Fourier Plane, the 'IDL'

software was used to scale the filters to enhance their transmitted energy. Since negative values are not appropriate for an image displayed on an amplitude modulator, the phase only filters have been encoded in Ronchi gratings (Vallmitjana, 1995).

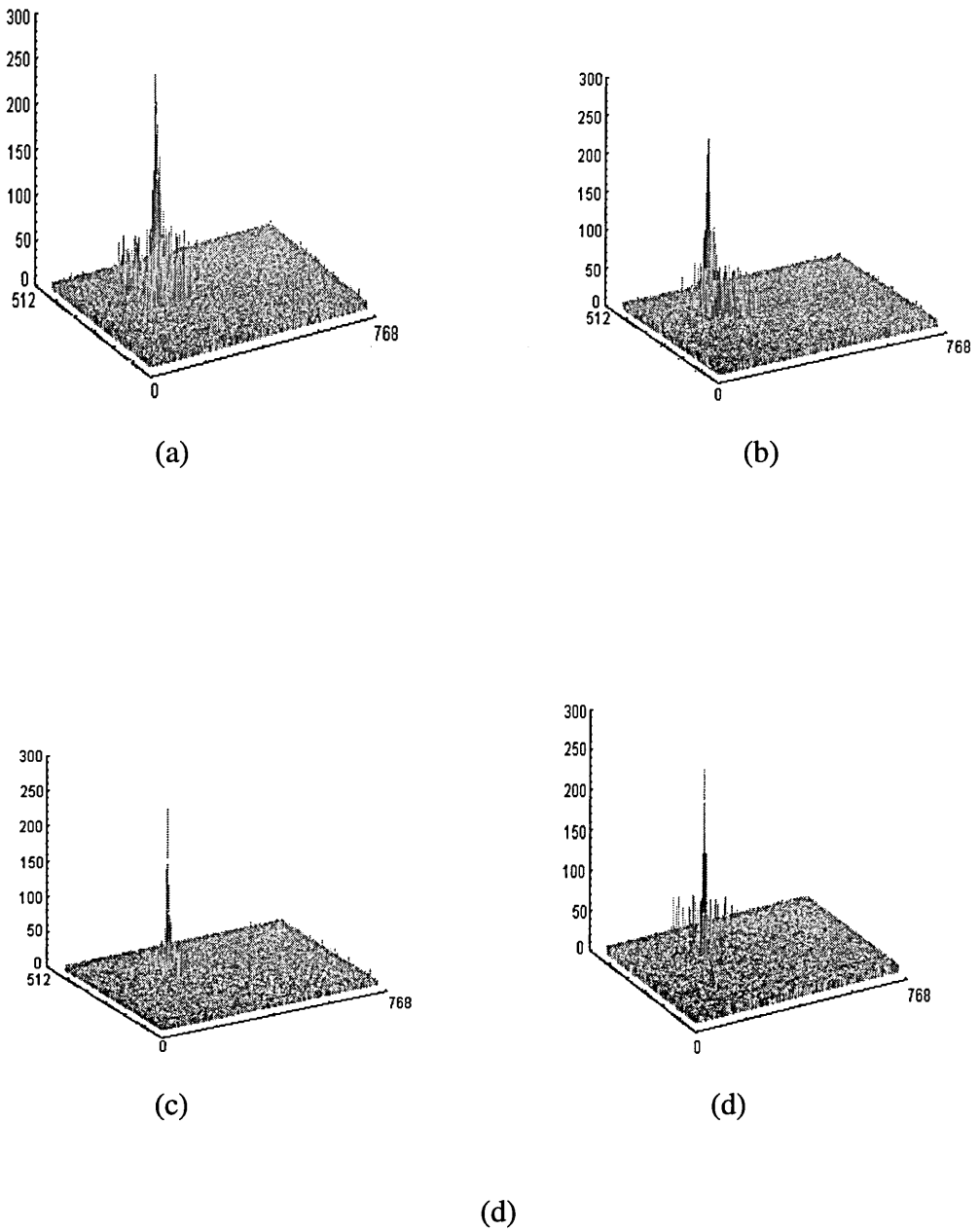

Fig. 8.1 The experimental results of the zero-order CHF, three dimensional plots of the correlation obtained with, (a) a circular harmonic match filter and 0 degree rotation of the target, (b) with circular harmonic matched filter and a target rotation of 180 degree, (c) circular harmonic phase-only filter and 0 degree rotation of the target, (d) with a circular harmonic phase-only filter and 180 degree rotation of the target.

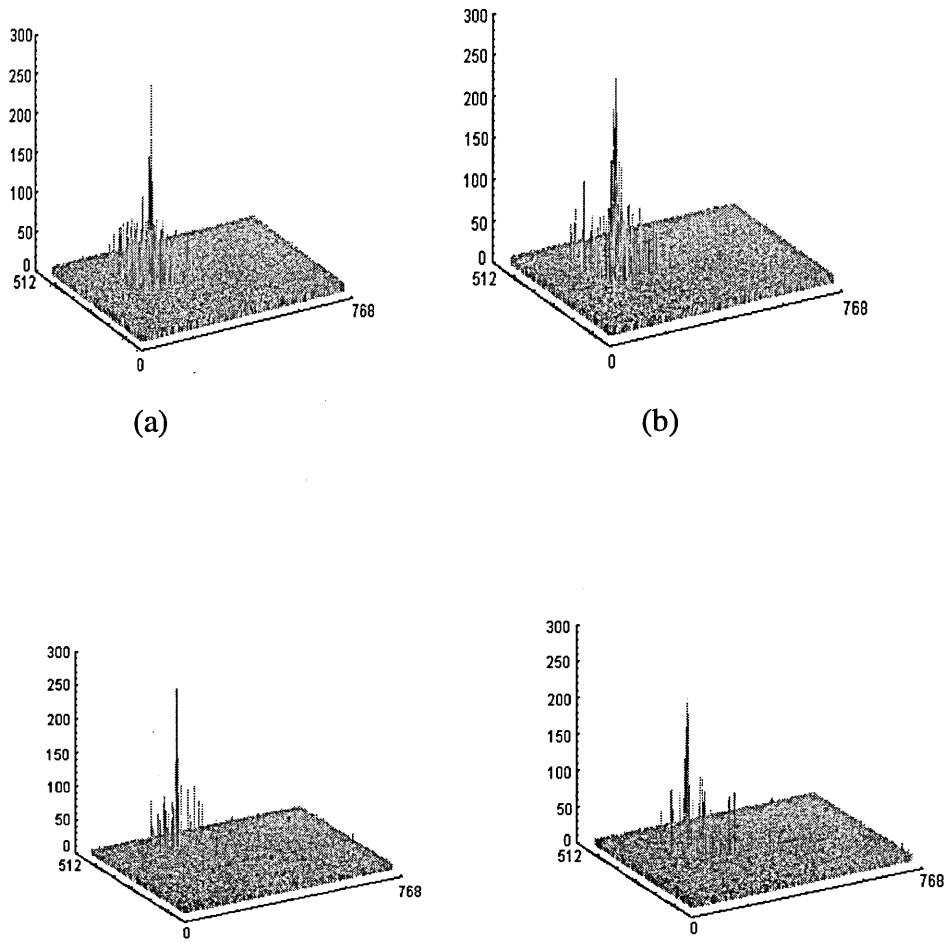

Fig. 8.2 The experimental results of the second-order CHF, three dimensional plots of the correlation obtained with, (a) a circular harmonic match filter and 0 degree rotation of the target, (b) with circular harmonic matched filter and a target rotation of 180 degree, (c) circular harmonic phase-only filter and 0 degree rotation of the target, (d) with a circular harmonic phase-only filter and 180 degree rotation of the target.

Filter	Zero-order CHF		Zero-order CHPOF		Second-order CHF		Second-order CHPOF	
Angle	0	180	0	180	0	180	0	180
PCI	255	225	240	218	195	195	165	180
SNR	32	30	45	41	28	27	42	39
$\overline{PCI}$	240		229		195		173	
$\overline{SNR}$	31		43		28		41	

Table 8.1 The correlation results with various CHFs, PCI: Peak Correlation Intensity; SNR: Signal-to-noise ratio.

The experimental results are shown in Fig. 8.1 and Fig. 8.2, for the zero-order and the second-order respectively; for each one, (a) is a three dimensional plot of the correlation obtained with the circular harmonic matched filter with 0 degree rotation of the target, (b) is as (a) but with a target rotation of 180 degree, (c) is a three dimensional plot of the correlation obtained with a circular harmonic phase-only filter and 0 degree rotation of the target and (d) is as (c) but with a 180 degree rotation of the target. For comparison, table 8.1 summarises the numerical results. From this experiment, we observe the following:

- Compared with a joint transform correlator with original images, no matter which circular harmonic component has been used to form a filter, the correlation peak is reduced significantly and the reduction worsens as the order of the circular harmonic increases.
- With phase-only circular harmonic filters, the anticipated higher correlation peaks have not been obtained, only signal-to-noise ratios show some improvement. For the zero order and the second order, the SNR has been improved by 41% and 46% respectively.

8.3 Tacking a Rotating Object with the Photorefractive JTC

In this experiment we followed the path of an aircraft with different rotational angles. Fig. 8.3 (a) shows the target aircraft. In order to improve light intensity transmission of the filter as well as its discrimination ability, instead of using a single circular harmonic component, a multiple circular harmonic filter composed of the 0 and $\pm$ 1 orders was used. As a result of this, full rotational invariance was not expected, however in practice, the loss of rotational invariance was not as serious as anticipated. Fig. 8.4 Shows the variation in correlation intensity with the rotation angles of the target. It is obvious that the intensity variation has a period of π instead of 2π and that there are also two peaks corresponding to rotations around 90 degree and 270 degree, presumably because the target aircraft has some element of symmetry. The ratio of minimum and maximum correlation intensity within one period is 0.75.

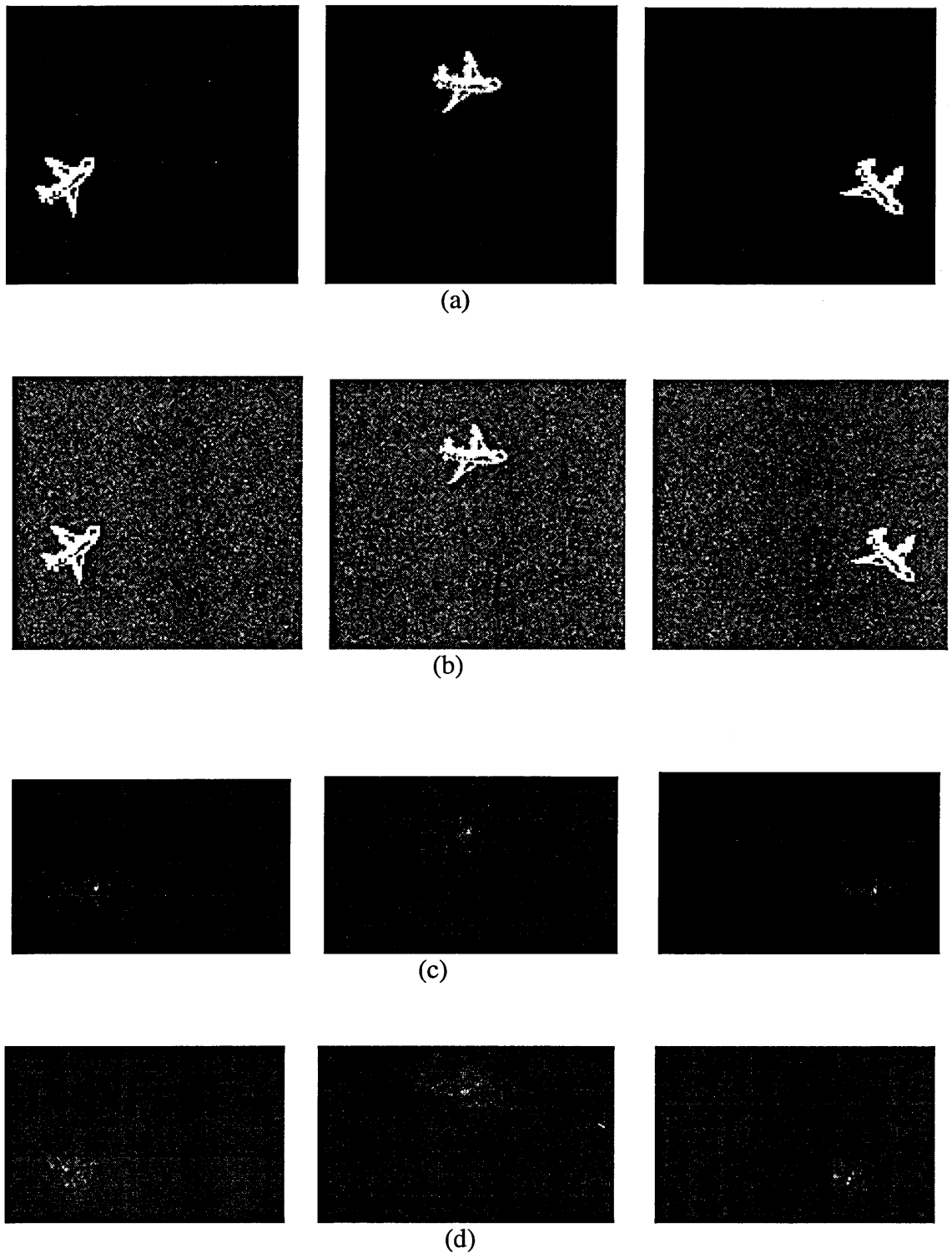

Fig. 8.3. (a) The target aircraft with different orientations, (b) The target aircraft against a non-overlapped noise background ($\sigma = 40$), (c) Correlation output plane of (a), (d) Correlation output plane of (b).

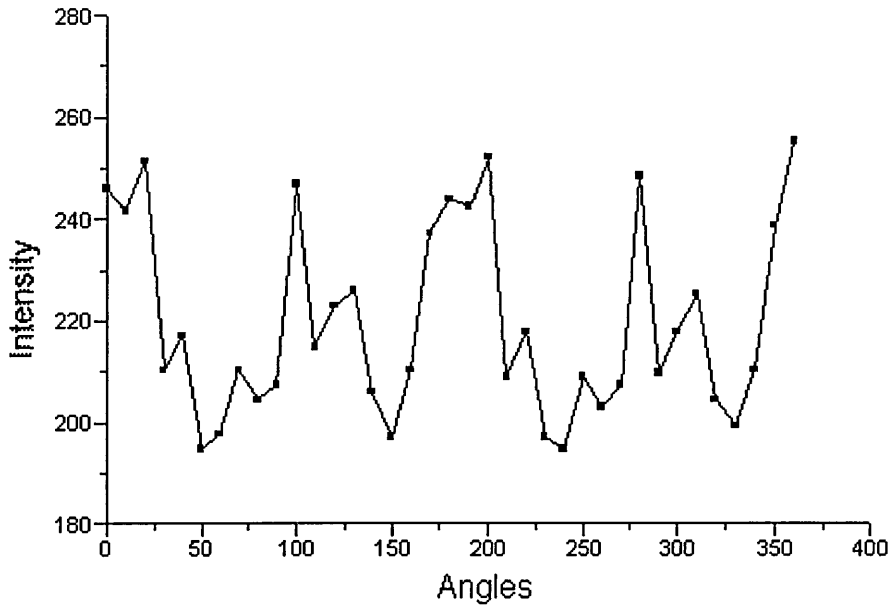

Fig. 8.4. The correlation intensity dependence on the rotational angles of the target.

To investigate the noise tolerance of the circular harmonic matched filter, noise with normal distribution and varying standard deviations, which does not overlap to the target, have been added to experimental scenes. Fig. 8.5 shows the signal-noise-ratio varies with the standard deviation (σ) of the background noise; with σ = 30 the SNR decreases by about 50%, thus the filter is quite sensitive to noise. In our experiment, by the time that the standard deviation of background noise had increased to 80, the correlation signal was difficult to distinguish from the background.

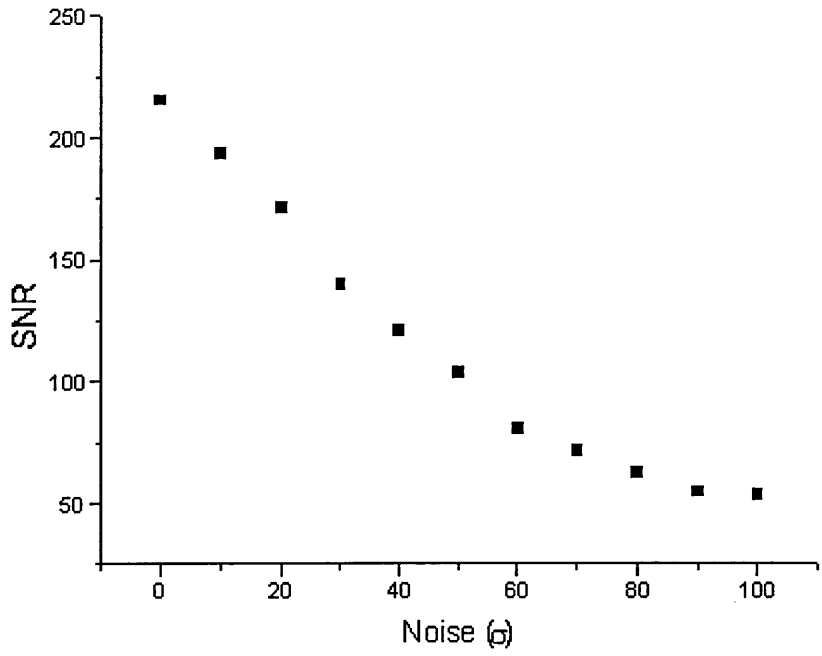

Fig. 8.5. The signal-to-noise ratio dependence on deviation of the background noise

Therefore, in our experiment, rotational invariance has been achieved by employing circular harmonic filters into a real-time photorefractive joint transform correlator. However, compared with the original joint transform correlator, it suffers from lower peak correlation intensity and lower signal-to-noise ratio. With a phase-only filtering technique, the correlation peaks become sharper while peak intensity shows no obvious enhancement. It is possible to use a multiple circular harmonic filter to follow an object with different orientations, even under slightly noisy conditions. When more than one circular harmonic components are used to form a filter, only partial rotational invariance can be obtained, however in practice this may not be particularly worrying especially if the target displays some degree of symmetry.

8.4 Wavelet Transforms in a Photorefractive JTC with CHFs

8.4.1 The experimental setup

In our experiment, a couple of 2-D Mexican-hat wavelets with different dilation factors have been used as spatial filters. It is a function with revolution symmetry. The mother Mexican-hat wavelet is the second derivative of the Gaussian function (Alam, 1999).

$$h(x,y)=\left[1-(x^2+y^2)\right]\exp\left(-\frac{x^2+y^2}{2}\right) \tag{8.1}$$

It is even and real, and the wavelet admissible condition is satisfied. The Fourier transform of the Mexican-hat wavelet is

$$H(p,q)=4\pi^2(p^2+q^2)\exp\left[-2\pi(p^2+q^2)\right] \tag{8.2}$$

with the dilation factor a, the Fourier spectrum is

$$H_a(p,q)=aH(au,av) \tag{8.3}$$

$\left|H_a(p,q)\right|^2$ is the filter inserted in the Fourier domain. By varying the factor a, different band-pass operations can be obtained.

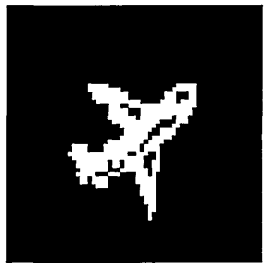

Fig. 8.6. The target aircraft.

The reference object selected is an aircraft shown in Fig. 8.6. The zero order and the second order circular harmonic components were used in turn to form the matched filters. Fig. 5.3 shows the experimental set-up. The target aircraft and the circular harmonic filters are displayed side by side in the input plane, which is an image of 768 x 512 pixels generated by a frame grabber and scaled to ensure the correct registration of the pixels on the LCTV. The Fourier transform is formed at the BSO crystal which is positioned at the back focal plane of the lens L1. For the read-out part, He-Ne laser light is expanded and collimated so that the joint power spectrum grating can be addressed. The wavelet functions are displayed at IP1 to filter the JPS. The correlation output is formed by lens L2, and an interference filter IF and a polaroid P1 are used to suppress the background noise.

8.4.2. Experimental results and analysis

The experimental results are showed in Fig. 8.7, Fig. 8.8, Fig. 8.9 and Fig. 8.10 for the zero-order and the second-order, with or without rotation, respectively. All images are 128 x 128 pixels cut from the correlation output plane (768 x 512). Fig.8.7 and 8.8 shows the results with the zero-order, the former deals with target aircraft without rotation and the later refers the correlation output with the target with 180 degrees rotation. In both of them, (a) is the correlation output with conventional circular harmonic filter, (b), (c) and (d) are results with different Mexican-hat wavelets. Fig. 8.9 and 8.10 shows the results of the second-order with the same sequences as Fig. 8.7 and 8.8, respectively. It is evident from these images that by employing Mexican-hat wavelet, the

correlation output have been modified, the change of the correlation profile depends on the scaling factor chosen to form the wavelet filter. The larger the scaling factor, the less the noise at the output plane, and there is no evident loss of peak correlation intensity. Compared with the results we obtained from the former experiments of using a Mexican-hat wavelet in a conventional joint transform correlator (not with circular harmonic components), the modification is more evident, probably because the output plane of a JTC with circular harmonic filter is poorer than the conventional ones. Employing wavelets a more obvious improvement to the JTC with circular harmonic filters.

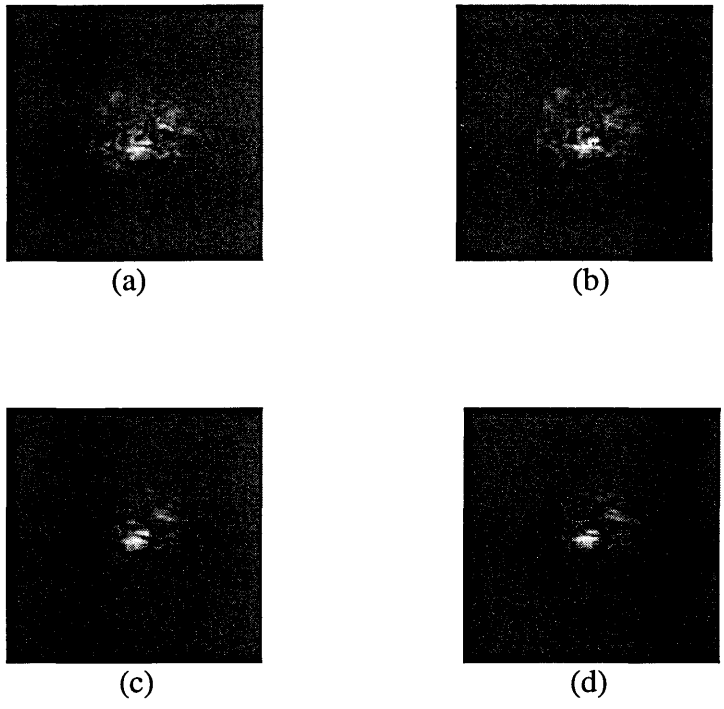

Fig. 8.7 The experimental results with zero-order circular harmonic filter and target 0 degree rotation.

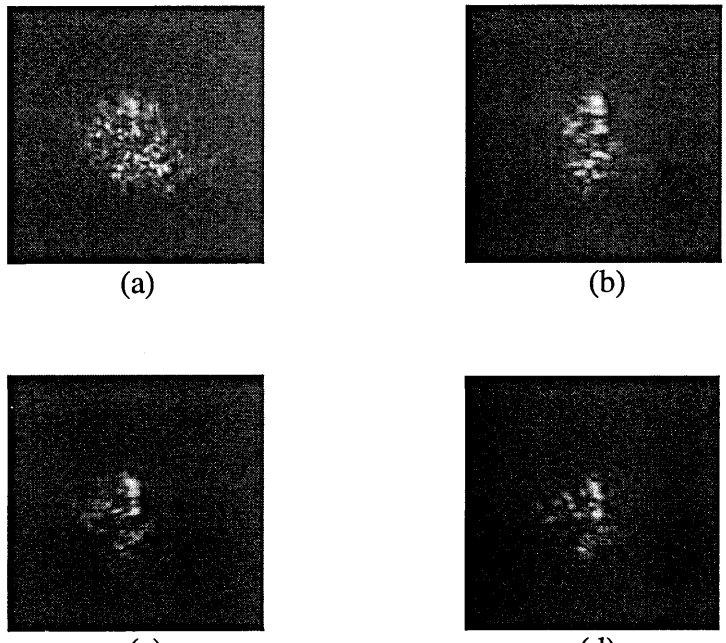

Fig. 8.8 The experimental results with zero-order circular harmonic filter and target 180 degree rotation.

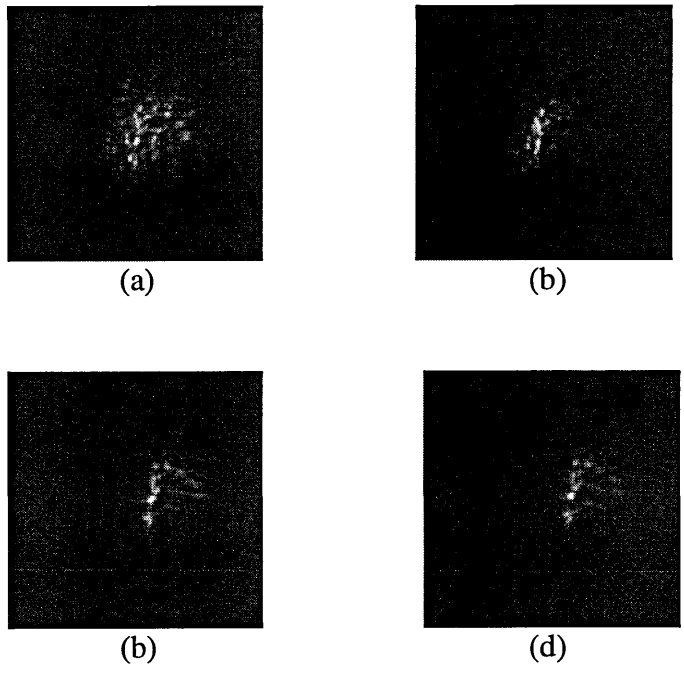

Fig. 8.9 The experimental results with the second-order circular harmonic filter and target 0 degree rotation.

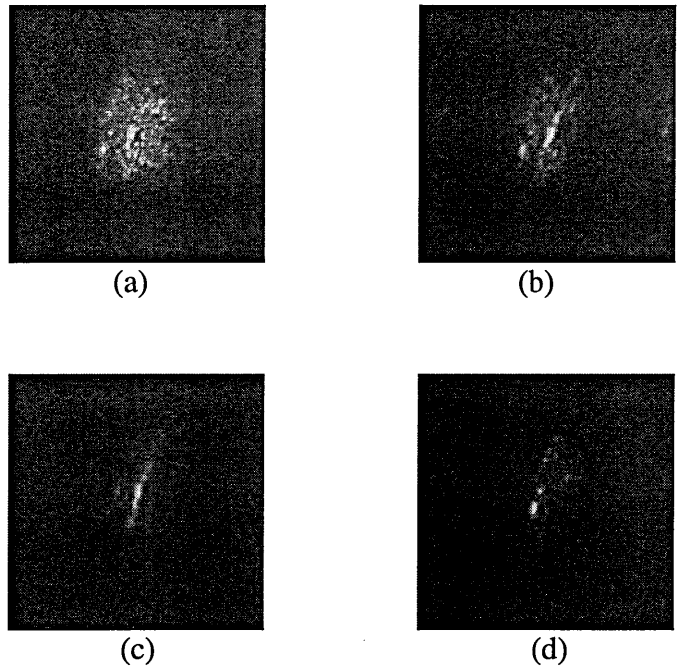

Fig. 8.10. The experimental results with the second-order circular harmonic filter and target 180 degree rotation.

For a clear comparison, table 8.1 summarizes the numerical results. The performance criteria used are the correlation peak intensity (CPI) with a quantization of 0-255, the signal-to noise ratio (SNR) and the half-correlation-peak-width (HCPW). The SNR is defined as the ratio of the peak correlation intensity to the mean intensity outside a 50% peak value in the correlation which represents the sharpness of the correlation peak and determines the chance of an error in pattern recognition. HCPW is the width of the correlation term at half its peak value (measured as pixel numbers). AVEs are their average values. From these data, we have obtained, in our experiment

- The rotational invariance exists for 0 and π degrees after employing wavelet transforms into the joint transform correlator,
- With the wavelet function in the JTC, the peak correlation intensity shows some reduction, but not seriously so.

- The signal-to-noise ratios have been improved by using wavelet functions, the increase depends on the scaling factor chosen. This means the wavelet filter has reduced the noise level of the output plane.
- The peak correlation intensity of the second-order circular harmonic is almost the same as with the zero-order.

Filters	Wavelets	PCI			SNR			HCPW		
		Rotation		AVE	Rotation		AVE	Rotation		AVE
		0	π		0	π		0	π	
Zero-order	No-wavelet	242	238	240	14.6	10.5	12.6	39	89	64
	Wavelet1	224	220	222	16.3	16.0	16.2	37	68	52
	Wavelet2	204	222	213	16.8	15.4	16.1	37	54	46
	Wavelet3	178	191	185	15.7	14.6	15.2	57	71	64
2nd-order	No-wavelet	224	228	226	12.7	11.1	11.9	30	53	42
	Wavelet1	224	208	216	18.1	18.1	18.1	18	17	18
	Wavelet2	222	206	214	19.0	17.8	18.4	9	21	20
	Wavelet3	174	168	171	12.4	14.3	13.4	23	22	22

Table 8.2. The experimental results with various circular harmonic expansion filters with or without wavelet transform functions.

In this way, we have investigated the behavior of wavelet transforms in a photorefractive joint transform correlator with circular harmonic filters. A bank of wavelet filters derived from a mother Mexican-hat wavelet have been selected to accomplish band-pass operations in the JTC Fourier domain. The zero-order and second-order circular harmonic components have been used in the experiment. The experimental results show that rotational invariance exists after incorporating the Mexican-hat wavelet into this setup. These wavelet functions modified the correlation contours and made them sharper, hence improving the discrimination for orientation invariant pattern recognition.

The improvement depends partly on the circular harmonic orders used to form the filter. In our experiment, the second order performs better than the zero-order. Compared with the experiment discribed before (with wavelet filters in a conventional joint transform correlator), the improvement is more evident by employing wavelet filters in a circular harmonic joint transform correlator.

Chapter 8: References

M.S. Alam, "Wavelet based joint transform correlation", Proceedings of the SPIE, 3715, 236-247, Orlando, 1999.

H.H. Arsenault, and Y. Sheng, "Properties of the circular harmonic expension for rotation-invariant recognition", Appl. Opt. **25**(18), 3225-3229 (1986).

A.S. Awwal, M.A. Karim and S.R. Jahan, "Improved correlation discrimination using an amplitude-modulated phase-only filter", Appl. Opt. **29**, 233-236 (1990).

S. Chang, S.A. Boothroyd, and J. Chrostowski, "Partial rotation-invariant pattern matching and face recognition with a joint transform correlator", Appl. Opt. **36**(11), 2380-2387 (1997).

N.J. Cook, A. Carnicer, S. Vallmitjana, I. Juvells, C.M. Cartwright, and W.A. Gillespie, "Implementation of a photorefractive binary joint transform correlator" J. Opt. Soc. Am. B. **15**(7), 1977-1984 (1998). J.L. Horner and P.D. Gianino, "Phase-only matched filtering", Appl. Opt. **23**, 812-816 (1984).

Y.N. Hsu, H.H. Arsenault, and G, April, "Rotational-invariant digital pattern recognition using circular harmonic expansion", Appl. Opt. **21**, 4012-4015 (1982).

Y.N. Hsu, and H.H. Arsenault, "Pattern discrimination by multiple circular harmonic component," Appl. Opt. **23**(6), 841-844 (1984).

B. Javidi, "Nonline joint power spectrum based optical correlation", Appl. Opt. **28**, 2358-2367 (1989).

B. Javidi and J.L. Horner, "Real-time optical information processing", Academic Press, INC., California 1994. Chapter I.

B.V.K.V. Kumar and T.K. Khim Ng, "Multiple circular-harmonic-function correlation filter providing specified response to in-plane rotation", Appl. Opt. **35** (11), 1871-1878 (1996).

Leclerc, Y. Sheng, H.H Arsenault, "Optical binary phase-only filters for circular harmonic correlation", Appl. Opt. **30**(32), 4643-4649 (1991).

S. Vallmitjana, A. carnicer, E. Martin-Badosa, and I. Juvells, "Nonlinear filtering in object and Fourier space in a joint transform optical correlator: comparison and experimental realization," Appl. Opt. **34**(20), 3942-3949 (1995).

J. Wang, and B. Javidi, "Multiobject detection using the binary joint transform correlator with different types of thresholding methods", Opt. Eng. **33**(6), 1793-1805 (1994).

P. Willett, B. Javidi, and M. Lops, "Analysis of image detection based on Fourier plane nonlinear filtering in a joint transform correlator," Appl. Opt. **37**(8), 1392-1341 (1998).

H. Zhang, Z.Q. Wang, C.M. Cartwright, M.S. Ding, N.J. Cook, and W.A. Gillespie, "A circular harmonic quantized amplitude compensated matched filter", Optik **109** (3), 119-123 (1998).

H. Zhang, C.M. Cartwright, M.S. Ding, Z.Q. Wang, N.J. Cook, and W.A. Gillespie, "Experimental implementation of a photorefractive joint transform correlator with circular harmonic filters", Opt. Comm. **173**, 129-136 (2000).

H. Zhang, C.M. Cartwright, M.S. Ding, and W.A. Gillespie, "Optical implementation of a photorefractive joint transform correlator with wavelet filters", Opt. Comm. **181**, 223-230 (2000).

Summary and Conclusions

This thesis has presented a discussion of optical pattern recognition with the photorefractive joint transform correlator and object and frequency space filtering techniques.

The work started with the investigation of the properties of the BSO crystal and utilizing these properties to realize an edge enhancement operation. After that, there were two main aspects to this research work: real-time photorefractive joint transform correlation and highly discriminant and rotationally invariant filter design. Then the two aspects were combined together, that is, the implementation of photorefractive joint transform correlator with wavelet filters for high-speed discriminant pattern recognition and feature extraction, and circular harmonic filters for rotationally invariant pattern recognition.

The moving grating technique has been applied to the real-time optical correlation systems to realize image edge enhancement. It has discribed the nonlinear dependence of the optimum fringe velocity on the fringe modulation and the variation of the enhancement of the diffraction efficiency with fringe modulation by moving gratings with a fixed fringe velocity suitable to high fringe modulations. The most interesting result is that there are two groups of data in the variation of the optimum fringe velocity with fringe modulation over a range of fringe modulations, and the velocity difference between these two groups is very large. Edge enhancement of objects and edge enhanced correlation have been achieved by moving gratings. The sharpness of the auto-correlation peak has been improved using the moving gratings. This is a significant improvement of the discrimination for optical pattern recognition. The proposed edge enhancement technique has the unique advantages of being able to arbitrarily select spatial frequencies to be enhanced, improved signal-to-noise ratio and the elimination of fluctuations of the output due to the resonant effects of moving gratings. Therefore the proposed technique is attractive in respect to the applications of photorefractive crystals.

It has been shown that the performance of optical pattern recognition can be improved with proper filtering techniques. The quantized amplitude-compensated matched filter is characterized by its simple structure, with only a few discrete grey levels, and excellent signal-to-noise ratio performance which determines the probability of an error in recognition and can be regarded as one of the most important performance criterion. This work has been extended to circular harmonic expansion filters for rotation-invariant recognition. It is shown that there is a trade-off between the signal-to-noise ratio and the Horner efficiency with the amplitude compensation technique. The trade-off is dependent on the circular harmonic order used. We have also applied the quantized amplitude technique to the Fresnel lens-encoded binary filter and created the Fresnel lens-encoded quantized amplitude-compensated matched filter to improve filter performance. In a comparison with the Fresnel lens-encoded binary filter, the proposed spatial filter possesses an excellent signal-to-noise ratio which is a significant improvement because the signal-to-noise ratio determines the probability of a false detection. Therefore it is considered to be a strong candidate particularly in real-time applications. The quantized amplitude compensation technique has also been applied to the Fresnel lens-encoded circular harmonic binary filter for rotationally invariant recognition. The zero-order and the first-order of the circular harmonic terms were selected to form the filters in the simulations.

Photorefractive materials can be used as a dynamic holographic medium in a joint transform correlator for real time recording and reading. We have investigated the performance of the photorefractive crystals BSO and KNSBN in a joint transform correlator. The correlation output patterns from the JTC with both crystals, the dependence on applied field, the variation of the signal-to-noise ratio, and the time for the erasure of gratings inside the crystals are compared. BSO can only work effectively under the condition that it is used with an appropriate applied field, and the short grating erasure time makes it suitable for real time processing. On the other hand, SBN can work as a recording material with or without an applied field. The period needed for erasing the grating inside the SBN crystal is much longer than BSO. Generally speaking, the JTC

with the crystal KNSBN performs not as well as the one with BSO, the correlation peak is broader and the signal-to-noise is lower.

Nevertheless, the photorefractive JTC for pattern recognition has its problems, such as low discrimination, and broad correlation peaks. The performance of a photorefractive JTC can be improved by additional processing of the reference and scene functions. In order to improve the discrimination ability as well as the signal-to-noise ratio of the photorefractive JTC, a coherent erasure method has been presented to modify the matched-filter-based joint transform correlator. In this implementation, in addition to the two beams forming the conventional joint power spectrum in the Fourier plane, a third coherent beam is used to generate filters or non-linearity in order to increase the discrimination capability of the joint transform correlator. The three beams form a so-called triple correlator. Therefore, the frequency spectrum in the Fourier plane of a conventional joint transform correlator can be modified with a third coherent beam and an encoded image in its object plane as the third input. The image can be chosen to implement a special filter or as a non-linearity. Both computer simulations and experimental results show that correlation performance has been improved with this method. The third beam gives the joint transform correlator another degree of freedom, which may have other uses in the future.

For the incoherent triple JTC, wavelet transforms are used in the experiments. We have demonstrated a photorefractive joint transform correlator with various wavelet filters to extract different kinds of feature. Both computer simulation and experimental results have shown that these encoded wavelet filters work effectively in the photorefractive JTC with the purpose of extracting different local features of images, such as corners and edges. The wavelet transform filters also have been used to modify the correlation profiles of optical correlators. A real-time photorefractive joint transform correlator with wavelet transform filters is presented to improve the correlation performance. The Mexican-hat wavelets are used in the correlator in the frequency domain, instead of in the space domain as the Mexican-hat wavelet functions have negative values in the space domain but have positive Fourier spectra. The signal-to-

noise ratio, discrimination ability and noise robustness of the wavelet transform JTC have been improved with appropriate wavelet functions.

Rotational invariance can be achieved by employing circular harmonic filters into a real-time photorefractive joint transform correlator. However, compared with the original joint transform correlator, it suffers from lower peak correlation intensity and lower signal-to-noise ratio. In order to improve the light transmission of the references, we used the 'IDL' software to scale both the matched filter and phase only filter before display at the joint input plane. With a phase-only filtering technique, the correlation peaks become shaper while the peak intensity shows no obvious enhancement. The experimental results from the circular harmonic JTC and circular harmonic phase only JTC have been compared for several single circular harmonic components. After that we used a multiple CHF in a JTC to follow the track of an aircraft with rotations within ±90. It is possible to use a multiple circular harmonic filter to follow an object with different orientations, even under slightly noisy conditions. When more than one circular harmonic components are used to form a filter, only partial rotational invariance can be obtained, however in practice this may not be particularly worrying especially if the target displays some degree of symmetry.

We have also investigated the behavior of the wavelet transforms in a photorefractive joint transform correlator with circular harmonic filters. A bank of wavelet filters derived from a mother Mexican-hat wavelet have been selected to accomplish band-pass operations in the JTC Fourier domain. The zero-order and second-order circular harmonic components have been used in the experiment. The experimental results proved that the rotational invariance exists after employing the Mexican-hat wavelet into this setup. These wavelet functions modified the correlation contours and made them sharper, hence improve the discrimination for the orientation invariant pattern recognition. The improvement depends partly on the circular harmonic orders used to form the filter.

For the future work, other wavelet filters could be used for different purposes such as feature extraction and to improve performance. We have shown that it is possible to

achieve high performance with wavelet filters with proper dilations in a photorefractive JTC. However, the discrete wavelet scaling factors have been selected without accurate calculation, therefore the problem remains of how to choose a proper dilation automatically to achieve a good correlation output. For this purpose, in the next stage, an optimizing search could be involved in the filter calculation. In the triple joint transform correlation, we have used four beams to implement a triple correlator, in which a He-Ne beam is used as read-out beam. In the future, there may be the possibility of using the third coherent beam to write the image and also read out the fringes inside the crystal simultaneously, this would be helpful to simplify the experimental implementation and reduce the background noise at the output plane. For circular harmonic filters, faster and more accurate algorithms are required to calculate the proper expansion centers for the filters, and also effective methods are needed to optimize a single filter's performance and to construct multiple CHFs with both good performance and simple structure.

Appendix List of Publications

The following publications and conference presentations were based on the work presented in this thesis.

Publications:

H. Zhang, Z.Q. Wang, C. Cartwight, M. Ding, N. Cook, and W. Gillespie, A circular harmonic quantized amplitude compensated matched filter, *Optik* **109** (3), 119-123 (1998).

Z.Q. Wang, H. Zhang, C. Cartwright, M. Ding, N. Cook, and W. Gillespie, Edge enhancement by use of moving gratings in a bismuth silicon oxide crystal and its application to optical correlation, *Applied Optics*. **37** (20), 4449-4456 (1998).

Z. Q. Wang, H. Zhang, C. Cartwright, M. Ding, N. Cook, W. Gillespie, " A Fresnnel lens-encoded quantized amplitude-compensated matched filter with circular harmonic expansions", *Journal of Optoelectronics Laser*, 9 179-185 (1998).

H. Zhang, C. Cartwright, M. Ding, and A. Gillespie, A triple joint transform correlator, SPIE **3715**, 185-196 (1999).

H. Zhang, C. Cartwright, M. Ding, Z.Q. Wang, N. Cook, and A. Gillespie, Experimental implementation of a photorefractive joint transform correlator with circular harmonic filters, *Optics Communications* **173**, 129-136 (2000).

H. Zhang, C. Cartwright, M. Ding, and A. Gillespie, Optical implementation of a photorefractive joint transform correlator with wavelet filters, *Optics Communications*, **181** (4-6), 223-230 (2000).

H. Zhang, C. Cartwright, M. Ding, and A. Gillespie, "Image feature extraction with wavelet transforms in a photorefractive joint transform correlator", accepted by *Optics Communications.*

H. Zhang, C.M. Cartwright, M. Ding, Z.Q. Wang, B.L. Liang, and A. Gillespie, "Rotationally invariant pattern recognition in a photorefractive joint transform correlator using circular harmonic filters and the wavelet transform", submitted to *Optics Communications.*

Conference Presentation:

H. Zhang, C.M. Cartwright, M.S. Ding and W.A. Gillespie, "Triple joint transform correlator", Aerosense'99, Orlando, USA, April 1999.